Back-propagation beamformer design with transverse oscillations for motion estimation in echocardiography

Xinxin Guo

N° d'ordre: 2014ISAL0085 Année 2014

THÈSE

Back-propagation beamformer design with Transverse Oscillations for motion estimation in echocardiography

Délivrée par
L'INSTITUT NATIONAL DES SCIENCES APPLIQUÉES DE LYON

Pour obtenir
DIPLÔME DE DOCTORAT

Ecole doctorale :
ELECTRONIQUE, ELECTROTECHNIQUE, AUTOMATIQUE

Soutenue publiquement le 12/09/2014 par
Xinxin GUO

Jury

Directeurs de thèse:	
Denis FRIBOULET	Professeur d'Universités, INSA de Lyon
Hervé LIEBGOTT	Maître de Conférences, HDR, Université Claude Bernard, Lyon I
Rapporteurs:	
Jean-Marc GIRAULT	Maître de Conférences HDR, Université François Rabelais, UMRS "Imagerie & Cerveau", Tours
Marc LETHIECQ	Professeur, Université François Rabelais, GREMAN, Tours
Examinateurs:	
Denis KOUAME	Professeur, Université Paul Sabatier, Toulouse III
Christian CACHARD	Professeur, Université Claude Bernard, Lyon I

INSA Direction de la Recherche

SIGLE	ECOLE DOCTORALE	NOM ET COORDONNEES DU RESPONSABLE
CHIMIE	**CHIMIE DE LYON** **http://www.edchimie-lyon.fr** Insa : R. GOURDON	M. Jean Marc LANCELIN Université de Lyon – Collège Doctoral Bât ESCPE 43 bd du 11 novembre 1918 69622 VILLEURBANNE Cedex Tél : 04.72.43 13 95 directeur@edchimie-lyon.fr
E.E.A.	**ELECTRONIQUE, ELECTROTECHNIQUE, AUTOMATIQUE** **http://edeea.ec-lyon.fr** Secrétariat : M.C. HAVGOUDOUKIAN eea@ec-lyon.fr	M. Gérard SCORLETTI Ecole Centrale de Lyon 36 avenue Guy de Collongue 69134 ECULLY Tél : 04.72.18 60 97 Fax : 04 78 43 37 17 Gerard.scorletti@ec-lyon.fr
E2M2	**EVOLUTION, ECOSYSTEME, MICROBIOLOGIE, MODELISATION** **http://e2m2.universite-lyon.fr** Insa : H. CHARLES	Mme Gudrun BORNETTE CNRS UMR 5023 LEHNA Université Claude Bernard Lyon 1 Bât Forel 43 bd du 11 novembre 1918 69622 VILLEURBANNE Cédex Tél : 04.72.43.12.94 e2m2@biomserv.univ-lyon1.fr
EDISS	**INTERDISCIPLINAIRE SCIENCES-SANTE** **http://ww2.ibcp.fr/ediss** Sec : Safia AIT CHALAL Insa : M. LAGARDE	M. Didier REVEL Hôpital Louis Pradel Bâtiment Central 28 Avenue Doyen Lépine 69677 BRON Tél : 04.72.68 49 09 Fax : 04 72 35 49 16 Didier.revel@creatis.uni-lyon1.fr
INFOMATHS	**INFORMATIQUE ET MATHEMATIQUES** **http://infomaths.univ-lyon1.fr**	M. Johannes KELLENDONK Université Claude Bernard Lyon 1 INFOMATHS Bâtiment Braconnier 43 bd du 11 novembre 1918 69622 VILLEURBANNE Cedex Tél : 04.72. 44.82.94 Fax 04 72 43 16 87 infomaths@univ-lyon1.fr
Matériaux	**MATERIAUX DE LYON** Secrétariat : M. LABOUNE PM : 71.70 –Fax : 87.12 Bat. Saint Exupéry **Ed.materiaux@insa-lyon.fr**	M. Jean-Yves BUFFIERE INSA de Lyon MATEIS Bâtiment Saint Exupéry 7 avenue Jean Capelle 69621 VILLEURBANNE Cédex Tél : 04.72.43 83 18 Fax 04 72 43 85 28 Jean-yves.buffiere@insa-lyon.fr
MEGA	**MECANIQUE, ENERGETIQUE, GENIE CIVIL, ACOUSTIQUE** Secrétariat : M. LABOUNE PM : 71.70 –Fax : 87.12 Bat. Saint Exupéry **mega@insa-lyon.fr**	M. Philippe BOISSE INSA de Lyon Laboratoire LAMCOS Bâtiment Jacquard 25 bis avenue Jean Capelle 69621 VILLEURBANNE Cedex Tél :04.72.43.71.70 Fax : 04 72 43 72 37 Philippe.boisse@insa-lyon.fr
ScSo	**ScSo*** M. OBADIA Lionel Sec : Viviane POLSINELLI Insa : J.Y. TOUSSAINT	M. OBADIA Lionel Université Lyon 2 86 rue Pasteur 69365 LYON Cedex 07 Tél : 04.78.69.72.76 Fax : 04.37.28.04.48 Lionel.Obadia@univ-lyon2.fr

- Écoles Doctorales – Quinquennal 2011-2015

Abstract

Echography is nowadays one of the most popular medical diagnosis modalities. It enables real-time observation the motion of moving organs which facilitates the diagnosis of pathologies for physician. Echocardiography [1, 2], blood flow imaging [3, 4] and elastography [5-7] are the favorite domains of motion estimation in using of echography (e.g., due to its high frame-rate capacity). Thus the requirements for imaging with high quality are on the primary place. In cardiac imaging, the conventional imaging system is somehow limited in the transverse direction (the direction perpendicular to the beam axis). Working on the image formation, this problem can be addressed by modifying the beamforming scheme in order to introduce transverse oscillations (TOs) in the system point spread function (PSF).

Transverse oscillation techniques have shown their potential for improving the accuracy of local motion estimation in the transverse direction (i.e., the direction perpendicular to the beam axis). The conventional design of TOs in linear geometry, which is based on the Fraunhofer approximation, relates PSF and apodization function through a Fourier transform. Motivated by the adaptation of TOs in echocardiography, we propose a specific beamforming approach based on back-propagation in order to build TOs in sectorial geometry.

The performance of the proposed back-propagation method has been studied gradually, in comparison with the Fourier transform, such as in evaluation of the quality of PSF, in estimation of simulated cardiac motion and in experiments study, etc. The quantified results demonstrate the proposed method leads to better controlled TOs images than the conventional beamforming.

Another method based on plane wave decomposition and a different back-propagation principle has been presented. This method is better taking into account the 2D property of PSF, by decomposing the PSF into a set of plane waves directionally, back-propagating them to the probe, by using the superposition results as excitations, a simulated PSF with high accordance to the theoretical one is acquired. By adapting this method to sectorial geometry, the quality of PSF obtained in front of probe is better using the plane wave decomposition method than that of Fourier relation, but it is limited for the scanning on the side of probe, so the further work will be addressed to adapting the plane wave decomposition method to the complete sectorial imaging.

Key words: echocardiography, motion estimation, back-propagation, transverse oscillation, beamforming, plane wave decomposition.

Résumé

L'échographie est aujourd'hui l'une des modalités les plus populaires de diagnostic médical. Il permet d'observer, en temps réel, le mouvement des organes qui facilite le diagnostic des pathologies pour des médecins. L'échocardiographie [1, 2], l'imagerie du flux sanguin [3, 4] et l'élastographie [5-7] sont les domaines préférés de l'estimation de mouvement en utilisant l'échographie (en raison de son haut frame-rate).En conséquence, les images avec meilleurs qualités sont nécessaires. . En imagerie cardiaque, le système classique d'imagerie est limité dans la direction transversale (la direction perpendiculaire à celle de propagation). Travaillant sur la formation des images, ce problème peut être résolu en modifiant la façon de formateur de voie afin d'introduire des oscillations transversales (OTs) dans la fonction d'étalement du point (PSF).

La technique d'oscillation transversale a montré son potentiel d'améliorer la précision de l'estimation de mouvement local dans la direction transversale (la direction perpendiculaire à celle de propagation). La classique OT en géométrie linéaire, basée sur l'approximation de Fraunhofer, relie la PSF et la fonction de pondération par la transformée de Fourier. Motivé par l'adaptation des OTs en échocardiographie, nous proposons une technique spécifique basée sur la rétro-propagation afin de construire des OTs en géométrie sectorielle.

La performance de la méthode de rétro-propagation proposée a été étudiée progressivement, comparée avec la méthode de la transformée de Fourier, par exemple, l'évaluation de la qualité de la PSF quantifié, dans l'estimation de mouvement cardiaque en simulation, et en étude la qualité des PSF visuellement expérimentale. Les résultats quantifiés montrent les OT-images sont mieux contrôlés par la méthode proposée que par le formateur de voie conventionnelle.

Une autre méthode, basée sur la décomposition d'onde plane et un principe différent de rétro-propagation, a été présentée. Cette méthode mieux prend en compte la propriété 2D de PSF, en décomposant la PSF dans un ensemble d'ondes planes directionnelle, les rétro-propage à la sonde, en utilisant les résultats de superposition comme excitations, un PSF simulée et conforme fortement au PSF théorique est acquis. En adaptant cette méthode à la géométrie sectorielle, la qualité de la PSF obtenue en face et sur la côté de la sonde est meilleure en utilisant la décomposition en ondes planes à celle de la transformée de Fourier, le travail supplémentaire sera adressé à adapter la décomposition en ondes planes à imagerie sectorielle et l'estimation du mouvement.

Mots-clés : échocardiographie, estimation de mouvement, rétro-propagation, oscillation transversale, formation de voie, décomposition en ondes planes

Remerciements

Tout d'abord, je tiens à adresser mes plus vifs remerciements à mon directeur de thèse, Denis Friboulet et Hervé Liebgott, pour m'avoir donné l'occasion de travailler et de m'avoir guidée, encouragée et conseillée pendant ma thèse. Cela a été un plaisir et un honneur de travailler avec eux, et il m'a fait progresser. Je le remercie beaucoup de m'avoir soutenue et motivée dans les moments difficiles.

Je tiens à remercier sincèrement Mme Isabelle E. Magnin, directrice de CREATIS, qui m'a permis de travailler dans un environnement scientifique de très haute qualité.

Je tiens également à remercier Martino Alessandrini qui m'a envoyé les données simulent le mouvement cardiaque, qui me permet d'avoir une recherche plus profonde de mon travail.

J'aimerais également dire un grand merci à Professeurs Jean-Marc Girault et Marc Lethiecq qui ont été rapporteurs de ma thèse. Leur expertise scientifique m'a aidé à améliorer le manuscrit et à préparer ma soutenance. Je remercie aussi le Professeur Denis Kouamé et Christian Cachard pour avoir accepté d'être membre de mon jury.

Je souhaite remercier Adeline Bernard et Sébastien Salles. Merci beaucoup pour leurs temps consacré à l'acquisition des données pour ce travail et pour les discussions valables. Un grand merci en outre à François Varry, je le remercie pour ses suggestions en amélioration de ma présentation de la soutenance.

Merci à mes collègues de laboratoire pour ces années vécues dans une ambiance studieuse mais toujours détendue. Ils étaient toujours gentils et patients. Je pense plus particulièrement à Philippe Delachartre, Olivier Bernard. Un grand merci à mes collègues de bureau : Fanglue Lin, Yue Zhao, Oana Lorintiu, Razvan Stoica et Hector.Jacinto. Merci à tous mes amis présents et passés au cours de ces quatre années, Yan Wang, Fangfang Duan, Yue Zhang, Hongying Li, Liang Wang, Pei Dong, Lin Wang et Miaomiao Zhang.

Table of notations

Variables

x, y, z	Spatial variables, lateral, axial and azimuthal respectively
$w(x)$,	Apodization function
λ , λ^{PSF} , λ_{θ}^{PSF}	Wavelength
σ^{PSF} , σ_{θ}^{PSF} , σ_{θ}^{Apo}	Standard deviation
$h(x,y,z)$	Impulse response
k , k_1 , k_2	Constant coefficient
r	Scanning radius
$e(\mathbf{s},t)$	Elementary signal
$p(x,y)$, $p(\theta,r)$	Pressure field
f_0	Center frequency of signal
i, j	indicator
θ	Angle
d	Distance
c	Sound velocity

Abbreviations

BP	Back-propagation
RMSE	Root mean square error
ROI	Region of interest
PWD	Plane wave decomposition
TO	Transverse oscillations
PSF	Point spread function
2D, 3D	Two-, three-dimensional

Contents

Contents of Figures

Chapter 1

Introduction

Contents

1.1 Ultrasound imaging and motion estimation

Ultrasound, known as an oscillating pressure wave with a frequency greater than 20 kHz, separates from audible sound, not because of differences in physical properties, but the fact that it is out of the upper limit of the human hearing range.

The use of ultrasound for medical applications began in the 1950s and had an extensive development and application in 1970s [8]. For more than forty years, it has become an important clinical diagnostic technology.

With the advantages of being noninvasive, inexpensive [9], non-ionizing and transportable when compared to X-ray, CT and MRI, ultrasound systems have been widely used in clinical diagnosis. Its characteristic of providing fast, real-time imaging makes it particularly fit to motion estimation as shown by 2 typical applications: measuring and visualizing blood flow using so called Doppler techniques; and estimating the movement of moving organs. As be described in [10] in the field of MRI, the coronary artery disease will induce important changes in regional myocardial deformation. In the framework of this thesis, we will focus on the application of ultrasound in cardiac imaging, i.e. on echocardiography. Why is echocardiography important? We all know that the heart is a moving organ whose motion can be affected by several pathologies [11], such as ischemia or infarct that can affect the cardiac motion. Meanwhile, cardiovascular pathologies are still one of the leading causes of mortality in western countries. As a consequence, it is of great importance to provide the doctors with an imaging modality that enables to image the motion of the heart during the cardiac cycle. In that case, ultrasound is an excellent candidate: as mentioned above, it provides indeed fast acquisition when compared to other imaging modalities.

In echocardiography, most often, only a projection of the 3D cardiac motion is shown up as 2D image sequences. A lot of researches have been dedicated to develop motion estimation techniques from echocardiographic image sequences, but it is not easy to estimate motion in the transverse direction with a high accuracy, hence a strong limitation of current motion estimation techniques. Fig. 1-1 defines the geometry: the beam propagates in the axial direction and the lateral direction or as called above the transverse direction is the direction perpendicular to the beam axis.

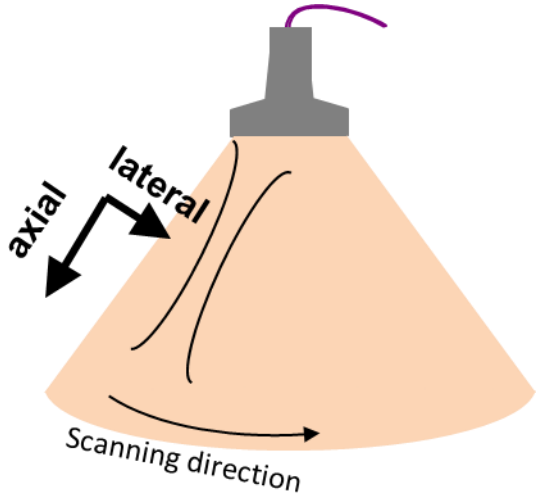

Fig. 1-1 : Definition of the imaging coordinate system: the ultrasound wave propagates in the axial direction and the in plane direction perpendicular to the beam axis is the lateral (or transverse) direction

1.2 Limitations of conventional acquisitions

The estimation of the displacement along the axial direction has been shown to be very accurate and this can be explained by the oscillations that are naturally present in the RF signals. Looking into the classical point spread function (PSF) in Fig. 1-2, the axial profile in Fig. 1-2 (b) is oscillating around the central frequency, while the profile in lateral direction is just a Gaussian-like envelop. As a result it is not easy to estimate motion in the transverse direction with a high accuracy, since a conventional acquisition cannot give the same oscillating characteristics in lateral direction as in the axial direction.

Even if several techniques have been described to estimate precisely multi-dimensional motion[12-15], as underlined by Lopata et al.[16] and confirmed in a more recent study [17]. Current motion estimation techniques can still not easily estimate motion in the transverse direction (direction perpendicular to the beam axis) with high accuracy. This problem can be addressed by modifying the image formation and using a beamforming scheme yielding a system point spread function (PSF) having in the lateral direction of the image the same oscillating characteristics as in the axial direction.

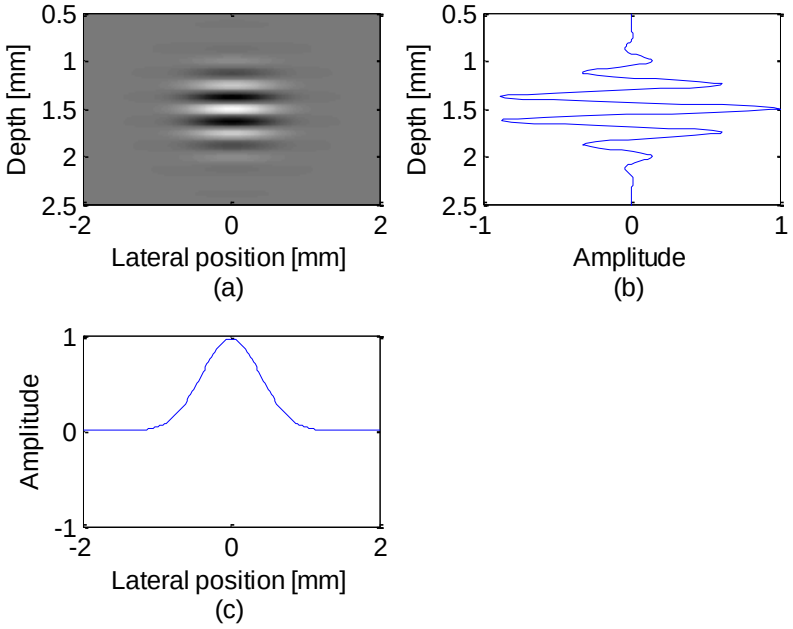

Fig. 1-2 : Classical PSF (a), with axial profile showing oscillations (b) and lateral profile having a smooth Gaussian like shape (c).

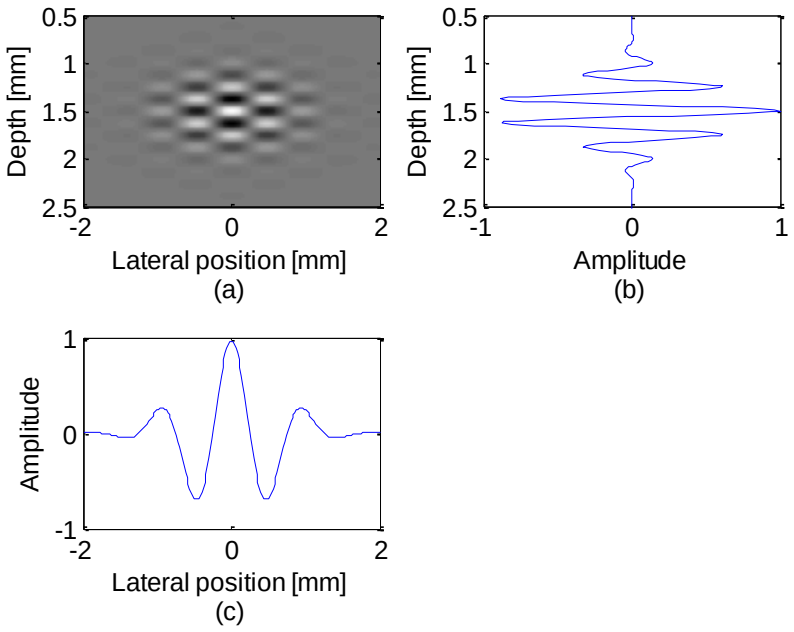

Fig. 1-3 : PSF with transvers oscillations (a), with its axial profile (b) and lateral profile (c) showing both axial and transverse oscillations.

1.3 Objective

In line with former section, a PSF with transverse oscillations (TOs) in Fig. 1-3 has been introduced in order to improve the motion estimation accuracy in lateral direction. The lateral profile in Fig. 1-3(c) presents the expected oscillating characteristics Fig. 1-2(c), and is thus called the transverse oscillations.

Transverse oscillations methods firstly arose in the late 1990s in the field of blood flow estimation [18, 19]. Several groups have been working on these methods. By now, TOs methods have been applied in blood flow estimation by Jensen et al. [19-21] and Anderson [18], in elastography by Sumi [22, 23] and our group [24, 25], and in echocardiography based on different beamforming strategies [26, 27] and estimators [28, 29].

These studies have shown that TOs images can lead to improved 2D motion estimation in linear geometry, i.e. when a linear probe is used. The formation of images featuring TOs in linear geometry uses conventional beamforming methods designed using the Fraunhofer approximation, which allows relating the apodization function and the system PSF through a simple Fourier transform. Application of TOs in echocardiography implies adapting this technique for sectorial scans. However, our preliminary investigations [30] have shown that conventional, Fraunhofer-based beamforming yields non-optimal TOs patterns. Therefore in this thesis we propose a new TOs beamformer design for sector scan. As will be described later on the document the proposed approach is based on the reciprocity theorem and uses back-propagation (BP).

So the objective of this thesis is to adapt the ultrasound images formation with TOs for 2D motion estimation in echocardiography, which implies in particular to work in a sectorial geometry.

1.4 Layout of this thesis

In this thesis, efforts are mainly taken into the beamformer design using back-propagation to adapt specific TOs images into sectorial geometry. The thesis is divided into the following four parts:

Background part:

This part includes chapter 2 and 3. Chapter 2 presents the background of ultrasound imaging. It describes in detail the principle of echography including the basic imaging by one transducer, the different imaging arrays used for different aims, the different

modes of echography; and then the formation of point spread function which is the basic model used throughout this thesis. Chapter 3 firstly gives a general introduction of beamforming techniques, after that it explains several methods for the specific transvers oscillations beamforming, including the Fraunhofer approximation, Sumi's method, the transvers oscillations design in linear geometry, and the transformation to sectorial geometry.

Contribution part:

This part presents all the contributions to this thesis which is the back-propagation method for transvers oscillations beamformer design adapted to sectorial geometry. Chapter 4 precises the principle of back-propagation method and introduces it to the transverse oscillations beamforming technique, and afterwards the conversion to sectorial geometry. Chapter 5 shows all the simulation and experiments results under comparison of the proposed back-propagation method with the conventional method. Simulations results on investigation of apodization function adaptation to variation of angles and on the evaluation of PSF qualities. Moreover, the influence of parameters to apodization functions is presented in the first place to study the performance of the proposed back-propagation versus the conventional method; chapter 6 is conducted to the plane wave decomposition, a different back-propagation method is described, then by superposition of all the back-propagated waves and using them as transmitting signals, the simulated PSF is with high agreement with the theoretical one in linear geometry, furthermore, the contribution to adapt this strategy to sectorial geometry is presented.

Conclusion and perspectives part:

Chapter 7 concludes the organization of this thesis and gives the perspectives of this work.

Chapter 2

Ultrasound Imaging

Contents

2.1 Introduction

In this chapter, we first introduce ultrasound imaging basic principles, i.e. the generation of excitation signals, the wave emission, propagation, diffraction and reception. We then describe different imaging arrays and different modes of echography that are commonly used. The notion of point spread function (PSF), which is central in this thesis is then presented in details.

2.2 Principle of echography

This section gives a description of basic ultrasound imaging. It is gradually explained by the image formation with one transducer, multi-transducer imaging arrays and the different imaging modes.

2.2.1 Transducer

The transducer is the basic and most important component of an ultrasound probe. It has two main functions, to transmit ultrasound signals, and to receive echoes. In transmission, an ultrasound signal is generated by exciting the piezoelectric transducer with an electric signal; strong, short electrical pulses from the ultrasound machine make the transducer ring at the desired frequency. On the surface of the probe, materials to enable impedance matching between transducer and skin, enable the sound to be transmitted efficiently into the body, undergoing diffraction, attenuation, diffusion and reflection. The return sound wave vibrates the transducer which turns the vibrations into electrical pulses that are then processed and transformed into a digital image by the scanner. The display in gray or color scale on the screen depends on the amplitudes of electrical signals.

The illustration in Fig. 2-2 shows a patient having echocardiography. The patient lies on his left side. A sonographer moves the transducer on the patient's chest, while viewing the echo pictures on a computer. In echocardiography, a square probe is used to emit and receive ultrasound in the range of 3.5 to 5 MHz. This probe is a small sized squared probe, allowing access the heart through the limited space between ribs. The Fig. 2-3 presents the cardiac image obtained.

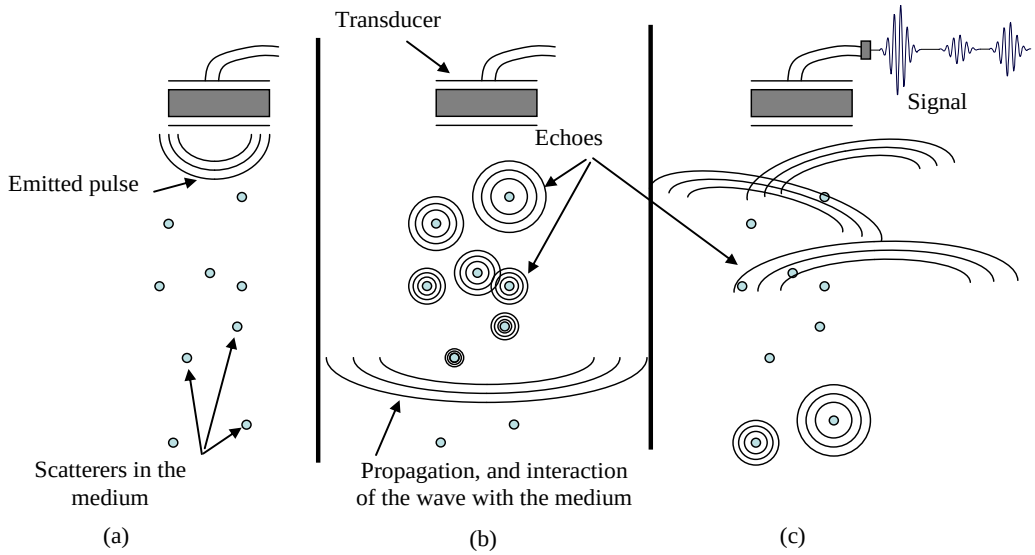

Fig. 2-1 : Basic principle of ultrasound imaging in using of one transducer [31]: (a) a pulse is emitted by the transducer, (b) shows the wave propagates through the medium, some echoes are backscattered from heterogeneities and (c) the echoes received at the transducer are traduced in an electrical signal.

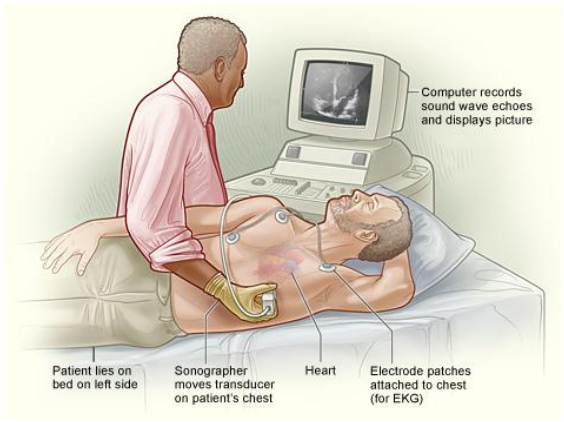

Fig. 2-2 : Illustration of a patient having echocardiography.

https://www.nhlbi.nih.gov/health/health-topics/topics/echo/during.html

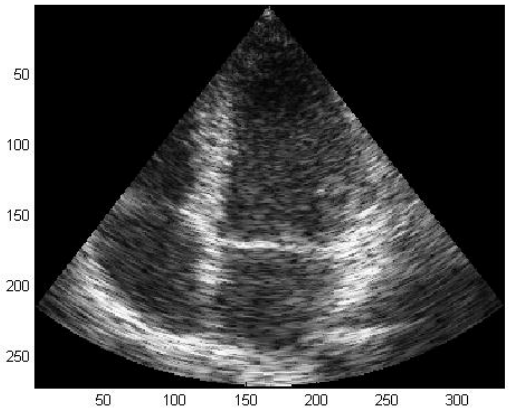

Fig. 2-3 : Echocardiography image in an apical four chamber view showing on top the two ventricle and on the bottom the two atria.

2.2.2 Imaging arrays

Only the principle of ultrasound imaging for one transducer and the probe used for echocardiography have been introduced, so in this section, three main kinds of ultrasound probe (linear arrays, convex arrays and phased arrays) which are composed by a series of elements will be explained in detail.

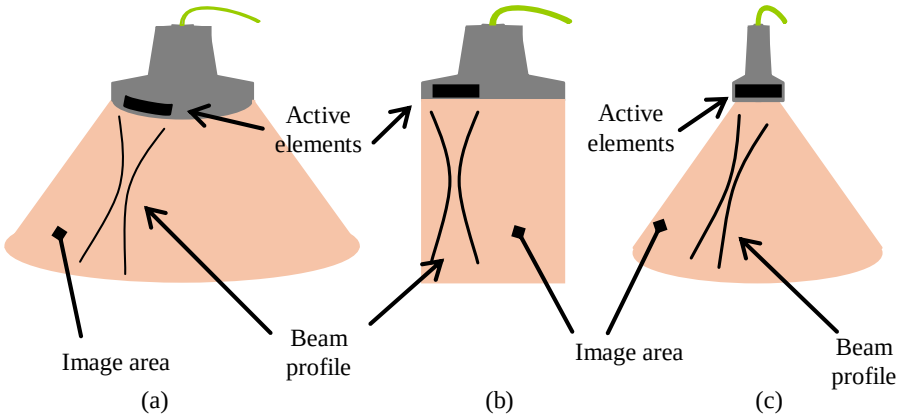

Fig. 2-4 : Principle of electronic sweeping with a convex array (a), a linear array (b), and a phased array [31]

Linear array

The linear array is used generally on vascular imaging, it is a rectangle composed by a number of A-lines (Amplitudes). Each line is acquired with a certain number of active elements which can be defined as sub-aperture. Taking a linear array with 192 elements as an example, using 128 active elements as sub-aperture to do scanning,

during the imaging process, the active elements translates in the linear array from one side to another, if they displace by one element, the size of the 64 elements leads to the width of image . Therefore a larger number of arrays are necessary to meet the need of larger region of imaging. But convex arrays can limit this problem.

Convex array

By placing the elements on a convex surface a larger area can be scanned by a smaller number of arrays elements. The principle of imaging is the same as for the linear array by translating the active sub-aperture. In that case, the region of scanning is in sectorial geometry. A typical application of this kind of imaging is to check fetal development. But in some cases, linear arrays and convex arrays cannot be used. For echocardiography imaging, smaller arrays called the phased arrays are used due to the specific configuration of the heart behind ribs.

Phased array

Phased arrays are small squares probes, enabling to imaging through a larger sectorial region. All elements of arrays are used to transmit and to receive. The direction of beam is controlled by the delay of signals which is so called phased arrays. It is also doing sector scan, and a classical application is echocardiography.

Recently, more advanced transducers have been developed. The number of elements is always increasing, and two dimensional arrays begin to be less uncommon.

In all different kinds of arrays, beamforming can be used in emit and receive in order to improve the contrast, depth of field or more generally to control the characteristics of the ultrasound image.

2.2.3 Different modes of echography

A-Mode (Amplitude)

A-mode is the oldest and simplest way of pulse echo method. The received signals by multi-channel system are combined to form a single line of propagation. The display on the screen with gray or color scale depends on the amplitudes of the signals. As be presented in Fig. 2-5, the ordinate corresponds to the amplitude of the RF signal, and the abscissa reflects the time of reception, which depends on the distance and the propagation velocity of acoustic waves. Mode A is not used for identifying the structure of an object, but for measuring the time delay and therefore the distance between the echogenic structures.

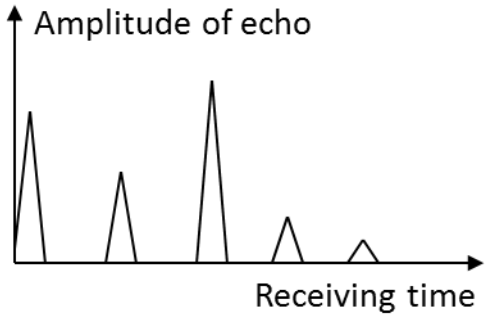

Fig. 2-5 : Representation of signal of Mode A

M-mode (Motion)

M mode is an extension of mode A, which is presented in Fig. 2-6. It is used for visualizing the motion of an object as be seen in Fig. 2-6. In M-mode, the evolution of A-mode line can be seen clearly. First, the transducer is fixed and it sends beams consecutively to detect the object, the left line brings the origin position information of the object colored gray. The movement of object is reflected by the motion of echoes which corresponds to the right line and carries the position information for the displaced object colored black. The straight line of echo presents the still part of echogenic structure, and the amplitude mutation demonstrates the distance of the object to the transducer. Thus the motion of the object can be represented by juxtaposing the A-mode successive signals.

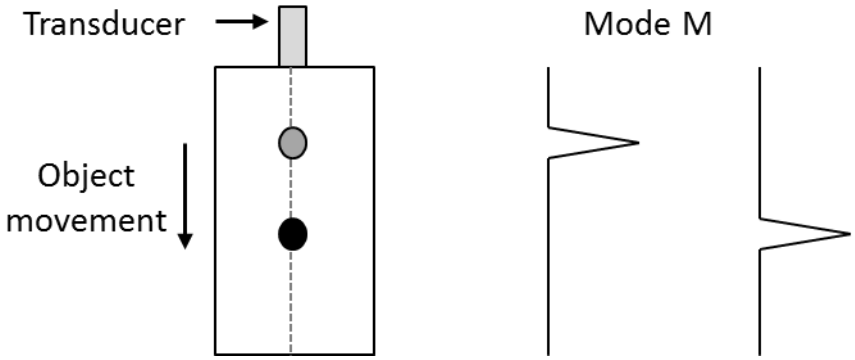

Fig. 2-6 : Principe of imaging with Mode M

Mode B (Brightness)

The currently most widespread acoustic imaging system is the B-mode (shown in Fig. 2-7). It is also another representation of A lines. By displacing the transducer on the detected object along the scanning direction see in the left image, a large number of reflecting A lines are obtained, and the two dimensional image is constructed by juxtaposing the lines in the direction of scanning. As be displayed in the right image,

each line corresponds to horizontal position along the scanning direction, and the vertical information of A line reflects the detected depth/time. Therefore, the distribution of acoustic impedance discontinuities of the object is a two dimensional echogram.

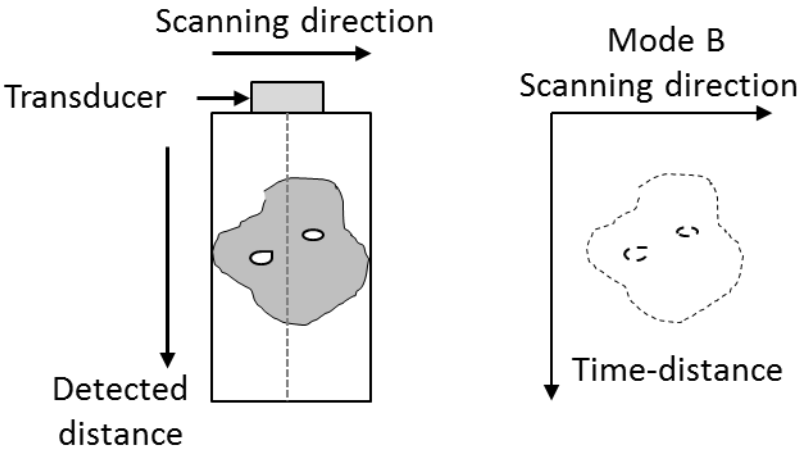

Fig. 2-7 : Presentation of imaging with Mode B

C-Mode (Constant depth)

C-mode (as be shown in Fig. 2-8), represents the image acquired at a "constant depth", which is in a plane perpendicular to the direction of wave propagation. The scanning beam is focused on the point at a constant distance along the propagation beam axis, thus display a plane in that sense. Particularly, this could be realized by controlling the time delay in emission. And the brightness of the spot is proportional to the amplitude of the echo.

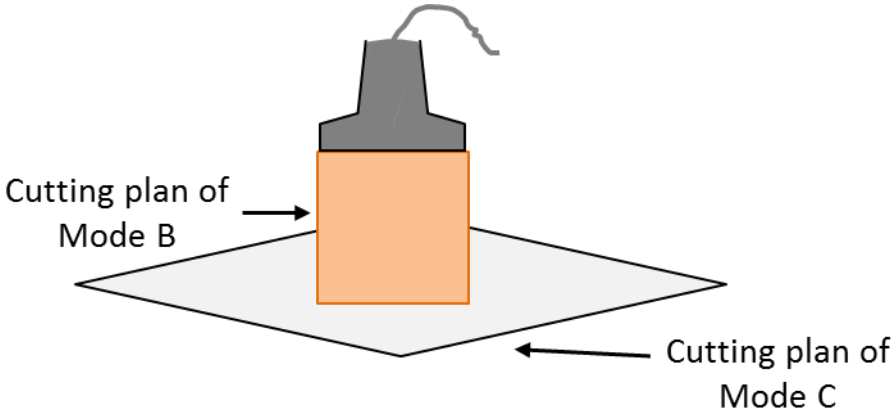

Fig. 2-8 : Cutting plan of Mode B and Mode C

2.3 Point spread functions

The PSF is an image that would be generated by only one scatterer of unitary amplitude, allowing the resolution in all directions to be observed. Assuming linearity of the imaging system, and the medium is composed by a collection of scatterers, the image formation of medium can be seen as the sum of a collection of PSF. The PSF can be modeled as a three dimensional function denoted as h(x, y, z). For simplicity, one can assume the PSF to be separable [32] in the three spatial dimensions as:

$$h(x,y,z)=h_x(x)h_y(y)h_z(z) \tag{1.1}$$

The axial profile $h_z(z)$ is related to the excitation pulse and to the electro-mechanical impulse response of the elements. The lateral profile $h_x(x)$ and the elevation profile $h_y(y)$ are governed by diffraction and interference effect. $h_x(x)$, $h_y(y)$ and $h_z(z)$ are also separable, one term corresponding to the emit process and one to the receive process, which can be expressed as follows:

$$h_x(x)=h_{xe}(x)h_{xr}(x) \tag{1.2}$$

$$h_y(x)=h_{ye}(y)h_{yr}(y) \tag{1.3}$$

$$h_z(z)=h_{ze}(z)h_{zr}(z) \tag{1.4}$$

Where $h_{xe}(x)$ and $h_{xr}(x)$ correspond to the lateral profile in emission and in reception respectively. $h_{ye}(y)$ and $h_{yr}(y)$ are the emission and reception profile in elevation direction separately, $h_{ze}(z)$ and $h_{zr}(z)$ denote the axial profile in emission and in reception correspondingly.

2.4 Conclusion

In order to provide readers a basic knowledge of ultrasound imaging, this chapter describes the general concepts in the first place, and then gives gradual in-depth explanations of the principle of echography, the imaging principle of a transducer, different types of imaging arrays for specific applications. In the next chapter we will introduce the basics of beamformer design methods.

Chapter 3

State of the art of Beamforming

Contents

In chapter 2, the principle of ultrasound imaging has been presented, and the limitation of echocardiography has been explained in chapter 1. In this chapter, the beamforming technique will be introduced clearly since it will influence the quality/appearance of the images and as a consequence it influences the motion estimation accuracy in echocardiography. First, the general beamforming techniques will be presented. Then the works for specific transverse oscillations beamformer design which have been done will be described.

3.1 General beamforming design techniques

Beamforming is the name of the signal processing technique used to construct one beam from the combination of the single transducer beams. The evolution of ultrasound beamformers [33] experiences a long time, the most commonly used beamformer is the delay-and-sum beamformer, see in Fig. 3-1 and Fig. 3-2. Further, with the development of technology, the advanced beamforming, including the synthetic aperture imaging [34], parallel receive beamforming [26], compounding [35, 36] and adaptive beamforming [37], etc., are proposed in order to meet different needs. These beamformers will be illustrated in this section.

Delay-and-sum beamformer

The delay-and-sum beamformer, although it is the simplest way of signal processing, it is still the most powerful way to do signal processing. It can be designed both in transmission (Fig. 3-1) and in reception (Fig. 3-2).

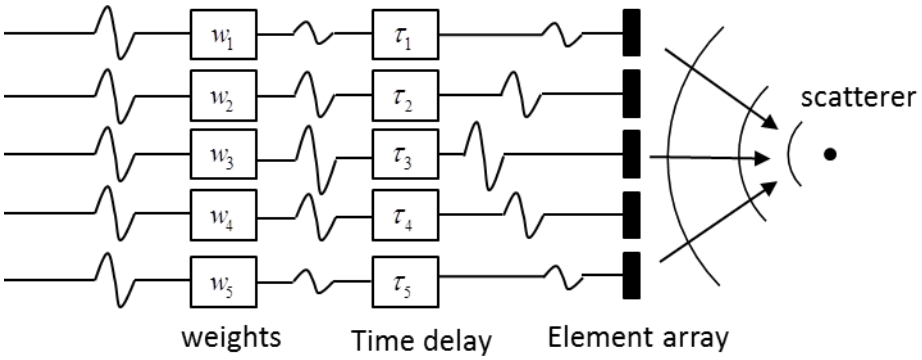

Fig. 3-1: Presentation of the principle of delay-and-sum beamformer in transmit mode

As seeing in Fig. 3-1 and Fig. 3-2, w_i are the weighting coefficients to the signals, which if used in transmission to change the emitted pulse field for example minimize unwanted lobes, or in reception to create a specific spatial schema; τ_i is the time delay depending on the distance from the diffuser to the element.

In transmission, the signals are first weighted, which changes the amplitude of the signals, then the time delay is imposed for focusing at different points; in reception, the received signals are first be delayed and apodized, afterwards, all the signals are summed up to as one final signal.

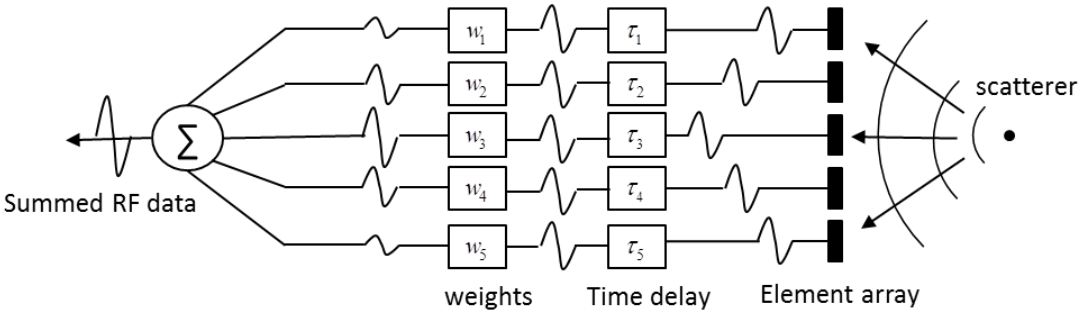

Fig. 3-2: Presentation of the principle of delay-and-sum beamformer in receive mode

Synthetic aperture imaging

Synthetic transmit aperture imaging (as be described in [34]) is achieved by using an aperture with a fixed number of elements. A single element is used for transmitting and all\part of the elements are used in reception to form a so called low resolution image. This will be done sequentially for each element in transmission, the final result is a sum of all the images. Since all elements transmissions are separated, transmit beamforming can be performed in post-processing. This enables for example to produce transmit dynamic focusing. Unfortunately the acquisition of a full synthetic aperture dataset can be longer than a conventional imaging strategy. By using a sparse set of emission, the frame rate and pulse repetition time could be dissociated, thereby a fast imaging albeit with lower resolution will be constructed. The synthetic aperture can also be used in radar system [38] and optical domain [39].

Parallel receive beamforming

Parallel receive beamforming [26] is used to increase the frame rate and so ideal for cardiac imaging. With this technique, a broad beam is transmitted, and multiple receives are formed. It is most useful for imaging deep tissue, or when real-time 3-D imaging is desired. It is now one of the most active research domains, and has already been widely used in elastography [40] etc.

Compounding

By using this technique, the effects of speckle/noise can be reduced. In compounding, multiple images of the same target are averaged in order to reduce the coherent noise. Here are the different ways to obtain the images: 1) by changing the

steering direction [36]; 2) by physically translating the transducer [35]; 3) and by changing the transmit frequency [41]. In this case, each image contains uncorrelated noise patters, therefore reducing the noise.

Adaptive beamforming

Adaptive beamformer is used to destruct the directionality of signals to/from undesired directions. Because the undesired signals can reduce image qualities, obscure targets and bring image artifacts. This technique can be realized by introducing least mean squares algorithm, maximum likelihood method and sample-Matrix Inversion algorithm, etc., these techniques have been explained in [42].

The general beamforming techniques have been introduced above, but there are still some specific beamformer design techniques for specific aims. For example, improving the system detected depth of field [43-45], reducing the field level to avoid potential hot spots [46], and minimizing undesired beamforming artifacts due to blocked elements which exists using large aperture [47].

This thesis is focused on a specific beamformer design method [48] aiming at improving imaging resolution which can further improve motion estimation accuracy in echocardiography. This specific beamformer design method is based on the most common delay-and-sum beamformer in receive. By using different weighting functions, a specific schema with transverse oscillations can be created, which permits better resolution in lateral direction. This approach will be presented in the next section.

3.2 Beamforming for transverse oscillations

The principle of the TO technique is to modify image formation by using a beamformer that is able to produce a pulse-echo sound field featuring axial and transverse oscillations, whereas conventional beamformers lead to axial oscillations only. The very interesting consequence is that the signature of the backscattered signal received from a moving group of ultrasonic scatterers crossing such a sound field will carry information about both the axial and the transverse velocity. How these images are obtained and exploited as well as their potential for different applications has been summarized in a short review in [49].

3.2.1 Approaches based on the Fraunhofer approximation

Fraunhofer approximation [50] concerns the far-field or focal point region. It supposes that under most circumstance in medical imaging, the propagation of

monochromatic signal is a linear operation, and it has a transfer function which is the Fourier transform to the impulse response, which can be simply expressed as

$$h_{xr}(x) = FT\left\{\frac{w(x)}{\lambda y}\right\} \tag{3.1}$$

where FT stands for the Fourier transforming, $w(x)$ is the apodization function; λ is the wavelength of emitted signal, y is the depth of the PSF and $h_{xr}(x)$ is the lateral profile of the PSF.

On the basis of Fraunhofer approximation, the apodization function is the inverse Fourier transform of the desired profile and is given as

$$w(x_i) = k^{-1} \cdot FT^{-1}[h_{xr}(x)] \tag{3.2}$$

where FT^{-1} stands for the inverse Fourier transform, the $w(x_i)$ stands for the apodization function with respect to the lateral position at the depth of y of the ith element, k is a coefficient regrouping constant coefficients and having the dimension of length over the lateral profile of $h_{xr}(x)$.

It works well in linear geometry as presented by Jensen in estimation of velocity vectors [19], and Liebgott and Ben Salem [51] have planted it in sector scan, but they only imposed the apodization function that calculated in linear geometry to elements which did sectorial scanning. So it doesn't adapt well for sectorial scan.

3.2.2 Sumi's approach

In order to search for a high lateral resolution and accurate measurement of displacement, Sumi proposed a Lateral Cosine Modulation Methods (LCMs) in [52], where the apodization function in transmission is superimposition of two Gaussian functions and two parabolic functions in reception. These apodization functions are also obtained using the Fraunhofer approximation such that the transmitted US energy used is the same when realizing the Gaussian-type lateral PSF.

LCM permits complete freehand measurements and reconstructions in one, two and three dimension motion measurements. But it doesn't work well when small steering angles must be used.

3.2.3 Transverse oscillations in linear geometry

The 2D PSF system incorporating the desired TOs is assumed to be separable [53] for both directions as well as for the transmit and receive scheme as given in (3.3)

$$h(x,y) = h(y)h_e(x)h_r(x) \tag{3.3}$$

where $h(y)$ is the axial pulse-echo profile of the impulse response, $h_e(x)$ and $h_r(x)$ are the transmitted and received lateral profiles, respectively.

Our beamformer design mainly focuses on lateral profiles. Moreover, the transmit scheme can be considered as having little influence on the final image formation if a plane wave is emitted by making a focus in the far-field. As a consequence, we consider beamforming during receive.

In linear geometry, lateral oscillations correspond to the lateral profile expressed in (3.4), which is a multiplication of a Gaussian envelope with a cosine function. In this equation, λ^{PSF} is the expected wavelength of the transverse oscillations, σ^{PSF} is the half maximum width of the Gaussian envelope that limits the extent of the PSF, and $u^{PSF} = 1/\lambda^{PSF}$.

$$h_r(x) = \cos(2\pi x u^{PSF}) \cdot \exp(-\pi(\frac{x}{\sigma^{PSF}})^2) \tag{3.4}$$

The conventional beamforming used to obtain the profile expressed in (3.4) is based on Fraunhofer approximation, the conditions of which are met at the focal point. If a broad beam is emitted, $h_e(x)$ in (3.3) can be considered to have no influence on the final point spread function (it can be considered as close to 1). This can be obtained by emitting a plane wave, as explained by Jensen and Munk in [19]. In this case the Fraunhofer approximation holds along the whole propagation path, because the system lateral impulse response is equal to the term in receive as in equation (3.4) and the dynamic focus is performed for all depths in receive. Under this approximation, the transverse profile of the PSF at the focusing depth is related to the apodization function by a Fourier transform [50]. In this setting, the apodization function is thus obtained as the inverse Fourier transform of the PSF profile and is written as follows:

$$w(x_i^{Apo}) = \frac{1}{2}(\exp^{-\pi(\frac{x_i^{Apo}-x^{Apo}}{\sigma^{Apo}})^2} + \exp^{-\pi(\frac{x_i^{Apo}+x^{Apo}}{\sigma^{Apo}})^2}) \tag{3.5}$$

where x_i^{Apo} is the lateral position of the ith element, $\pm x^{Apo}$ are the positions of the two peaks and σ^{Apo} is the half maximum width of each peak. The parameters in (3.5) can be related to the PSF parameters of (3.4) and the depth y as

$$x^{Apo} = \lambda y / \lambda^{PSF} \tag{3.6}$$

$$\sigma^{Apo} = \sqrt{2}\,\lambda y / \sigma^{PSF} \tag{3.7}$$

where λ is the wavelength of the transmitted pulse. The lateral PSF profile in (3.4) and the apodization function in (3.5) are represented in Figure 1.

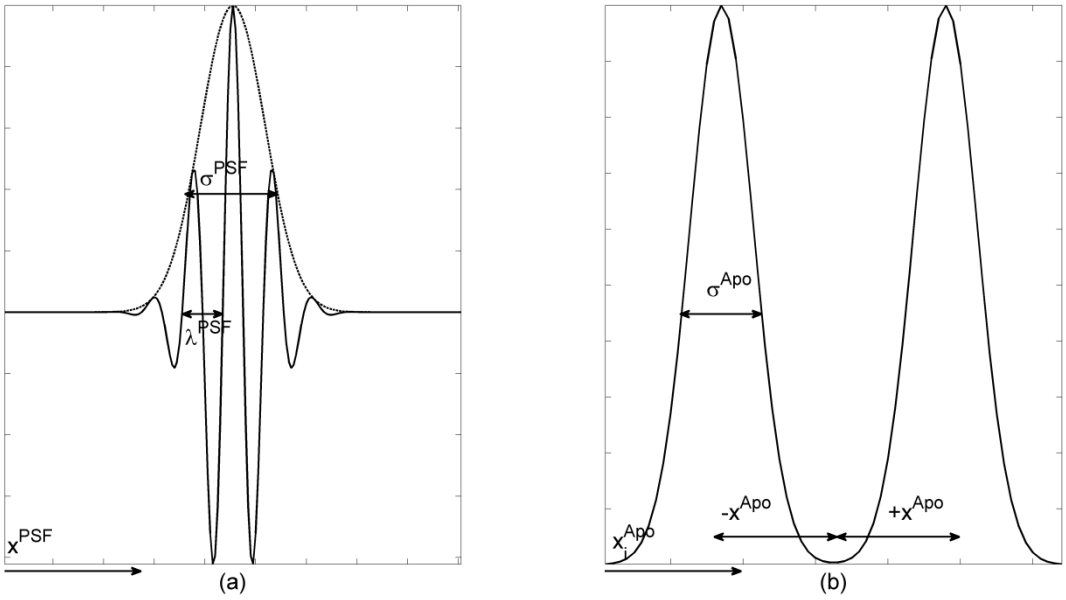

Fig. 3-3 : Representation of the different variables of the lateral profile of the PSF (a) and the apodization function (b). The relations between x^{Apo} and $u^{PSF} = 1/\lambda^{PSF}$ as well as between σ^{Apo} and σ^{PSF} are given in (3.6) and (3.7).

The above framework has been studied in [30, 51] in terms of motion estimation in echocardiography, wherefore the feasibility of TOs for sectorial geometry has been tested. In order to adapt it to sectorial geometry, we use a configuration which transforms the parameters λ^{PSF} and σ^{PSF} in Cartesian coordinates into corresponding parameters in polar coordinates as λ_θ^{PSF} and σ_θ^{PSF} in the next part 3.2.4.

3.2.4 Transformation of Transverse oscillations to sectorial geometry

In order to adapt the above framework to sectorial geometry, we transform the model parameters from Cartesian to polar coordinates [48]. This is done by setting:

$$\lambda^{PSF} = \lambda_{\theta}^{PSF} \cdot r \tag{3.8}$$

$$\sigma^{PSF} = \sigma_{\theta}^{PSF} \cdot r \tag{3.9}$$

where λ_{θ}^{PSF} is the expected lateral wavelength of the PSF profile in angles, σ_{θ}^{PSF} is the width at the half maximum of the PSF lateral profile, and r is the sweeping radius. Based on (3.6) and (3.7) and making the approximation that $y = r$, the position of the two peaks $\pm x_{\theta}^{Apo}$ and the standard deviation σ_{θ}^{Apo} (which are both expressed in [m])of the apodization function are then given as follows:

$$x_{\theta}^{Apo} = \lambda / \lambda_{\theta}^{PSF} \tag{3.10}$$

$$\sigma_{\theta}^{Apo} = \sqrt{2}\lambda / \sigma_{\theta}^{PSF} \tag{3.11}$$

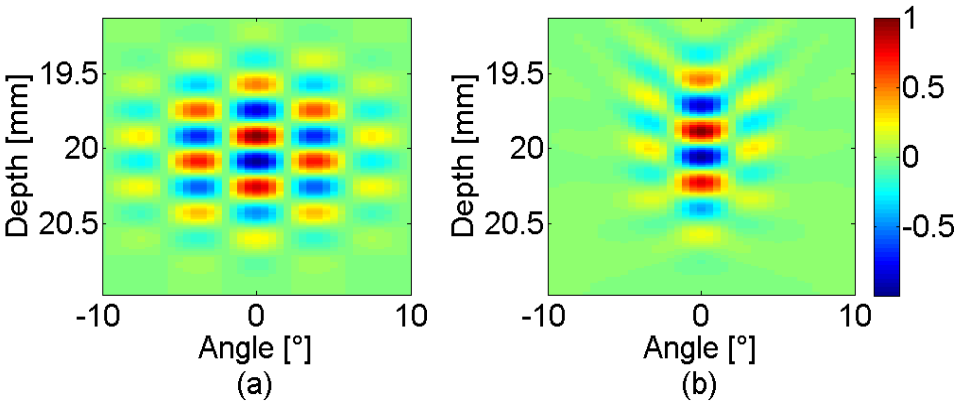

Fig. 3-4: Presentation of theoretical PSF in (a) and the PSF obtained using Fourier relation

Here in Fig. 3-4 is an example of the theoretical PSF in (a) and the obtained PSF using Fourier relation in (b), the abscissa varies with angles which are the situation in sectorial scanning. As can be observed, the shape of obtained PSF is not satisfied because the Fourier relation is proposed under Fraunhofer approximation, which is not adaptive in sectorial scanning. So in next chapter, an adapted method which is the contribution of this thesis is proposed to solve this problem.

3.3 Conclusion

Looking into equations (3.10) and (3.11), the apodization function to the probe is due to only the wavelength of the transmitted pulse λ, the expected lateral wavelength of the PSF profile in angles λ_{θ}^{PSF}, and the width at the half maximum of

the PSF lateral profile σ_θ^{PSF}. The center frequency of transmitted pulse by other means the λ is decided for the compatible to echocardiography, so as limited to the small size of phased array probe, we need to expand the λ_θ^{PSF} and σ_θ^{PSF}.

All the methods that have been mentioned above are very good, but there exist a problem that the precision in lateral direction is not satisfied enough as shown in Fig. 3-4, moreover, the previous techniques were only studied in linear geometry, but for most applications a sectorial scan is definitely essential. In meeting with these demands, we propose a transverse oscillations beamformer design using back-propagation which is adaptive with the changes of directions of scanning beam in sectorial scan and has a better resolution in lateral direction. We will show all methodology in next chapter.

Chapter 4

Back-propagation beamforming design

Contents

4.1 Introduction

This chapter focuses on the main contribution of this thesis–the back-propagation method and the adaptation of TOs to sectorial geometry.

As adaptation of back-propagation method with TOs to echocardiography has been proposed in [30, 51]. More recently another group has also used TOs with a phased array but to estimate vector flow [54]. They even extended the concept to be used with a matrix phased array [55]. These studies yielded relative good performance, however they use the same apodization function for all beams.

With the aim of respecting better the real physics of wave propagation in echocardiography, we propose a specific beamformer design method based on back-propagation (BP) and reciprocity theorem, under which the parameters depend on the beam direction. This approach allows for more accurate results in sectorial geometry.

This chapter has been organized as: First, the general two principles of wave propagation theory and the reciprocity theorem are introduced, which are the basics of back-propagation method. Then the explanations in details for introducing transverse oscillations beamformer design to back-propagation method and the conversion to sectorial geometry will be presented.

4.2 Principle of back-propagation method

4.2.1 Wave propagation theory

Ultrasound is a mechanical wave, it propagates through the medium, for example air molecules or human body. Ultrasound is longitudinal wave, which in the case of plane waves means the vibration of the medium is parallel to the direction of propagation. In 2D, the propagating signal is given as

$$e(\mathbf{s},t) = \exp(j(\omega_0 t - \mathbf{k}\cdot\mathbf{s})) \tag{4.1}$$

where the elemental function of ultrasound wave is characterized by the wavenumber k and the angular frequency w_0. s is the directional position of the point of interest and t is the observation time. Here the $\mathbf{s}=(x,y)$ and $\mathbf{k}=(k_x,k_y)$. As the actual pressure field is a combined effect of all ultrasound waves, the 2D+t (space and time) pressure field can be given as

$$p(\mathbf{s},t)=\frac{1}{(2\pi)^3}\iiint_{-\infty}^{+\infty}A(\mathbf{k},\omega)\exp(j(\omega t-\mathbf{k}\cdot\mathbf{s}))d\mathbf{k}d\omega \tag{4.2}$$

where $A(\mathbf{k},\omega)$ is the amplitude of each elemental wave, $p(\mathbf{s},t)$ is the combined pressure field. Equation (4.2) is valid only when it satisfies the condition that

$$\omega^2=c^2|\mathbf{k}|^2=c^2k^2 \tag{4.3}$$

Equation (4.3) is valid only for lossless medium which is the assumption in this thesis. After introducing the coordinate (x,y) and equation (4.3) into (4.2) and assuming the observation time is equal to $t=0$, $\mathbf{k}\cdot\mathbf{s}=|\mathbf{k}|\cdot|\mathbf{s}|\cos\theta=\frac{\omega}{c}\cdot r\cdot\cos\theta=\frac{2\pi r}{\lambda}$ when the elevation angle $\theta=0$ in the 2D surface, $\omega=2\pi f$ and $c=\lambda f$, then the pressure $p(x,y)$ got at the point of interest is

$$p(x,y)=\frac{1}{(2\pi)^2}\iint_{-\infty}^{+\infty}A(x,y)\exp(-j\frac{2\pi r}{\lambda})dxdy \tag{4.4}$$

where $A(x,y)$ is the amplitudes of signals at the point of interest, r is the distance from the source to the point of interest.

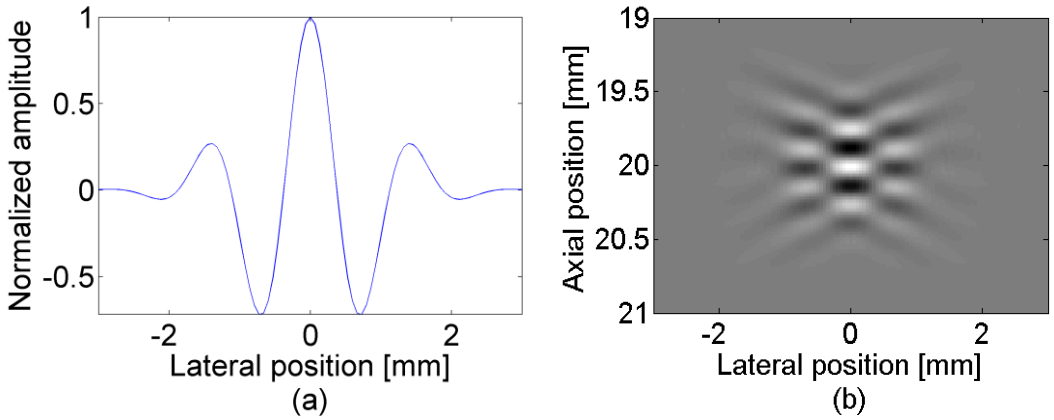

Fig. 4-1: Presentation of the impulse response of the probe in (a) and the generated pressure field in (b) at the depth of 20 mm. The parameters are the number of elements is 128, the center frequency is $f_0=6MHz$.

Fig. 4-1 illustrates the equation(4.4), which indicates that if the signal source is a probe with 128 elements, the signal center frequency is 6 MHz, if the system impulse response is as given in (a), the pressure field obtained at the depth of 20 mm is like in Fig. 4-1 (b).

4.2.2 Reciprocity theorem [56]

The back-propagation method is based on the reciprocity theorem [56]. It is a theorem which states that in the acoustic field due to a sound source, the sound pressure received at any other point of interest is the same as that which would be produced at the position of source point if the waves got at the point of interest be back-propagated, and that this can be generalized for multiple sources and receivers.

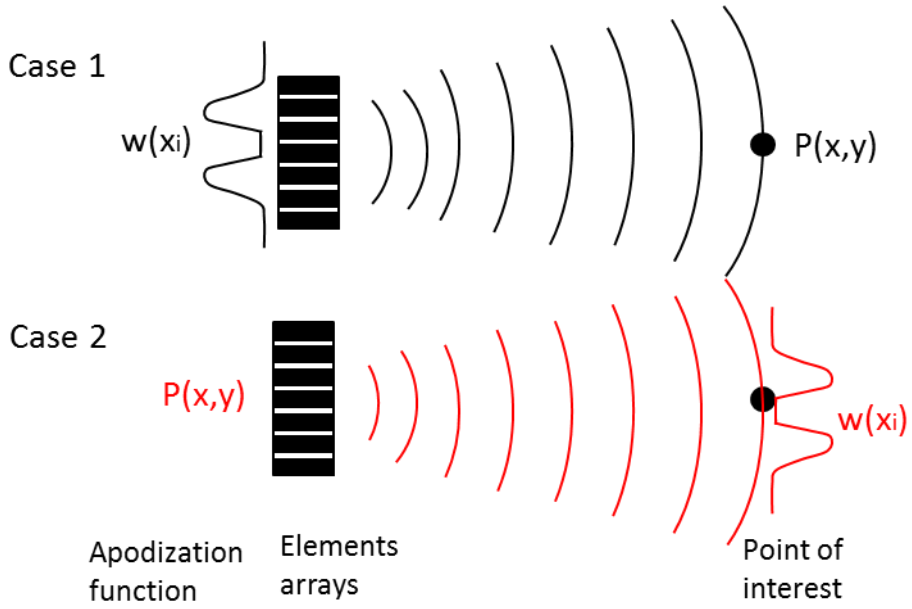

Fig. 4-2 : Presentation of reciprocity theorem: Case 1 presents that after the elements arrays apodized by $w(x_i)$, the pressure field obtained at the point of interest is p(x,y); Case 2 indicates that if the pressure field p(x,y) is used as apodization function like $w(x_i)$ in case 1, the the pressure field received at the point of interest are equal to $w(x_i)$ as presented in case 1.

Applying this theorem to the ultrasound probe and point of interest, as be shown in Fig. 4-2: case 1, the emitted signals are weighted by $w(x_i)$, then the pressure field at the point of interest is P(x,y); under the reciprocity theorem in case 2, if the emitted signals are weighted by P(x,y) , the pressure field obtained at the point of interest represents the same pressure profile as $w(x_i)$.

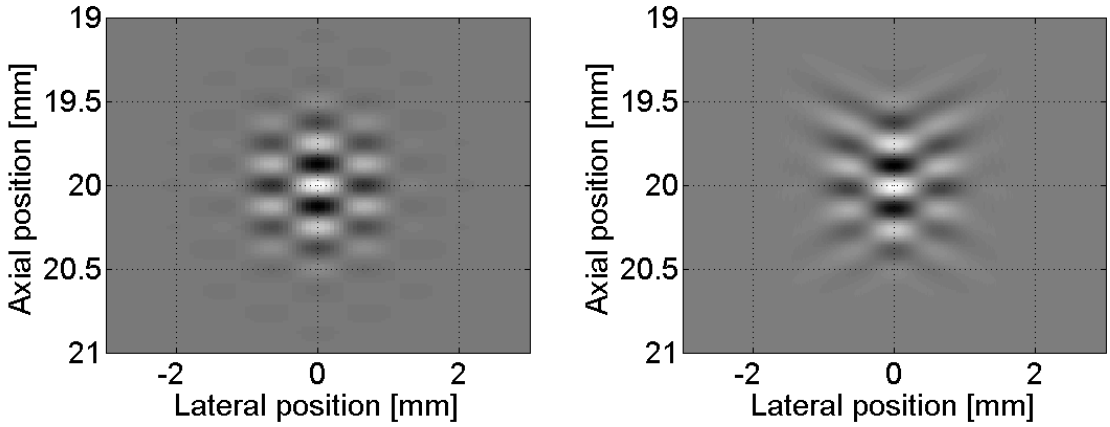

Fig. 4-3: Presentation of PSF in linear geometry: (a) is the theoretical one and (b) is the PSF simulated using back-propagation method. The parameters are the center frequency is set as $f_0 = 6MHz$, the lateral wavelength of PSF is $\lambda_x = 1.5mm$ and the half maximum width of the Gaussian envelope is $\sigma_x = 1.5\lambda_x$, the number of elements is 128.

Fig. 4-3 presents the results under reciprocity theorem using PSF. The theoretical PSF in (a) signifies the pressure field given in Fig. 4-2 the case 2, using the apodization function attained by back-propagating it to the probe, the pressure field presented in Fig. 4-3 the case 1 is demonstrate by the simulation PSF in Fig. 4-3(b).

4.3 Transverse oscillations beamformer design

In the section of 4.2, the wave propagation principle and the reciprocity theorem have been described, which is the basic of the back-propagation method. Then in this section, the transverse oscillations beamformer design using back-propagation method and the adaptation to sectorial geometry which is the truth in echocardiography would be presented.

4.3.1 TO beamformer design for back-propagation

As the conditions of Fraunhofer approximation as be describe in the subsection 3.2.1 are not 100% satisfied see in Fig. 3-4, because the Fraunhofer approximation assumes the propagation of monochromatic signal is a linear operation, under which it assumes the apodization function is the inverse Fourier transform of the PSF profile, but it is not the case especially in sectorial geometry, the inverse Fourier transform is then just an approximation of the back-propagation, This limitation leads us to propose a new TOs beamformer design using the back-propagation method, this method recalculates the apodization function without Fraunhofer approximation, which should better represent the physics of the problem, thereby be better adapted to

sectorial geometry and could yield a more precise PSF than the conventional beamformer design.

The PSF pressure field at the focus can be considered as the combined effect of all ultrasound pulses sent by all the aperture elements. Since the ultrasound propagation function from the ith element to a point of interest can be modeled as a Green function [50] one can relate the pressure in front of all elements of a linear array $p_0(x_i)$ to the pressure $p(x,y)$ at depth y and lateral position x in the medium by the following integral over the full surface of the probe Φ

$$\mathrm{p}(x,y)=\frac{1}{j\lambda}\int_{\Phi}p_0(x_i)\frac{e^{-\frac{j2\pi \mathrm{r_i}}{\lambda}}}{r_i}ds \tag{4.4}$$

Considering that the pressure in front of an element is directly proportional to the apodization function of each element $p_0(x_i)=kw(x_i^{Apo})$ and rewriting this integral as the discrete sum of the contributions from all elements,

$$\mathrm{p}(x,y)=\frac{1}{j\lambda}\sum kw(x_i^{Apo})\frac{e^{\frac{j2\pi r_i}{\lambda}}}{r_i}\Delta s \tag{4.4}$$

After regrouping all constant coefficients in one single constant $k_1=\frac{k\Delta s}{j\lambda}$, one obtains the following equation

$$p(x,y)=k_1\sum_{i=1}^{N}w(x_i^{Apo})\frac{e^{\frac{j2\pi r_i}{\lambda}}}{r_i} \tag{4.5}$$

where N is the number of active elements, k_1 has the dimension of pressure times length. x_i^{Apo} is the position of ith element, r_i is the distance from the ith element to the point of interest, and $w(x_i^{Apo})$ the apodization function. The 2D PSF pressure field in linear geometry with transverse oscillations is presented in Fig. 4-4, the abscissa denotes the lateral position in Cartesian coordinate, and the axial potion is in the ordinates. The PSF is obtained with signals with a frequency of 6 MHz, the expected lateral wavelength of the transverse oscillations is $\lambda^{PSF}=1.5mm$, and $\sigma^{PSF}=1.5\lambda^{PSF}$ is the half maximum width of the Gaussian envelope.

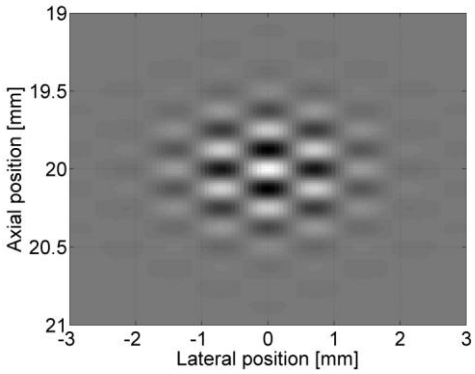

Fig. 4-4: 2D PSF pressure field at the depth of 20mm with transvers oscillations in linear geometry. The parameters are the center frequency $f_0 = 6MHz$, the expected lateral wavelength of the transverse oscillations is $\lambda^{PSF} = 1.5mm$, and $\sigma^{PSF} = 1.5\lambda^{PSF}$ is the half maximum width of the Gaussian envelope.

Under the reciprocity theorem[56], the function in (4.5) can be reversed. This leads to a relation giving the pressure that would be observed at the position of the aperture elements when the apodization function is applied at (x,y). This approach is thus called the back-propagation and can be expressed as

$$w(x_i^{Apo}, y_0) = k_2 \int_{-\infty}^{+\infty} p(x, y_0) \frac{e^{\frac{j2\pi r_{i0}}{\lambda}}}{r_{i0}} dx \tag{4.6}$$

where y_0 is the depth of interest, k_2 is a coefficient regrouping all constant coefficients and having the dimension of length over pressure. $p(x, y_0)$ is the pressure profile at the depth of interest, and r_{i0} is the distance from ith element to the point of interest, which can be given as

$$r_{i0} = \sqrt{(x - x_i)^2 + y^2} \tag{4.7}$$

The apodization function obtained using one lateral profile of the PSF given in Fig. 4-4 is presented in Fig. 4-5, where the figure (a) demonstrates the apodization function for different elements and it varies with the PSFs' depth from 15 mm to 70 mm. Figures (b, c, d) give the apodization profiles at the depth of 23mm, 35 mm and 48 mm respectively. In this case the reader can understand clearly that the apodization varies with depth.

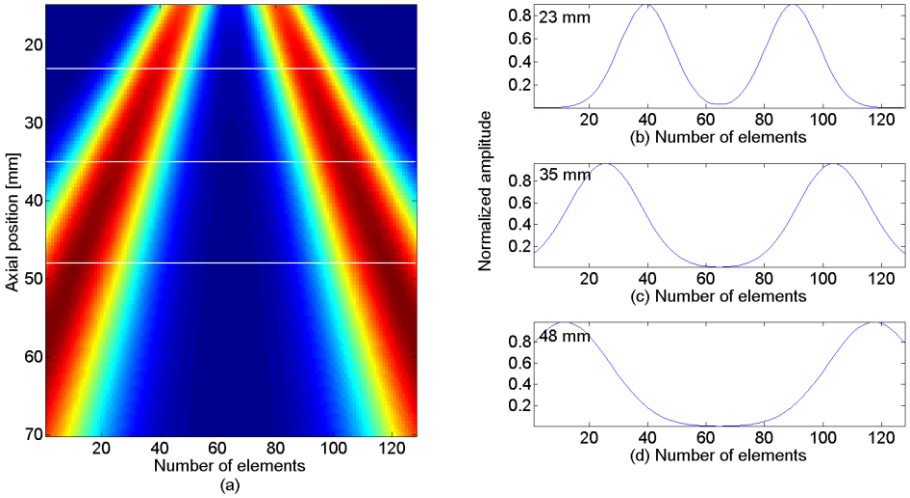

Fig. 4-5: Presentation of apodization function obtained using back-propagation from the depth 15mm to 30mm using 128 active elements in (a). Figures (b, c, d) give the apodized profiles obtained at the depth of 23mm, 35mm and 48mm respectively.

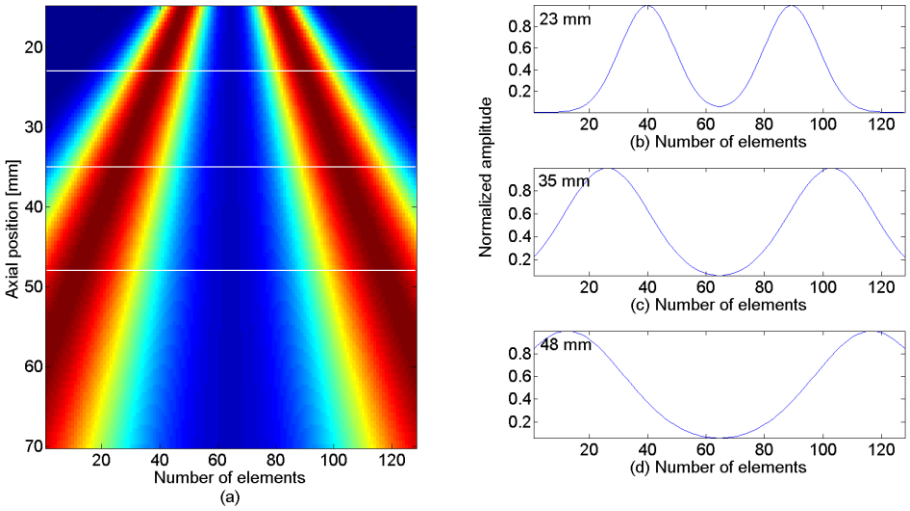

Fig. 4-6: Presentation of apodization function obtained using Fraunhofer approximation from the depth 15mm to 30mm using 128 active elements in (a). Figures (b, c, d) give the apodized profiles obtained at the depth of 23mm, 35mm and 48mm respectively.

Using one lateral profile of the PSF given in Fig. 4-4, the apodization function calculated by Fraunhofer approximation is shown in Fig. 4-6. By comparing with Fig. 4-5, we can see that the apodization function acquired under back-propagation and Fraunhofer approximation is quite similar. The peaks are symmetric, the distance between the peaks as well as the width of each peak increase with depth. Moreover, as can be concluded from the Fig. 4-4 - Fig. 4-6, if we keep the lateral wavelength $\lambda^{PSF} = 1.5mm$ and the half maximum width of the Gaussian envelope $\sigma^{PSF} = 1.5\lambda^{PSF}$ the same for all positions, the apodization function will be destroyed in deeper depth, see in Fig. 4-5 (d) and Fig. 4-6 (d).

Both the pressure field of $p(x,y)$ and the apodization function $w(x_i^{Apo}, y_0)$ are expressed for a linear geometry configuration. Considering the ground truth in echocardiography, which is the detected depth is up to 150mm and the scanning region a sector, an adaptation configuration will be presented in the following section.

4.3.2 Conversion to sectorial geometry

Adapting the TOs with back-propagation method to sectorial geometry, the distance from ith element to the point of interest is given as

$$r_{i0}(i,\theta) = \sqrt{(r\sin\theta)^2 + (r\cos\theta + x_i)^2} \tag{4.8}$$

$$\tan\theta = \frac{x - x_i}{y} \tag{4.9}$$

where $r = \sqrt{x^2 + y^2}$ is the beam radius from the central element to the point of interest, θ is scanning angle which is defined as the angle between elements array and the beam. Then the pressure field and apodization function can be transformed into a polar coordinate as follows:

$$p(\theta, r) = k_1 \sum_{i=1}^{N} w(x_i^{Apo}) \frac{e^{\frac{j2\pi r_i}{\lambda}}}{r_i} \tag{4.10}$$

$$w(x_i^{Apo}, r_0) = k_2 \int_{-\infty}^{+\infty} p(\theta, r_0) \frac{e^{\frac{j2\pi r_0(i,\theta)}{\lambda}}}{r_0(i,\theta)} d\theta \tag{4.11}$$

where $p(\theta, r)$ is the pressure field changes with angle θ and the distance from the aperture to the position of interest r, k_1 and k_2 are constants, x_i^{Apo} is the position of the ith element, r_i is the distance from the ith element to the point of interest; $w(x_i^{Apo}, r_0)$ is the apodization function for a certain scanning radius r_0 that should be used to obtain the pressure $p(\theta, r_0)$, $r_0(i,\theta)$ is the distance from ith element to a point that is located along the scanning radius of r_0 but changes at the same time with angles θ.

Fig. 4-7 gives the PSF obtained in sectorial geometry. The parameters are given as the number of active elements is 128, the center frequency is $f_0 = 2.1MHz$, the expected lateral wavelength of the transverse oscillations is $\lambda^{PSF}{}_{\theta} = 8°$, and

$\sigma_\theta^{PSF} = 1.5\lambda_\theta^{PSF}$ is the half maximum width of the Gaussian envelope. The Fig. 4-7 (a) is presented in polar coordinate, which the abscissa changes with angles, and the Fig. 4-7 (b) is its conversion to Cartesian coordinate, by which means it shows the behavior of angular property.

Keeping the lateral wavelength $\lambda^{PSF}{}_\theta = 8°$ and $\sigma_\theta^{PSF} = 1.5\lambda_\theta^{PSF}$ unchanged, we displace the PSF axially from 30mm to 50mm in front of the arrays elements, in which way the lateral wavelength in units of [mm] in expanded with deeper axial position. Fig. 4-8 (a) illustrates the apodization function obtained over the displaced axial positions, and Fig. 4-8 (b) shows the apodizationd profiles obtained at the axial position of 35mm (in solid blue line) and 45mm (in dotted red line). The two profiles present little difference at different position, so we can say that in sectorial geometry, if keeping the angle of lateral wavelength the same, the apodization function is also has no change.

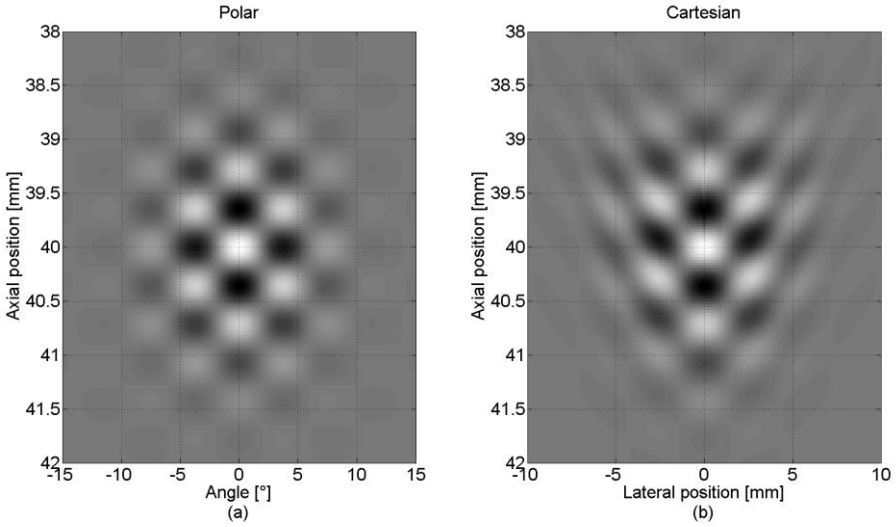

Fig. 4-7: Presentation of PSF obtained in sectorial geometry in (a) and the transformation of it to Cartesian coordinate in (b). The parameters are the center frequency is $f_0 = 2.1MHz$, the expected lateral wavelength of the transverse oscillations is $\lambda^{PSF}{}_\theta = 8°$, and $\sigma_\theta^{PSF} = 1.5\lambda_\theta^{PSF}$ is the half maximum width of the Gaussian envelope.

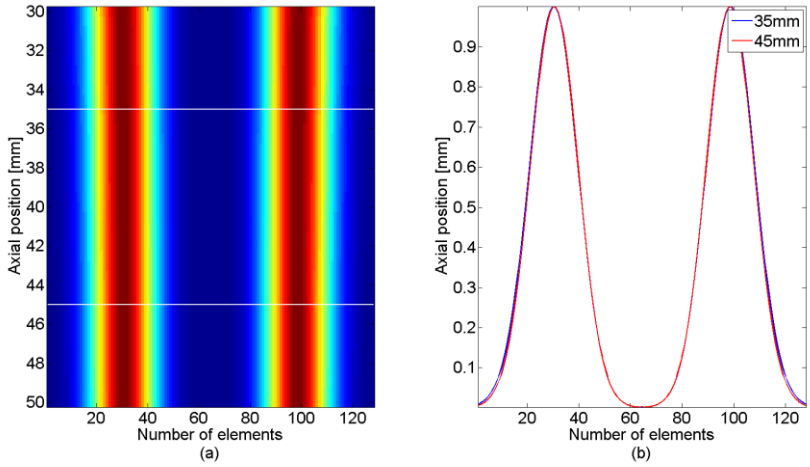

Fig. 4-8: Presentation of apodization function obtained in sectorial geometry. Figure (a) gives the apodization obtained from **depth 30mm to 50mm** with 128 active elements. Figure (b) demonstrates the apodized profiles at the depth of 35mm (solid blue line) and 45mm (solid red line).

By keeping the axial position unchanged at 40mm, we make a further study of the apodization funtion varies with angles. Fig. 4-9 (a) demonstrates the apodization function acquired conver the angle from -30° to 30°, and it shows apparent difference under the comparison of two apodized profiles obtained at symmetry directions of -15° and 15° in Fig. 4-9 (b).

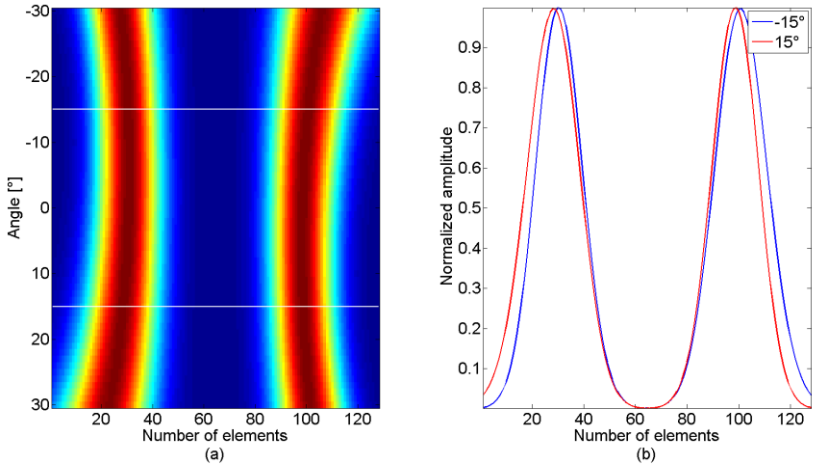

Fig. 4-9: Presentation of apodization function obtained in sectorial geometry, the PSF is displaced from **-30° to 30°** at a certain axial position of 40mm. Figure (a) gives the apodization obtained from -30° to 30° with 128 active elements. Figure (b) demonstrates the apodized profiles at -15° (solid blue line) and 15° (solid red line).

4.4 Conclusion

In this chapter, two basic principles for wave propagation and the reciprocity theorem which the back-propagation stands on are introduced on the first hand, and

then the transverse oscillations beamformer design is related to the back-propagation method as well as the conversion to sectorial geometry. In the next chapter, the simulated results will be illustrated by comparing the proposed back-propagation and the conventional Fraunhofer approximation in terms of evaluating the quality of PSF, the precision of simple motion estimation and the realistic cardiac motion estimation.

Chapter 5

Results

Contents

5.1 Introduction

Chapter 3 presents the readers several methods used for transverse beamformer design, including the classical Fraunhofer approximation, Sumi's method and the adaptation to sectorial geometry of the Fraunhofer approximation approach. Considering the limitation of these methods, we proposed in chapter 4 the back-propagation method using for transverse oscillations in echocardiography.

In this chapter simulations are presented in order to illustrate and quantify the performance of the proposed beamforming strategy. The performance is evaluated both in terms of pure beamforming aspects using PSF simulations and in terms of improvement of motion estimation accuracy.

The apodization functions obtained under two methods will be presented at first, as well as the study on the influence of different parameters, i.e. the lateral wavelength λ_θ^{PSF} and the half maximum width of the Gaussian envelope of PSF σ_θ^{PSF}.

In study of the pure beamforming concerns PSF, the estimated accuracy of simulated PSF to the theoretical one is presented; on the other hand, concerning the improvement for motion estimation, the simple motion estimation in lateral, axial and diagonal directions are first presented separately. At last the results in estimation of movements in realistic cardiac simulations is shown in a parasternal short-axis (Sax) view which correspond to one of the most commonly employed views in the clinical practice[57]. At last, the discussion and conclusion of this chapter will be described in detail.

5.2 Simulation results

Numerical simulations were performed using Field II [58, 59]. The configuration in equations (4.10) (4.11) thus provides the back-propagation beamforming design in sectorial scanning. All the results presented in the following context, both for simulations and experiments, were calculated with configurations given in equations (3.10) (3.11) for Fourier-based and equations (4.10) (4.11) for BP-based beamforming. Unless otherwise mentioned, the simulation parameters are given in Table 1. Note that the use of unfocused emission may decrease the SNR. Our simulation study does not include this evaluation.

Table 1: SIMULATION PARAMETERS

Parameter	Value
Probe type	Phased array
Number of elements	64
Center frequency f_0	2.1 MHz
Sampling frequency f_s	50 MHz
Lateral wavelength λ_θ^{PSF}	8°
Lateral standard deviation σ_θ^{PSF}	12°
Height	12.5 mm
Width	0.14 mm
Distance between two elements	0.03 mm
Focus in transmit	No focus / plane wave

5.2.1 Apodization functions

For purpose of illustration, we give in Fig. 5-1 (a) a 2D representation of the back-propagation apodization function in relation to the scan angle and element number. To compare the difference of the apodization function, Fig. 5-1(b) provides two profiles at two symmetry angles of −30° and 30°. Fig. 5-1(a) shows variations of the lateral profile of the BP-based apodization function with the angle and Fig. 5-1(b) shows a slight asymmetry of the apodization lateral profiles with respect to the central (0°) line.

To compare the difference of back-propagation and the conventional Fourier-based method, we give in Fig. 5-2 a representation of apodization function obtained under the conventional method. Fig. 5-2 (a) is a 2D representation of the Fourier apodization function in relation to the scan angle and element number. As compared to that of Fig. 5-1 (a), the apodization function obtained under Fourier method presents no variation with angles like that obtained under back-propagation method. And the two profiles at two symmetry angles of −30° and 30° in Fig. 5-2 (b) are identity to each other.

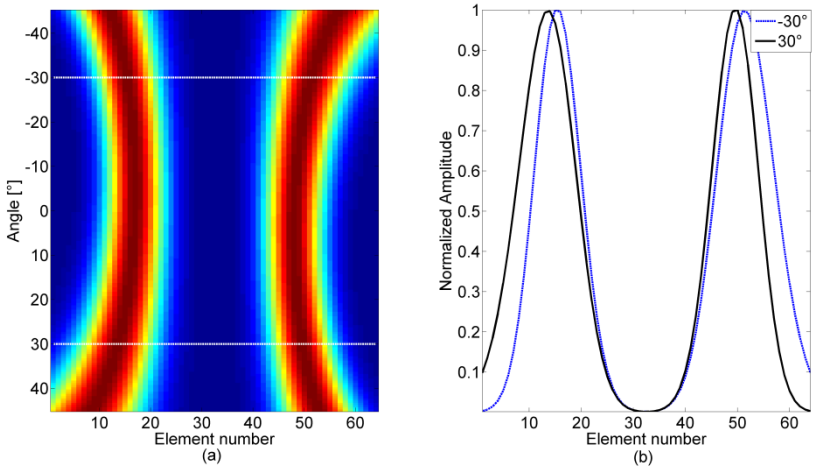

Fig. 5-1: (a) 2D representation of back-proapgation apodization function as a function of angle and element number. (b) Extraction of two profiles at two different angles, 30° and −30°, the parameters are $\lambda_\theta^{PSF} = 8°, \sigma_\theta^{PSF} = 12°, f_0 = 2.1MHz$.

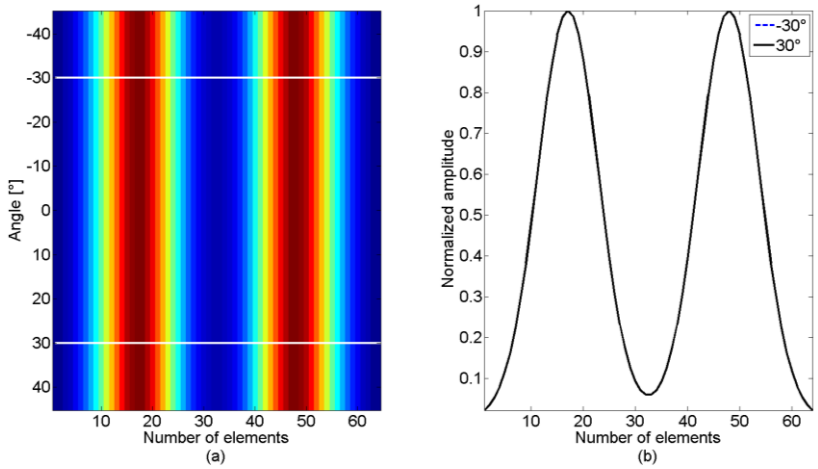

Fig. 5-2: (a) 2D representation of Fourier based apodization function as a function of angle and element number. (b) Extraction of two profiles at two different angles, 30° and −30°, the parameters are $\lambda_\theta^{PSF} = 8°, \sigma_\theta^{PSF} = 12°, f_0 = 2.1MHz$.

5.2.2 PSF quality evaluation

Evaluation Measure

In order to measure the performance of the proposed back-propagation and the conventional Fraunhofer approximation approach, the comparison of PSFs' quality is taken as a measure. The quality of PSF is addressed by comparing the simulated PSF to the expected, theoretical 2D point spread function (PSF^{th}). The simulated PSF is obtained by applying a beamforming/apodization scheme, noted PSF^{real}, which is

acquired by applying either the proposed back-propagation approach or the conventional Fourier-based technique (which is obtained under Fraunhofer approximation). In all simulations, the PSF amplitudes were normalized. The measure used in simulations to quantify the similarity between PSF^{real} and PSF^{th} is the RMSE (Root Mean Square Error). Calling PSF_{ij}^{real} the i,jth value of the discrete 2D PSF obtained through the Fourier transform or back-propagation and PSF_{ij}^{th} the corresponding i,jth value of the theoretical PSF, the RMSE is given as

$$RMSE = \sqrt{\frac{1}{M \times N} \sum_{i=1}^{M} \sum_{j=1}^{N} (PSF_{ij}^{th} - PSF_{ij}^{real})^2} \tag{5.1}$$

where N is the number of points of the simulated discrete PSF.

PSF Accuracy

So as to look at the spatial distribution of RMSE, the accuracy of the PSFs is obtained for depths ranging from 60 to 100 mm and scan angle from −30° to 30° is given in Fig. 5-3. The accuracy is evaluated using RMSE as given in equation (5.1). The comparison of Fig. 5-3(a) and (b) shows that the RMSE associated with the Fourier-based beamforming increases with scan angle whereas the RMSE associated with back-propagation decreases and it is always smaller than the first one. In order to display these observations more accurately, Fig. 5-4 provides a plot of the RMSE profiles obtained at a depth of 80 mm both for Fourier-based and BP-based beamforming. Fig. 5-4 confirms that BP-based beamforming provides a PSF closer to the expected PSF than Fourier-based beamforming, whatever the scan angle, and that this difference is particularly large for lateral scan regions, i.e., for large scan angles, such as the position close to 30°.

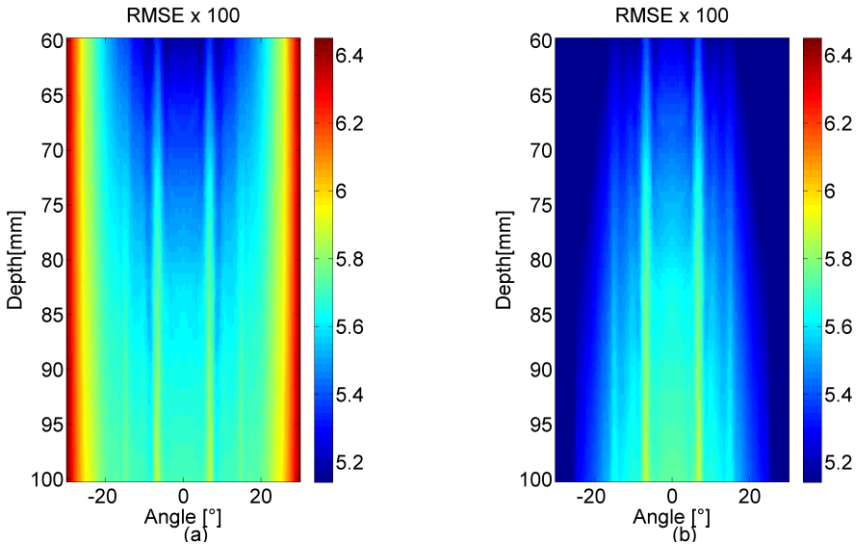

Fig. 5-3: (a) and (b) 2D RMSE images obtained with Fourier transform and back-propagation separately, the parameters are $\lambda_\theta^{PSF}=8°, \sigma_\theta^{PSF}=12°, f_0=2.1MHz$.

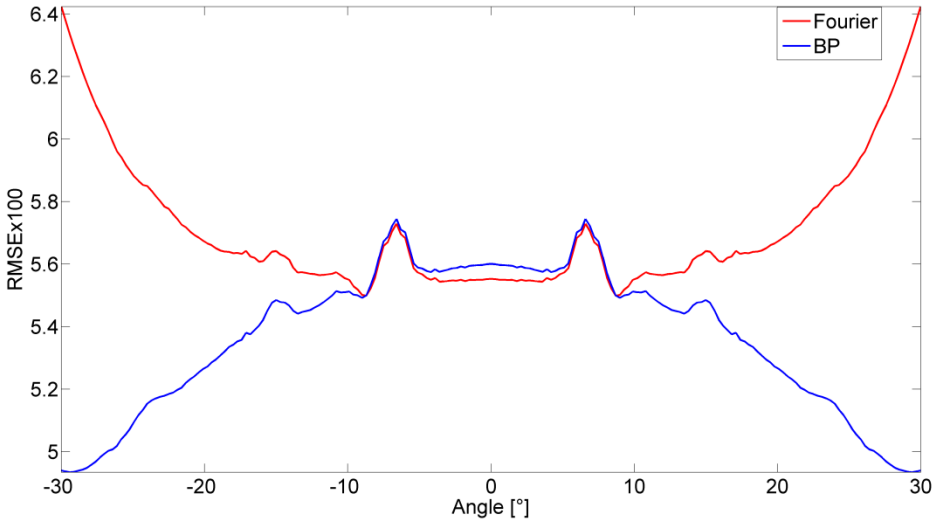

Fig. 5-4: RMSE profiles corresponding to Fig. 5-3 at depth of 80 mm. The RMSE profile associated with back-propagation is plotted in blue, whereas the RMSE profile associated with Fourier is plotted in red.

5.2.3 Parameters influence

In order to show that the improvement obtained with back-propagation compared to FAs is a general result for any TOs PSF parameter, in this section we study the influence of the parameters driving the shape of the TOs, i.e., the lateral wavelength λ_θ^{PSF} and standard deviation σ_θ^{PSF} of the PSF. The range of λ_θ^{PSF} is chosen as from 6° to 12° and the range of σ_θ^{PSF} is chosen as from 6° to 24°.

Fig. 5-5 displays the influence of λ_θ^{PSF} and σ_θ^{PSF} on the accuracy of the PSFs obtained. Fig. 5-5(a, b) shows RMSE for a point located in front of the probe (i.e., $\theta = 0°$) at a depth of 80 mm using Fourier-based and BP-based beamforming, respectively. It can be observed that the two parts of Fig. 5-5(a, b) are very similar. This is consistent with the fact that this situation corresponds to the location where the Fraunhofer approximation and thus the Fourier-based beamforming are the most valid. As a consequence, BP-based beamforming only contributes a slight improvement, mainly for low values of λ_θ^{PSF} and σ_θ^{PSF} (lower left corner of Fig. 5-5(a, b)). Fig. 5-5(c, d) shows RMSE for a point located laterally with respect to the probe ($\theta = 30°$) using Fourier-based and BP-based beamforming, respectively. These figures show that back-propagation clearly improves the PSF located on the side of probe, since the approximation underlying Fourier-based beamforming is less valid in this location. Here again, this improvement is more noticeable for low values of λ_θ^{PSF} and σ_θ^{PSF}, on the lower left-hand part of Fig. 5-5(c, d).

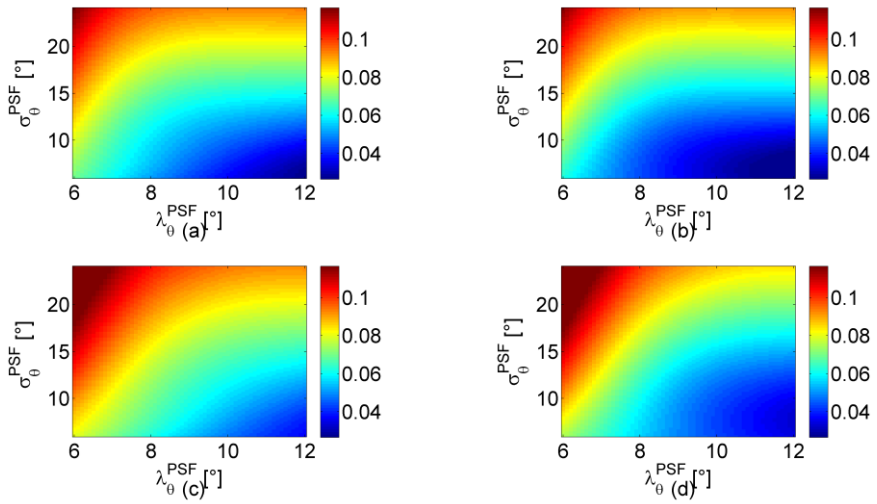

Fig. 5-5: Presentation of RMSE obtained with different λ_θ^{PSF} and σ_θ^{PSF} under Fourier transform in (a) (for a scatterer located in front of the probe) and (c) (for a scatterer located in the direction of 30°) and back-propagation in (b) (for a scatterer located in front of the probe) and (d) (for a scatterer located in the direction of 30°).

In order to clearly show the improvement brought by back-propagation method over Fourier-based beamforming, we also give the difference between the RMSE provided by these 2 methods. This result is given in Fig. 5-6. Fig. 5-6(a) corresponds to the difference obtained in front of the probe (i.e., $\theta = 0°$) at a depth of 80 mm (it thus corresponds to the difference of Fig. 5-5(a) and (b)). Fig. 5-6(b) gives the difference

on the side of the probe ($\theta = 30°$), corresponding to the difference of Fig. 5-5(c) and (d). Overall, the difference is positive which indicates that the error is larger for Fourier-based beamforming than for BP-based beamforming. Moreover, the comparison of Fig. 5-6(a) and Fig. 5-6(b) indicates that the improvement associated to back-propagation is more important for larger angles. This indicates that back-propagation beamforming is better adapted to sectorial geometry than Fourier-based beamforming.

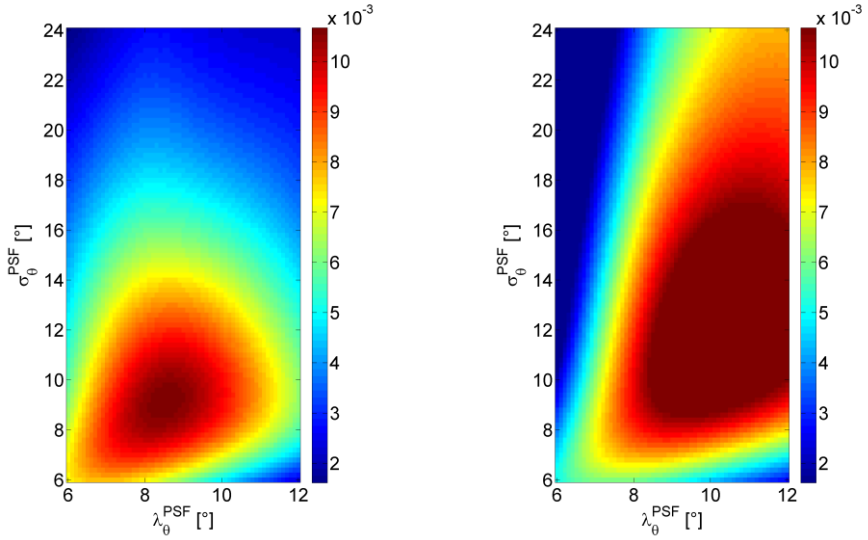

Fig. 5-6: (a) Difference of RMSE obtained with back-propagation and Fourier-based method in front of the probe (i.e., $\theta = 0°$) at a depth of 80 mm, corresponding to the difference Fig. 5-5(a) and (b) above. (b) Difference of RSME obtained with back-propagation and Fourier-based method on the side of probe ($\theta = 30°$), corresponding to the difference of Fig. 5-5(c) and (d).

From these results, it may be inferred that BP-based beamforming should improve the estimation of lateral motion compared to Fourier-based beamforming. The next section investigates this question.

5.2.4 Motion estimation accuracy

Because our method is based on phase differences, it cannot estimate motions larger than half of the axial (0.36mm) or half of the lateral wavelength (4°). The simulated motions are within the range [0°–6.4°] in the transverse direction and [0–0.6] mm in the axial direction (i.e., along the beam axis). The maximum values are thus larger than half the lateral and axial wavelength, allowing assessing the limits of the technique.

On a more general level, it should however be noted that estimating larger motion can nevertheless be easily performed using 2 different strategies:

- The large scale component of the motion can be estimated in a first step using e.g. block matching techniques and our method can be then used to refine the estimates [60]
- The rapidly developing ultrafast acquisition techniques will considerably decrease the magnitude of the motion to be estimated, making the proposed method directly applicable (thus making the above mentioned pre-processing step unnecessary)

Motion estimation for given displacements

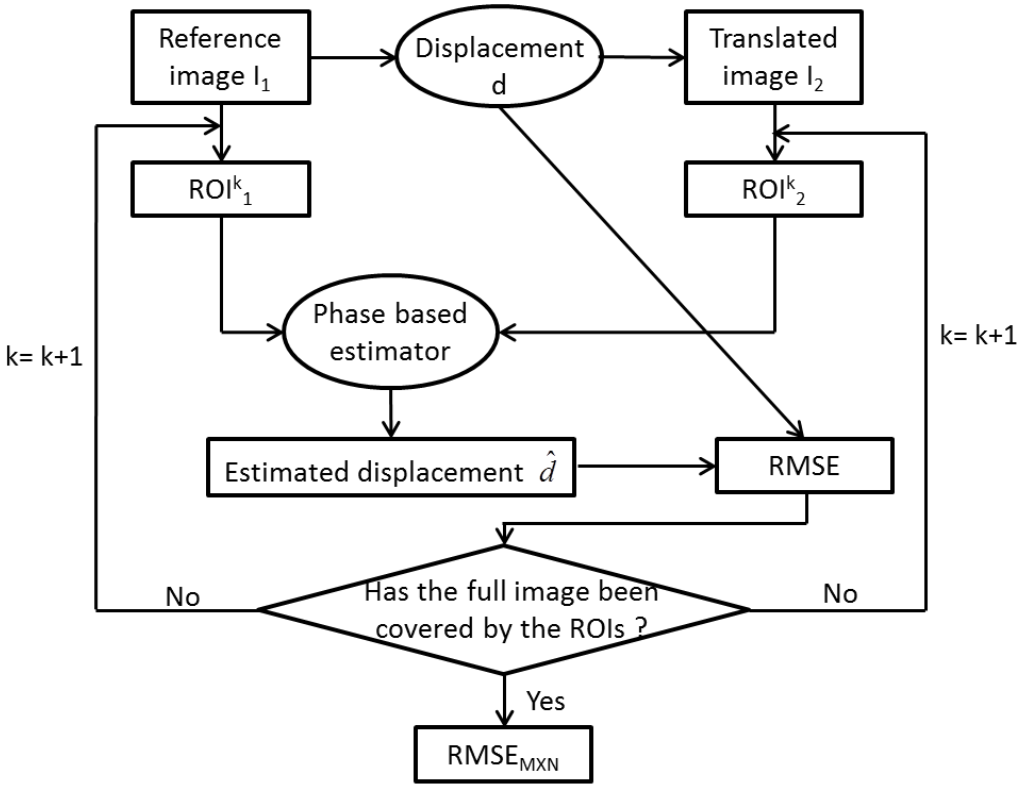

Fig. 5-7: Schematic diagram of the motion estimation procedure

In order for a clearly understanding of motion estimation measure, the Fig. 5-7 presents a schematic diagram procedure:

1. Obtain the translated image I_2 from the reference image I_1 by displacing the scatterers by d;
2. Consider a region of interest ROI_1^k in I_1, and ROI_2^k in I_2,;
3. Extract the phase of two ROIs and calculate the estimated displacement $\hat{d}$ using the phase based estimator [29];
4. Calculate the RMSE of the estimated $\hat{d}$ to the theoretical displacement d ;

5. Take the ROI in another position repeat the step 2 to step 4 until the ROIs have covered all the images I_1 and/or I_2.

The principle of this local phase-based method is to create complex image blocks based on a 2D extension of the analytical signal [61]. Basically, such an image block is generated by keeping only one quadrant of its two dimensional Fourier spectrum. Two different analytical images are obtained by keeping two different quadrants of the 2D FFT spectrum. A 2D rigid translation vector is then deduced from the phases of two successive TOs images. For more details on this motion estimation technique, the reader can refer to [29, 62].

The applied motions are purely axial, purely transversal, or diagonal. These motions are applied to 100 different isotropic phantoms, each of them containing 10,000 scatterers located in front of the probe. The phantom covers a depth ranging from 60 to 100 mm.

In these experiments, the motion is estimated between 2 full image acquisitions, the results are obtained by performing 100 motion estimations by varying the scatterers random distributions at the same position, then computing the average of these estimates. This method was used in the following conditions:

a) For a given phantom, we apply eight motions in the transverse, axial and diagonal directions, resulting in a total of 24 motions.
b) For a given motion, we chose a region of interest (ROI) with a size equal to half of the lateral and axial wavelength and centered on the initial and displaced position of the phantom.
c) The motion is then estimated using the phase-based method of [29] applied in these ROI.

For a given motion, the above procedure is applied to 100 different phantoms obtained by varying the diffusers random distributions. The results are then presented as the mean value and standard deviation of the motion estimates at a depth of 80 mm for varying direction ranging from -30° to 30° relative to the probe central axis. They are presented in Fig. 5-14, Fig. 5-15 and Fig. 5-16.

Fig. 5-8, Fig. 5-9 and Fig. 5-10 give the results of motion estimation performed at points located in front ($\theta = 0°$) and on the side ($\theta = 30°$) of the probe for Fig. 5-11, Fig. 5-12 and Fig. 5-13. In both cases, the depth was 80 mm.

The results located on a vertical axis of Fig. 5-9 shows that Fourier-based and BP-based beamforming yield similar motion estimation accuracy for purely axial motion. On the other hand, the results corresponding to pure transverse motion in

Fig. 5-8 (points located close to an horizontal axis) indicate that BP-based beamforming yields an improvement over Fourier-based beamforming for lateral motion estimation. The results in Fig. 5-10 associated with the combined motion (points located on the diagonal of the plot) show an intermediate situation where back-propagation performs better than Fourier, although this improvement is not as great as for the purely transverse motion. It may also be observed that accuracy decreases as motion amplitude increases, especially when the displacements are larger than half the signal wavelength, there are significant differences between the estimated and real motions.

The results obtained on the side of the probe (Fig. 5-12) are similar to the previous results for axial motion in Fig. 5-9: BP-based beamforming improved a little in terms of motion accuracy as compared to Fourier-based beamforming. Regarding the transverse motion in Fig. 5-11, BP-based beamforming still improves accuracy, but not as much as in

Fig. 5-8. Here again, the results associated with diagonal motion correspond to an intermediate situation where back-propagation performs better than Fourier in Fig. 5-13. In line with the conclusion from

Fig. 5-8, Fig. 5-9 and Fig. 5-10, the estimated motion deviates a lot when the real displacement is larger than half the signal wavelength (8° for full of lateral wavelength and 0.73mm for full of axial wavelength), thus given the limitation of our method is the half of signal wavelength.

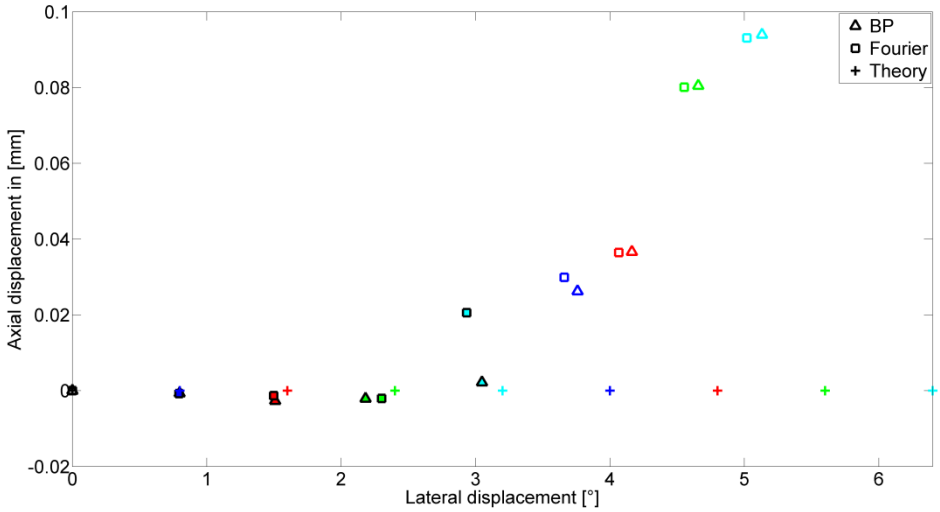

Fig. 5-8: Estimation of lateral displacements. The motion was estimated using either Fourier-based (square) or BP-based (triangle) beamformed images and the results are compared to the true motion (crosses). Motion estimation was performed at points located in front ($\theta = 0°$) of the probe at the depth of 80 mm. The half value of lateral wavelength is 4°.

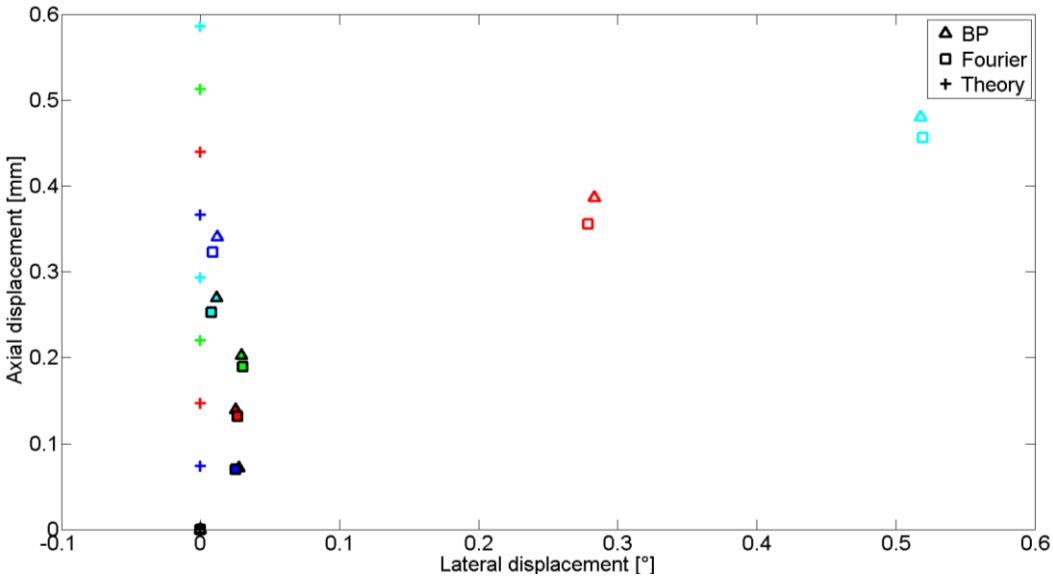

Fig. 5-9: Estimation of axial displacements. The motion was estimated using either Fourier-based (square) or BP-based (triangle) beamformed images and the results are compared to the true motion (crosses). Motion estimation was performed at points located in front ($\theta = 0°$) of the probe at the depth of 80 mm. The half value of axial wavelength is 0.36 mm.

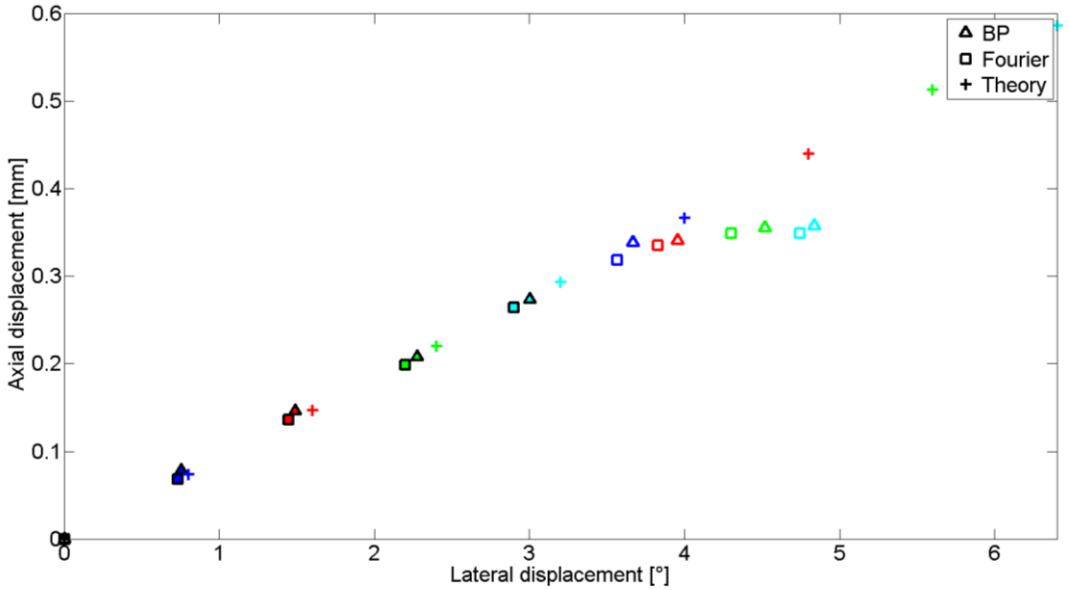

Fig. 5-10: Estimation of diagonal displacements. The motion was estimated using either Fourier-based (square) or BP-based (triangle) beamformed images and the results are compared to the true motion (crosses). Motion estimation was performed at points located in front ($\theta = 0°$) of the probe at the depth of 80 mm. The half value of lateral wavelength is 4° and 0.36 mm for the half of axial wavelength.

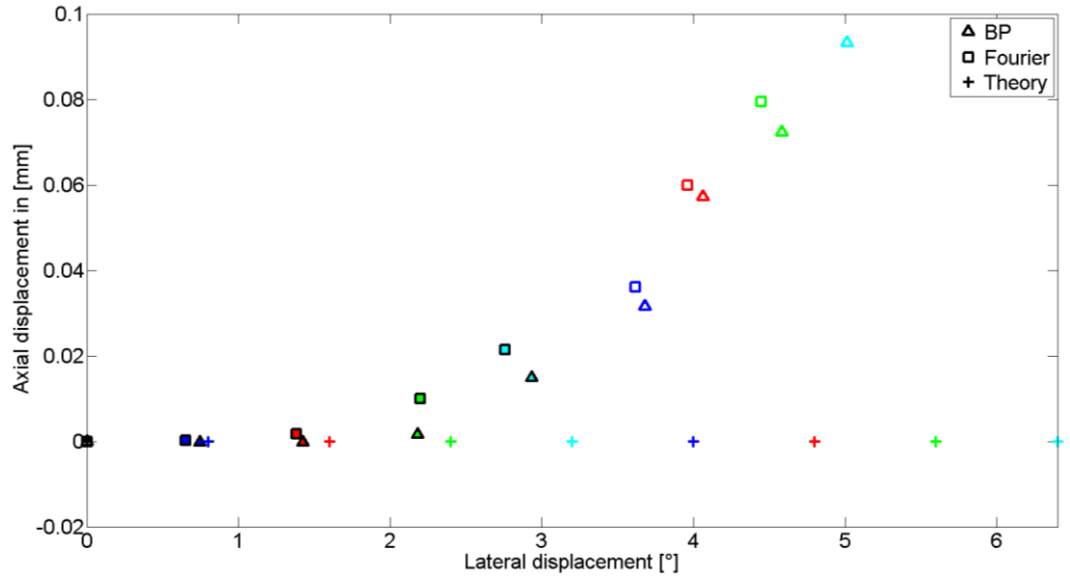

Fig. 5-11: Estimation of lateral displacements. The motion was estimated using either Fourier-based (square) or BP-based (triangle) beamformed images and the results are compared to the true motion (crosses). Motion estimation was performed at points located on the side ($\theta = 30°$) of the probe at the depth of 80 mm. The half value of lateral wavelength is 4°.

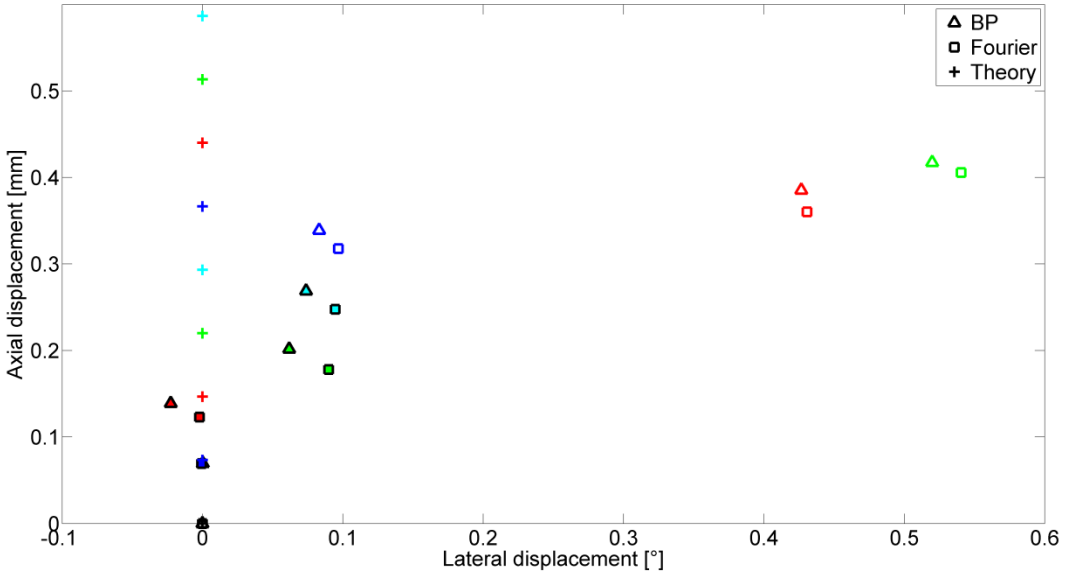

Fig. 5-12: Estimation of axial displacements. The motion was estimated using either Fourier-based (square) or BP-based (triangle) beamformed images and the results are compared to the true motion (crosses). Motion estimation was performed at points located on the side ($\theta = 30°$) of the probe at the depth of 80 mm. The half value of axial wavelength is 0.36 mm.

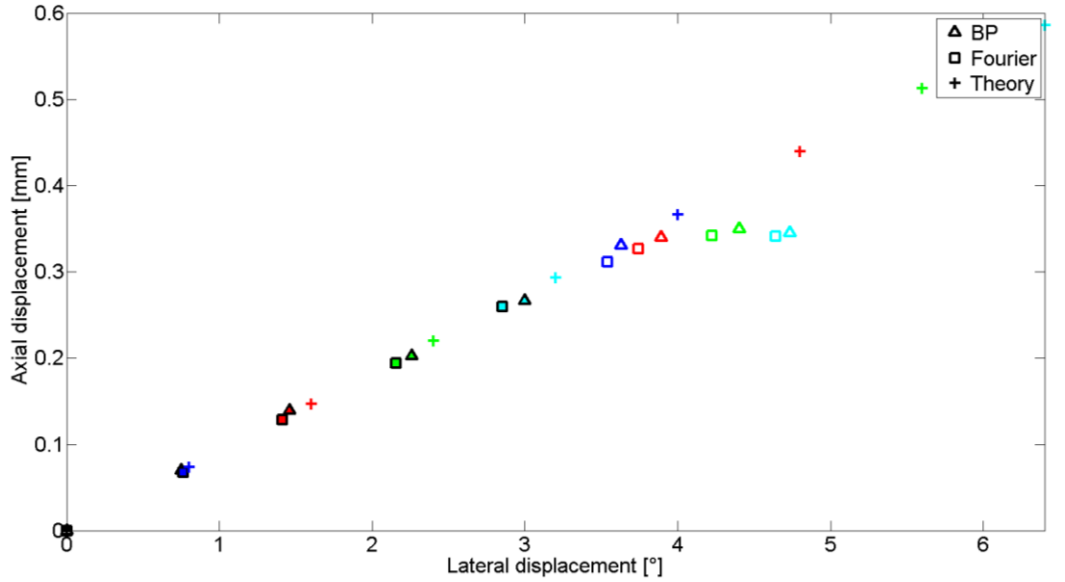

Fig. 5-13: Estimation of diagonal displacements. The motion was estimated using either Fourier-based (square) or BP-based (triangle) beamformed images and the results are compared to the true motion (crosses). Motion estimation was performed at points located on the side ($\theta = 30°$) of the probe at the depth of 80 mm. The half value of lateral wavelength is 4° and 0.36 mm for the half of axial wavelength.

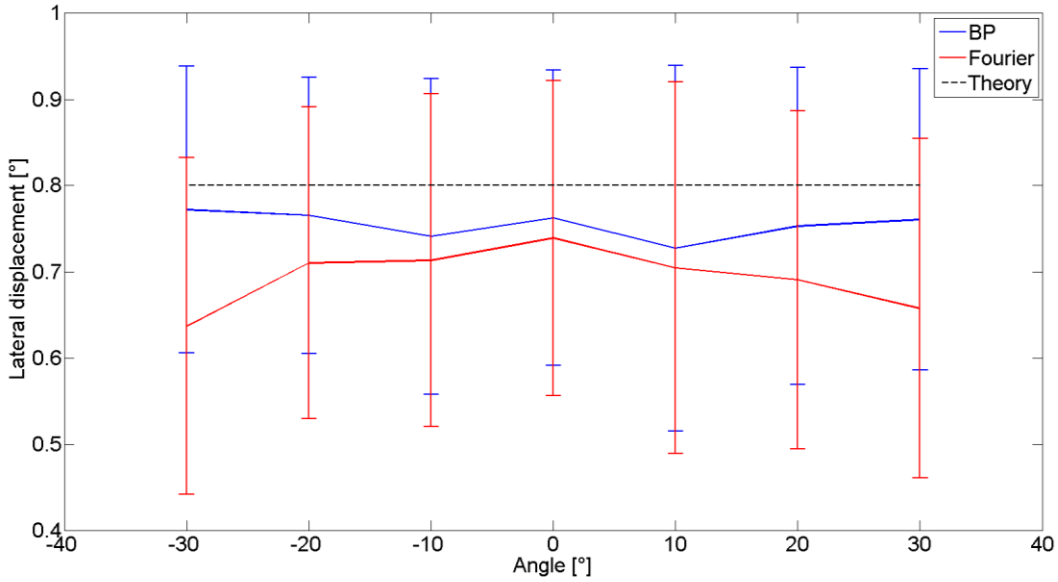

Fig. 5-14: Presentations of the mean value and standard deviation of the motion estimates in the case of a pure lateral motion of 0.8° at a depth of 80mm from -30° to 30. The blue solid line corresponds to BP method, the red solid line corresponds to Fourier method, and the black dashed line demonstrates the theory mean value.

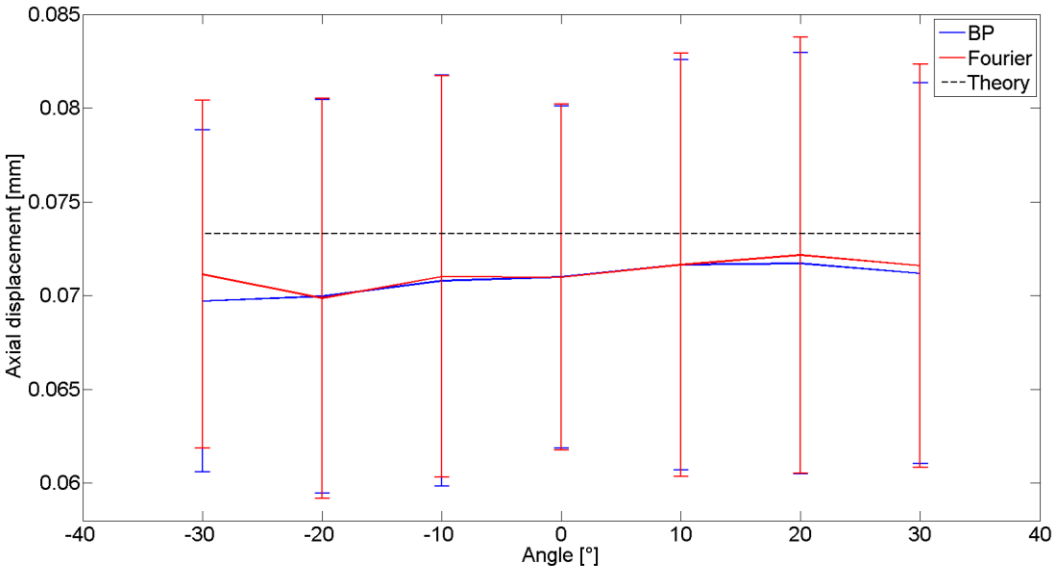

Fig. 5-15: Presentations of the mean value and standard deviation of the motion estimates in the case of a pure axial motion of 0.07 mm at a depth of 80mm from -30° to 30 The blue solid line corresponds to BP method, the red solid line corresponds to Fourier method, and the black dashed line demonstrates the theory mean value.

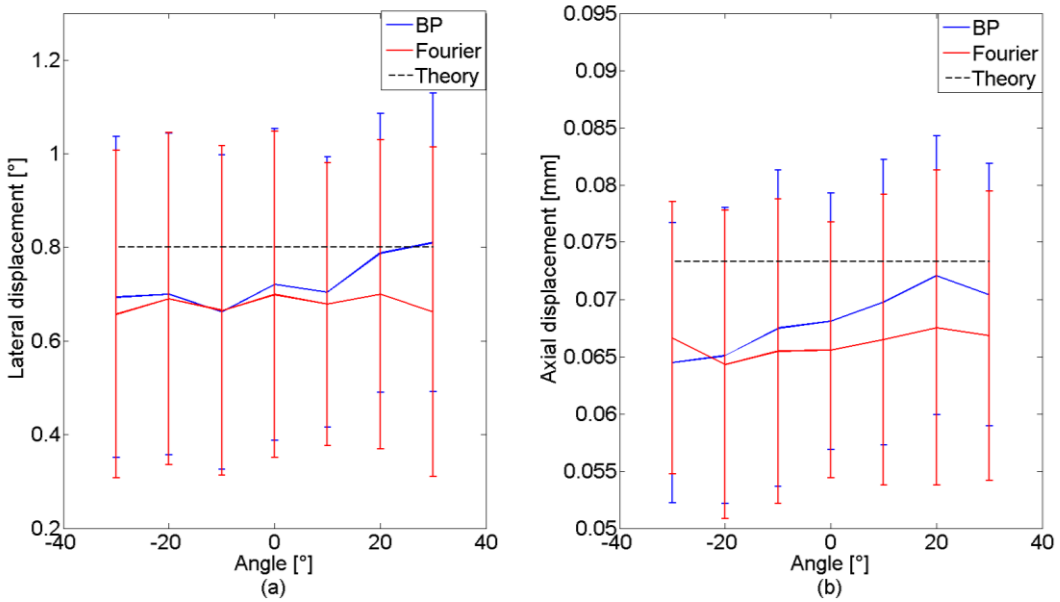

Fig. 5-16: Presentations of the mean value and standard deviation of the motion estimates in the case of a diagonal motion (0.8° in lateral direction and 0.07mm in axial direction) at a depth of 80mm from -30° to 30 (a) shows the lateral motion estimates and (b) presents the axial motion estimates. The blue solid line corresponds to BP method, the red solid line corresponds to Fourier method, and the black dashed line demonstrates the theory mean value.

Fig. 5-14, Fig. 5-15 and Fig. 5-16 show the mean value and standard deviation of the motion estimates at a depth of 80mm for varying directions ranging from -30° to 30° relative to the probe central axis. Fig. 5-14 is given for the estimation of a pure lateral motion of 0.8° using Fourier relation in red solid line and BP-based beamformer in blue solid line respectively. It shows that the mean value of back-propagation method is much closer to the reference (black dashed line) and can provide smaller standard deviation than Fourier-based beamforming. Note that the better value of RMSE observed for BP mainly comes from the smaller mean error associated to BP. Indeed the standard deviation found for both methods are very close. On the other hand, Fourier and BP-based beamforming provide very close mean value and standard deviation for pure axial motion of 0.07mm as presented in Fig. 5-15. Fig. 5-16 gives the result for diagonal motion (0.8° in lateral direction and 0.07mm in axial direction), and yields the same conclusions as in Fig. 5-14 for the lateral component estimation and Fig. 5-15for the axial component estimation.

Let us note that the estimation bias could be compensated for by scaling of the estimates based on the actual mean spatial frequency of the PSF. One option could be to estimate the mean spatial frequency, to be able to compensate its variation. In this work, we propose another option, which consists in performing the compensation during the beamforming step.

Overall, it may be concluded that motion estimation performed on BP-based beamformed TOs images always yields better accuracy as compared to Fourier-based beamformed TOs images. The only exception to this corresponds to the axial motion applied in front of the probe, where back-propagation and Fourier perform in a similar way.

Spatial distribution of motion estimation error

The spatial distribution of the motion estimation error, measured as RMSE between estimated and real motion is plotted for a sectorial scanning region corresponding to a depth ranging from 70 to 90 mm and an angle ranging from −30° to 30° (Fig. 5-17, Fig. 5-18 and Fig. 5-19).

Fig. 5-17, Fig. 5-18 and Fig. 5-19 illustrate the spatial distribution of the motion estimation error for three types of motion: a transverse motion with magnitude 0.8°, an axial motion with magnitude 0.07 mm and a combined motion with the same magnitudes as above. For each point in the phantom, the accuracy is quantified as the root mean square of the magnitude of the error vector over the 100 experiments (RMSE).

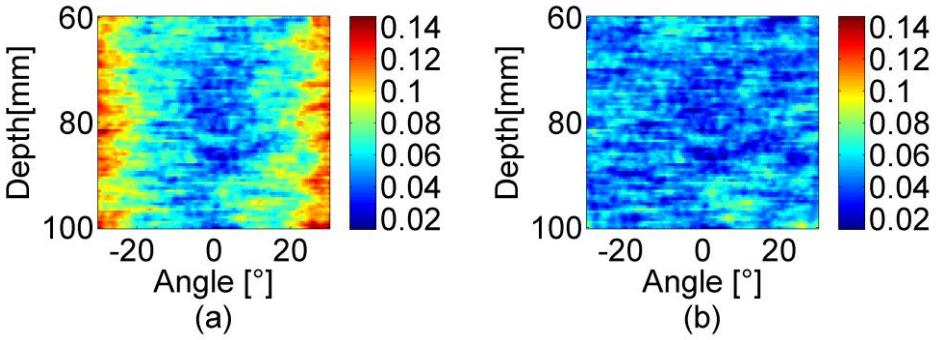

Fig. 5-17: Presentation of estimated accuracy evaluated by RMSE for lateral motion estimation of 0.8° obtained for scatters located from the depth of 60mm to 100mm over the scanning sector from -30° to +30°, using Fourier-based beamformed images in (a) and back-propagation in (b), the RMSE is presented by [°].

Fig. 5-17 displays the results obtained in the case of transverse motion of 0.8°. Fig. 5-17(a) shows that the RMSE associated with Fourier-based beamforming is relatively stable along the propagation direction and increases with the scanning angle to reach a maximum in the lateral regions of the sector. On the other hand, the RMSE associated with back-propagation is fairly stable. Moreover, it is smaller than the RMSE obtained for Fourier-based beamforming, except around the direction corresponding to the probe axis ($\theta = 0°$) where the two RMSEs are close. The mean value of the RMSE associated with Fourier-based beamforming is 0.07°, and it is 0.05°

for back-propagation. These results show that back-propagation contributes on average a 32.8% improvement over Fourier-based beamforming.

Fig. 5-18 displays the results obtained in the case of axial motion of 0.07mm. In contrast to the results obtained for transverse motion, it can be observed that the two beamforming methods yield very close RMSEs. The mean RMSE values are 9.4×10^{-3} mm and 9.3×10^{-3} mm for Fourier-based beamforming and back-propagation, respectively.

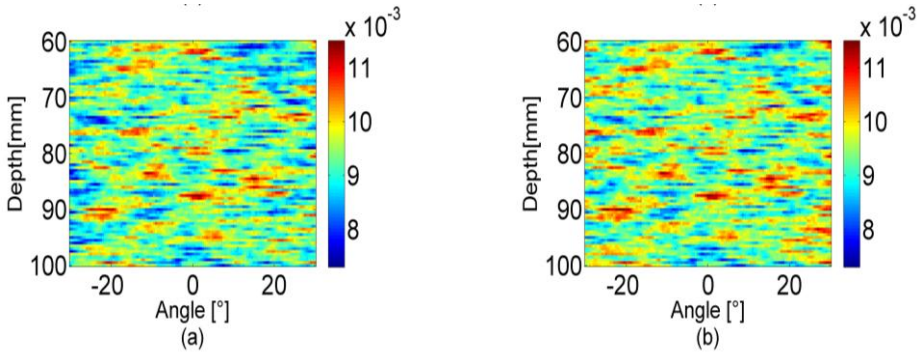

Fig. 5-18: Presentation of estimated accuracy evaluated by RMSE for axial motion estimation of 0.07mm obtained for scatters located from the depth of 60mm to 100mm over the scanning sector from -30° to +30°, using Fourier-based beamformed images in (a) and back-propagation in (b), the RMSE is presented by [mm]

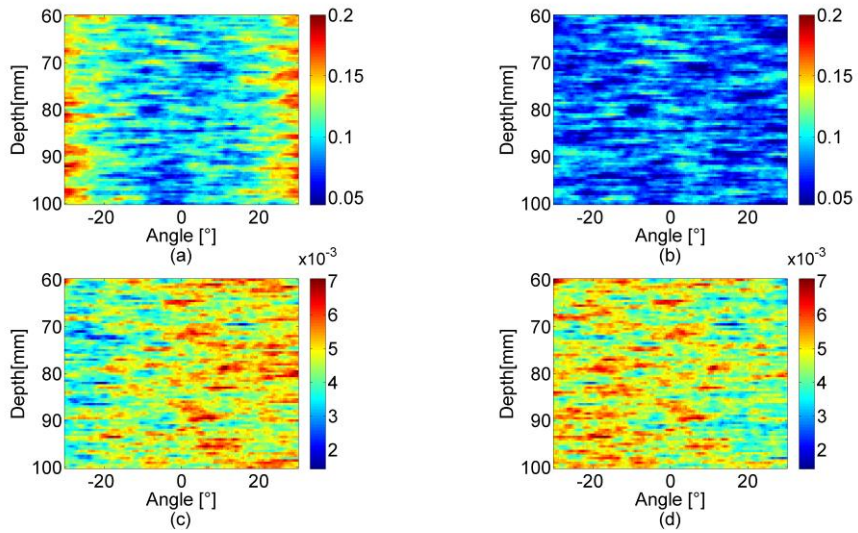

Fig. 5-19: Presentation of estimated accuracy evaluated by RMSE for diagonal motion estimation (0.8° in lateral direction and 0.07mm in axial direction) for scatters located from the depth of 60mm to 100mm over the scanning sector from -30° to +30°: (a) and (b) show the magnitude in [°] of the transverse RMSE using Fourier-based beamformed images and back-propagation, respectively; (c) and (d) show the magnitude in [mm] of the axial RMSE using Fourier-based beamformed images and back-propagation, respectively.

Fig. 5-19 displays the results obtained in the case of a diagonal motion. Fig. 5-19 (a, b) shows the magnitude of the transverse RMSE using Fourier-based beamformed images and back-propagation, respectively. Fig. 5-19(c, d) shows the corresponding axial RMSE. These results yield the same conclusions as in Fig. 5-17and Fig. 5-18. Indeed, Fig. 5-19(a, b) shows that the transverse RMSE associated with Fourier-based beamforming increases with the scanning angle, whereas the RMSE associated with back-propagation is more stable and smaller. Concerning the axial RMSE, Fig. 5-19(c, d) indicates that both methods yield very close accuracy values. The mean transverse RMSEs are 0.11° and 0.08° for Fourier-based beamforming and back-propagation, respectively; thus back-propagation contributes an average improvement of 28% over Fourier-based beamforming.

In order to see if the differences are statistically significant, Table 2 presents the t-test for the estimated results which are obtained at the center and on the side of image. In this table, the value 1 indicates a rejection of the null hypothesis at the 5% significance level, which means they have significant difference, and on the contrary the value 0 indicates a failure to reject the null hypothesis. From Table 2, we may observe that there is no significant difference concerning the estimates of the axial motion component. The situation for the transverse component is the following:

- In the center of the image there is no significant difference
- On the contrary on the sides of the image the difference is significant

Table 2: T-TEST RESULT OF ESTIMATED MOTION ACCURACY

Motion direction	Lateral movement (0.8°)		Axial movement (0.07mm)		Diagonal movement			
					Lateral direction (0.8°)		Axial direction (0.07mm)	
ROI position	Center (0°,80 mm)	Side (30°,80 mm)	Center (0°,80 mm)	Side (30°,80 mm)	Center (0°,80 mm)	Side (30°,80 mm)	Center (0°,80 mm)	Side (30°,80 mm)
h	0	1	0	0	0	1	0	0

These findings clearly show that back-propagation beamforming improves the accuracy for the transverse motion estimates on the sides of the image.

5.3 Simulated cardiac motion

Further comparison of the performance in terms of beamforming is disposed to a realistic cardiac motion. The cardiac motion is created by taking a real cardiac ultrasound acquisition as template, and mimics it both visually and synthetically. The resulting simulations look virtually indistinguishable from real acquisitions. As the simulated sequences embed a known motion, they can be used as a benchmark to evaluate algorithms for the estimation of heart motion.

The simulation is performed as described in [63] and leads to a complete cardiac cycle composed of 46 consecutive frames. Note that the simulated cardiac sequences span one cardiac cycle from one end-systole to the successive one.

Fig. 5-20 and Fig. 5-21 present the displacement errors in degree for lateral estimation and in [mm] for axial estimation. The blue plot corresponds to BP-based beamformer, and the black plot to the Fourier-based beamformer. Fig. 5-20 illustrates the mean error values for each frame of the synthetic sequence for the lateral error (a) and the axial error (b). It may be observed that BP-based beamformer provides lower lateral error than that of Fourier whereas the two methods give the same results for the axial error. Fig. 5-21 reports the corresponding standard deviations. It shows that BP-based beamformer present lower standard deviation for both lateral and axial errors.

In Fig. 5-20 and Fig. 5-21, frames 10 to 18 correspond to diastolic expansion, frames 19 to 31 to end-diastole while frames 32 to 45 to systolic contraction. As an example the estimation results during systolic contraction and diastolic expansion on the short axis sequence are reported in Fig. 5-22 . These results show that the estimated displacements are qualitatively consistent with the physiological motion expected on a healthy heart in those two phases of the cardiac cycle.

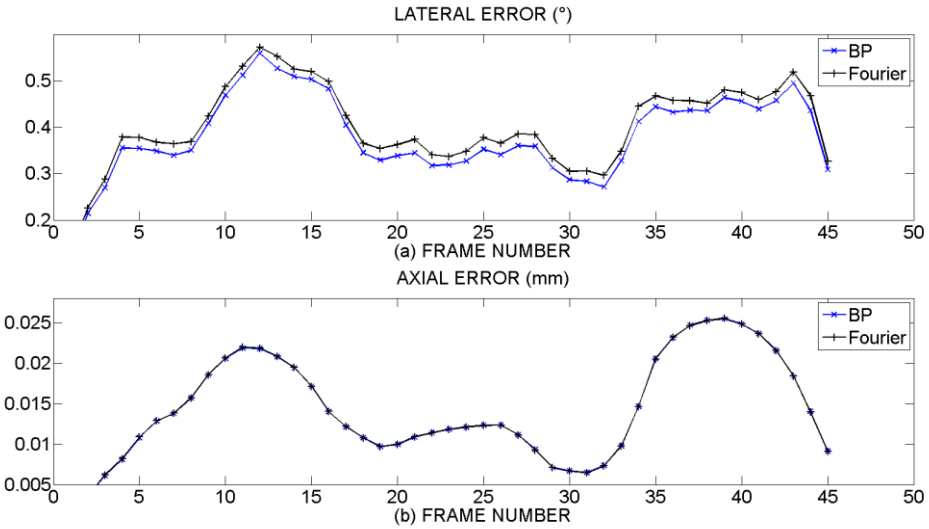

Fig. 5-20: Displacement errors on pre-scan converted data for the short-axis sequence. (a) and (b) illustrate the mean values for each frame of the synthetic sequence for the lateral error in degree and the axial error in [mm] respectively. The blue cross line is acquired under BP-based beamformer, and the black plus sign line the Fourier-based beamformer.

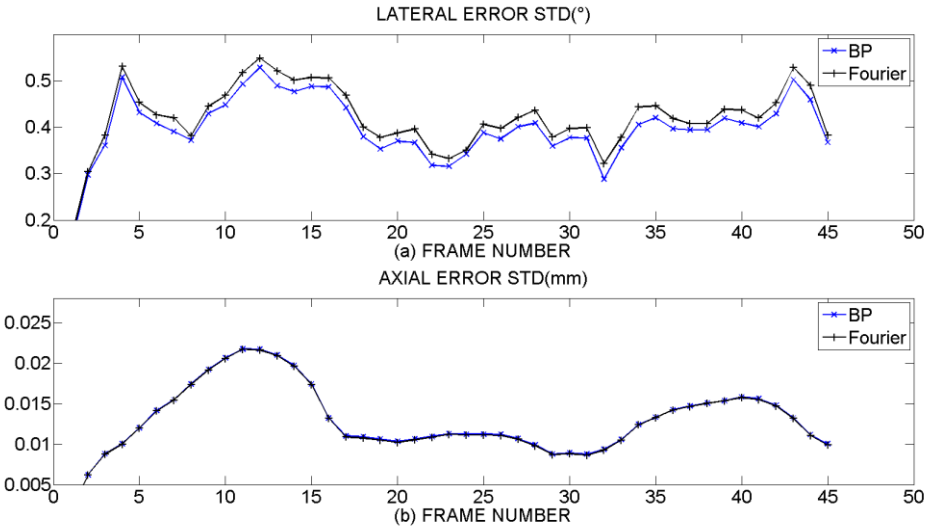

Fig. 5-21: Presentation of the corresponding standard deviations to Fig. 5-20. (a) and (b) demonstrate the standard deviation for each frame of the synthetic sequence for the lateral error in degree and the axial error in [mm] respectively. The blue cross line is acquired under BP-based beamformer, and the black plus sign line the Fourier-based beamformer.

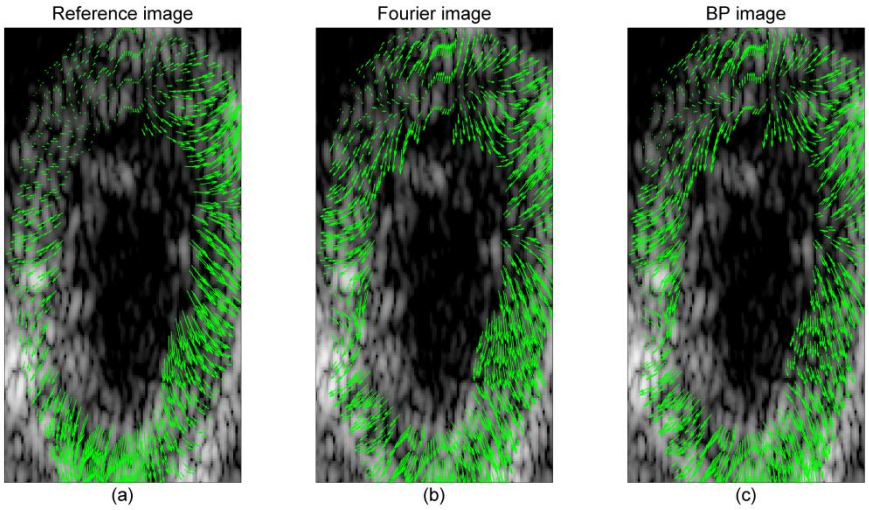

Fig. 5-22: Example of estimated motion fields on one diastolic frame of the short axis sequence, (a) presents the reference motion, (b) and (c) for the motion estimated using Fourier and back-propagation beamformer design.

5.4 Experimental results

In order evaluate the method on real data, we have performed a simple experimental study. It consisted in acquiring data from a wire to evaluate the experimental PSF. BP-based TO-beamforming method was compared to the Fourier-based technique. The experiments were conducted by using the ultrasound acquisition equipment named ULA-OP [64, 65], in which we have imported the proposed apodization. The wire was imaged with 0° and 30°, where θ is the scanning angle relative to the probe axis. The parameter settings correspond to those given in Table 1. This was repeated 100 times, measuring the RMSE in the same way as in the simulations.

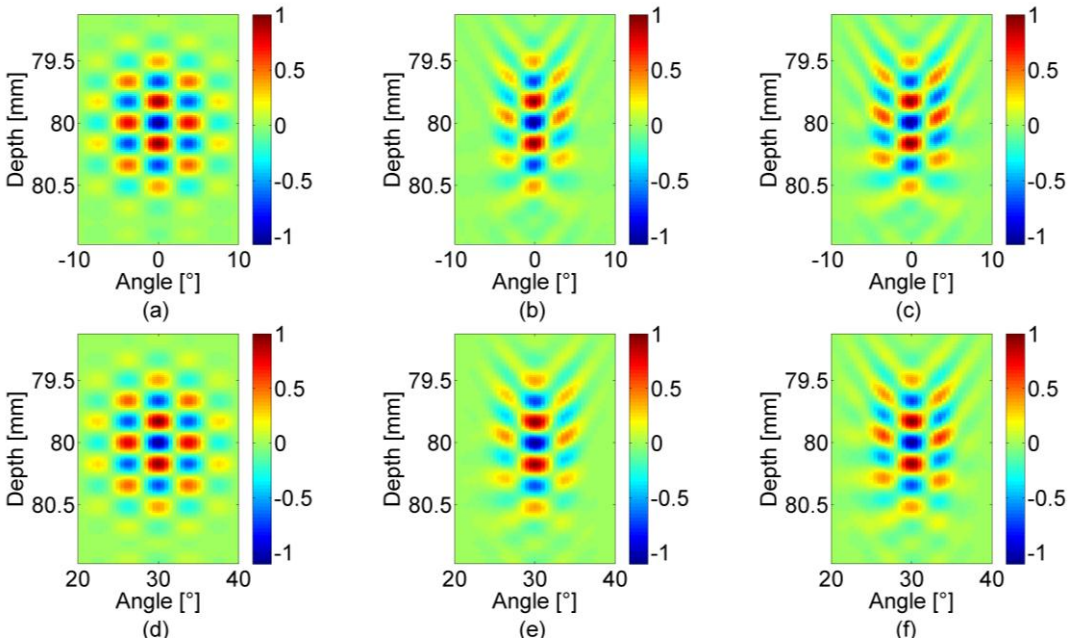

Fig. 5-23: Presentation of the theoretical PSF in front (0°) of the probe in (a) and the corresponding experimented PSF obtained under the Fourier relation in (b) and back-propagation in (c); (d) is the theoretical PSF on the side (30°) of the probe and the corresponding simulated PSF obtained under the Fourier relation in (e) and back-propagation in (f).

Fig. 5-23 (a, d) presents theoretical PSFs for scatterers located in front (0°) in (a) and on the side (30°) in (d) of the probe. Both scatterers are located at the depth of 80 mm, as in the simulation results for motion estimation from

Fig. 5-8 to Fig. 5-13.

Fig. 5-23 (b, c) shows the PSF obtained in front of the probe using Fourier-based beamforming and BP-based beamforming, respectively. The associated RMSEs are 0.0734 for Fourier-based beamforming and 0.0783 for BP-based beamforming, respectively: they thus yield very close results. Fig. 5-23 (e, f) corresponds to a RMSE of 0.0727 for Fourier transform and 0.0675 for back-propagation, showing that BP-based beamforming improves 7.15% over Fourier-based beamforming. Fig. 5-23(e, f) shows in particular that this improvement mainly corresponds to the side lobes of the PSF, which are better defined in the case of BP-based beamforming.

The PSF obtained in a real experimental setting confirms that the proposed back-propagation beamformer design is technically feasible. The results further validate that BP-based beamforming yields a more accurate PSF than Fourier-based beamforming on the side of the probe. These first results will be confirmed in future more in deep experimental studies including motion accuracy assessments.

Phase based motion estimation techniques are extremely precise but limited to "small" displacements. On the other hand in conventional imaging strategies inter-frame displacements of several millimeters can occur and the unique use of phase based techniques would fail in estimating such important displacements. As a result, as we already proposed in other papers, phase based techniques should be used in combination with a first step estimating large-scale motion, done for example with block matching, or fast acquisition techniques should be used to maintain the inter-frame displacement in an acceptable range.

5.5 Conclusions

In this chapter, we focused on a beamformer designed to improve the formation of PSF with transverse oscillations in the specific case of sectorial geometry, in order to provide better motion estimation. We proposed a beamforming method based on back-propagation and compared it with the classical Fourier-based beamforming method. As presented above, the proposed BP-based beamforming has advantages over Fourier-based beamforming, both for PSF accuracy and motion estimation. The experimental results confirmed the possibility to implement the back-propagation method on a real scanner.

As the proposed back-propagation is only working for one profile whereas the PSF is 2D, the improved back-propagation method associated with a plane wave decomposition principle is introduced in the next chapter 6, these methods are better taking into account the 2D property of the PSF hence can provide higher quality of PSF.

Chapter 6

Plane wave decomposition

Contents

As an extension of the proposed back-propagation method, this chapter describes a plane wave decomposition method and a different back-propagation principle which was initially proposed in [20, 21] for Doppler imaging using transverse oscillations in linear geometry. Doppler imaging implies several transmissions in the same direction in order to estimate the motion vector along that direction (up to 32 transmission [66]). However, it has never been studied for sector geometry. Different from Doppler imaging, in order to estimate a motion or velocity map in echocardiography one needs to sweep a complete image at instant t_0 and another at an instant $t_0 + \Delta t$. So in this chapter, the main concentration will be adapting the plane wave decomposition method and the different back-propagation principle to the sectorial scanning.

The plane wave decomposition theory is used to decompose in different directions an acoustic field into a set of plane waves. This could be done both numerically and analytically. The plane waves are individual waves propagating in different directions. By back-propagating the plane waves corresponding to the expected field from a position in the medium to the probe and after summing up all the back-propagated signals, we get one signal for each transducer. Using these signals as transmitted signals, we are supposed to obtain a transmitted field which is equal to the decomposed one at the initial field position. Need to be pointed out that the pressured field or saying the PSF should be symmetric to the propagation axis [67, 68]. All of these methods would be presented in this chapter.

As just mentioned, the plane wave decomposition method and back-propagation principle were initially proposed in linear geometry for Doppler imaging and estimation of blood velocity. In this chapter, the contribution that is described consists in adapting it to the sectorial geometry.

6.1 Theory

6.1.1 Plane wave decomposition theory in linear geometry

In order to decompose a field into a set of plane waves it is necessary to project the field onto a set of steered or oriented directions. This must be done for all time instances and directions. For doing this, the decomposed field is firstly frozen at time t_0 .Since the frozen field has an oscillatory nature in the propagation direction, the decomposition along the propagation direction can be regarded as time revolution. Each projection corresponding to an angle θ and a time instance $t_0 \pm \tau$ is performed by calculating the integral of the field along a line crossing the field with the right angle θ and the right time $t_0 \pm \tau$, θ is the angle between the integral line and x-axis.

Refering to the Fig. 6-1, it presents an example which the decomposition angle is $\theta = 0°$; and Fig. 6-2 shows the decomposition at direction of θ-angle to the x-axis.

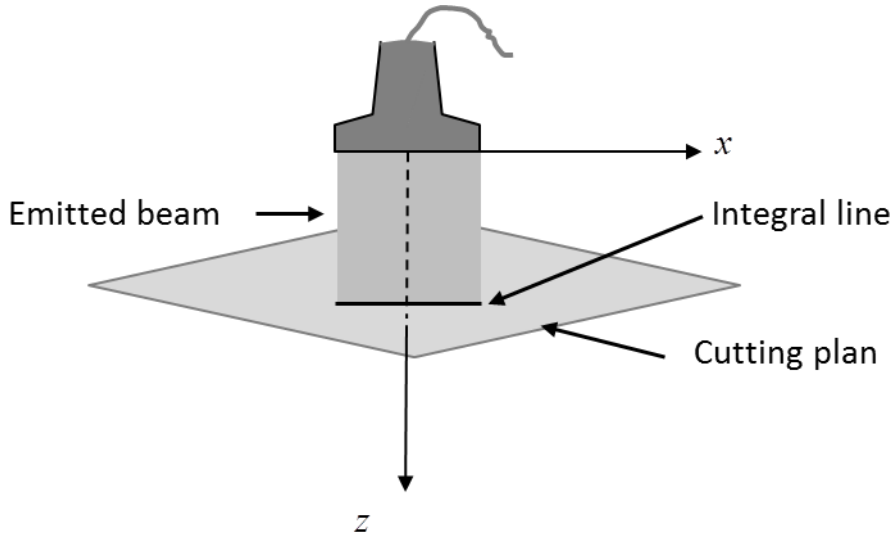

Fig. 6-1: Presentation of the integral line which is the interesting line between a cutting plan with the emitted beam. The cutting plan is parallel to the x-axis.

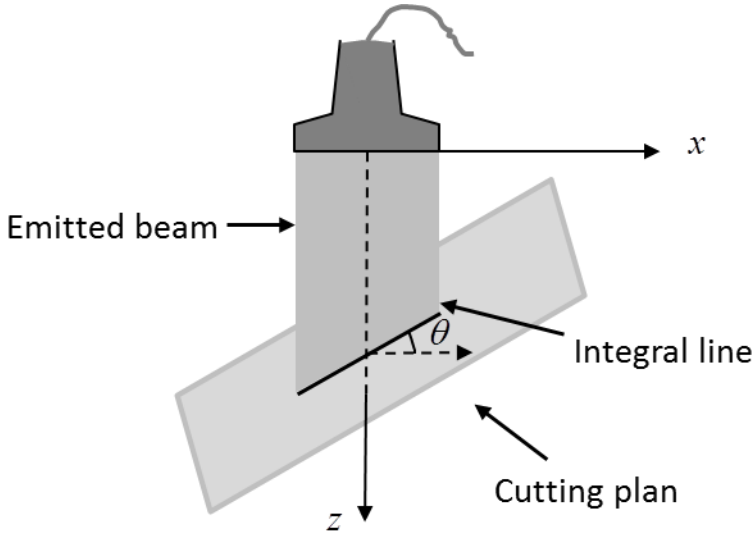

Fig. 6-2: Presentation of the integral line which is the interesting line between a cutting plan with the emitted beam. The cutting plan has a θ-angle to the x-axis.

Fig. 6-3 and Fig. 6-4 present respectively two cases for plane wave decomposition: one is the classic PSF Fig. 6-3 (a) which is a conventional Gaussian envelop both in lateral and axial direction. The corresponding plane wave decomposition is presented in Fig. 6-3 (b); the other is the PSF with transverse oscillations in Fig. 6-4 (a), the plane wave decomposition is presented in Fig. 6-4 (b).

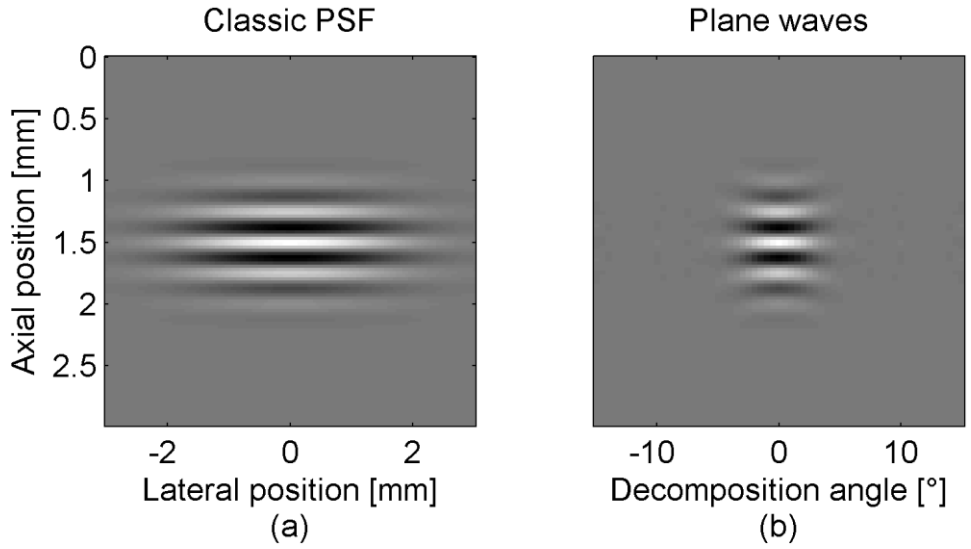

Fig. 6-3: Presentation of classical PSF with Gaussian envelop in (a) and the decomposed plane waves in (b). The center frequency $f_0 = 6MHz$, the lateral wavelength is 3mm, and the decomposition angle varies from -15° to 15°.

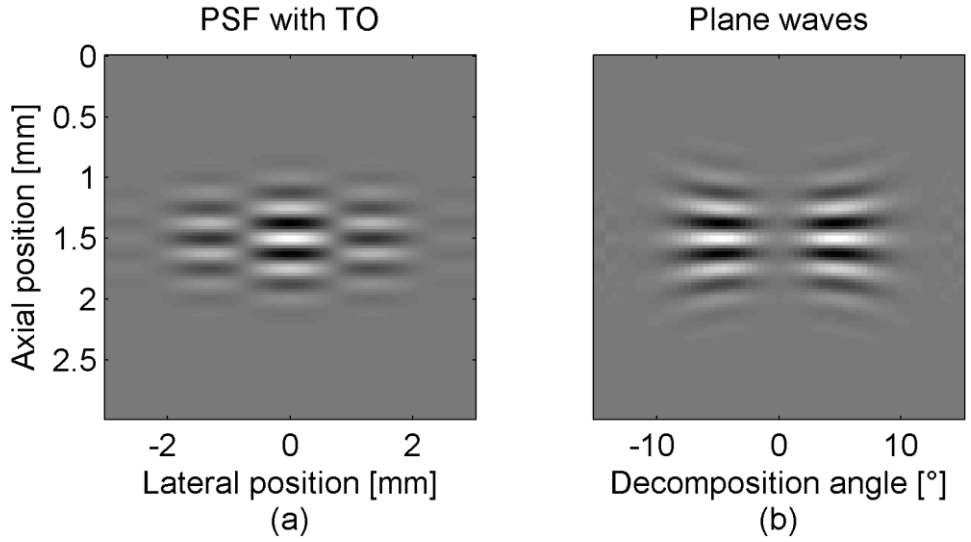

Fig. 6-4: Presentation of PSF with transverse oscillations in (a) and the decomposed plane waves in (b). The center frequency $f_0 = 6MHz$, the lateral wavelength is 3mm, and the decomposition angle is from -15° to 15°.

The previous results correspond to numerical decomposition. The calculation can also be done analytically. Let's consider the PSF as a multiplication of a 2D Gaussian envelope with cosines function which makes the oscillating behavior of the PSF. The oscillating functions in lateral and axial directions are given as

$$\begin{aligned} f(x,z,t) &= \cos\left(2\pi f_x \cdot x\right)\cos\left(2\pi f_0\left(\frac{z}{c}-t\right)\right) \\ &= \frac{1}{2}\cos\left(2\pi f_0\left(\frac{z}{c}-t\right)-2\pi f_x \cdot x\right)+\frac{1}{2}\cos\left(2\pi f_0\left(\frac{z}{c}-t\right)+2\pi f_x \cdot x\right) \\ &= f_1(x,z,t)+f_2(x,z,t) \end{aligned} \quad (5.2)$$

where

$$f_1(x,z,t)=\frac{1}{2}\cos\left(2\pi f_0\left(\frac{z}{c}-t\right)-2\pi f_x \cdot x\right) \quad (5.3)$$

$$f_2(x,z,t)=\frac{1}{2}\cos\left(2\pi f_0\left(\frac{z}{c}-t\right)+2\pi f_x \cdot x\right) \quad (5.4)$$

The 2D Gaussian envelope function is

$$g(x,z,t)=\frac{1}{2\pi}\frac{1}{\sigma_x\sigma_z}\exp\left(-\pi\left[\left(\frac{x}{\sigma_x}\right)^2+\left(\frac{z-ct}{\sigma_z}\right)^2\right]\right) \quad (5.5)$$

The line integral is denoted as [68]

$$H(t;\phi)=\int_{\phi-line} h(x,z,t)dxdz \quad (5.6)$$

as the field sensitivity is given by

$$\begin{aligned} h(x,z,t) &= f(x,z,t)\cdot g(x,z,t) \\ &= f_1(x,z,t)\cdot g(x,z,t)+f_2(x,z,t)\,g(x,z,t) \\ &= h_1(x,z,t)+h_2(x,z,t) \end{aligned} \quad (5.7)$$

where

$$h_1(x,z,t)=f_1(x,z,t)\cdot g(x,z,t) \quad (5.8)$$

$$h_2(x,z,t)=f_2(x,z,t)\,g(x,z,t) \quad (5.9)$$

The integral line is along

$$z=x\tan\theta \quad (5.10)$$

where θ is the angle between the line of integration and the axis of propagation z and x denotes the lateral axis.

And $h(x,z,t)$ could be expanded as

$$h(x,z,t)=\frac{1}{4\pi}\frac{1}{\sigma_x\sigma_z}\exp\left(-\pi\left[\left(\frac{x}{\sigma_x}\right)^2+\left(\frac{x\tan\theta-ct}{\sigma_z}\right)^2\right]\right)\cos\left(2\pi f_0\left(\frac{x\tan\theta}{c}-t\right)-2\pi f_x\cdot x\right)$$
$$+\frac{1}{4\pi}\frac{1}{\sigma_x\sigma_z}\exp\left(-\pi\left[\left(\frac{x}{\sigma_x}\right)^2+\left(\frac{x\tan\theta-ct}{\sigma_z}\right)^2\right]\right)\cos\left(2\pi f_0\left(\frac{x\tan\theta}{c}-t\right)+2\pi f_x\cdot x\right) \tag{5.11}$$

In this case $h_1(x,z,t)$ and $h_2(x,z,t)$ can be rewritten in the form

$$h_1(x,z,t)=\frac{1}{4\pi}\frac{1}{\sigma_x\sigma_z}\exp\left(-\pi x^2\left(\frac{1}{\sigma_x^2}+\frac{\tan^2\theta}{\sigma_z^2}\right)+\pi x\frac{2ct\tan\theta}{\sigma_z^2}-\pi\frac{c^2t^2}{\sigma_z^2}\right)$$
$$\cdot\cos\left(x\left(2\pi\frac{f_0}{c}\tan\theta+2\pi f_x\right)-2\pi f_0\cdot t\right) \tag{5.12}$$

$$h_2(x,z,t)=\frac{1}{4\pi}\frac{1}{\sigma_x\sigma_z}\exp\left(-\pi x^2\left(\frac{1}{\sigma_x^2}+\frac{\tan^2\theta}{\sigma_z^2}\right)+\pi x\frac{2ct\tan\theta}{\sigma_z^2}-\pi\frac{c^2t^2}{\sigma_z^2}\right)$$
$$\cdot\sin\left(x\left(2\pi\frac{f_0}{c}\tan\theta+2\pi f_x\right)+2\pi f_0\cdot t\right) \tag{5.13}$$

So the integration could be simplified as

$$H(t;\theta)=\int_{-\infty}^{+\infty}\exp\left(-\left(ax^2+2bx+d\right)\right)\cdot\cos\left(px^2+2qx+u\right)dx \tag{5.14}$$

The coefficients are given as

$$
\begin{aligned}
a &= \pi\left(\frac{1}{\sigma_x^2}+\frac{\tan^2\theta}{\sigma_z^2}\right)\\
b &= -\pi\frac{ct\tan\theta}{\sigma_z^2}\\
d &= \pi\frac{c^2t^2}{\sigma_z^2}\\
p &= 0\\
q_{1,2} &= \pi\frac{f_0}{c}\tan\theta\pm\pi f_x\\
u &= -2\pi f_0 t
\end{aligned}
\tag{5.15}
$$

The integration of $h(x,z,t)$ and the result $H_n(t;\theta)$ becomes

$$
H_n(t;\theta)=\frac{1}{4\pi}\frac{1}{\sigma_x\sigma_z}\sqrt{\frac{\pi}{a}}\exp\left(\frac{b^2}{a}-d-\frac{q_n^2}{a}\right)\cdot\cos\left(-2\frac{b}{a}q_n+u\right) \tag{5.16}
$$

The final resolution is

$$
H(t;\theta)=H_1(t;\theta)+H_2(t;\theta) \tag{5.17}
$$

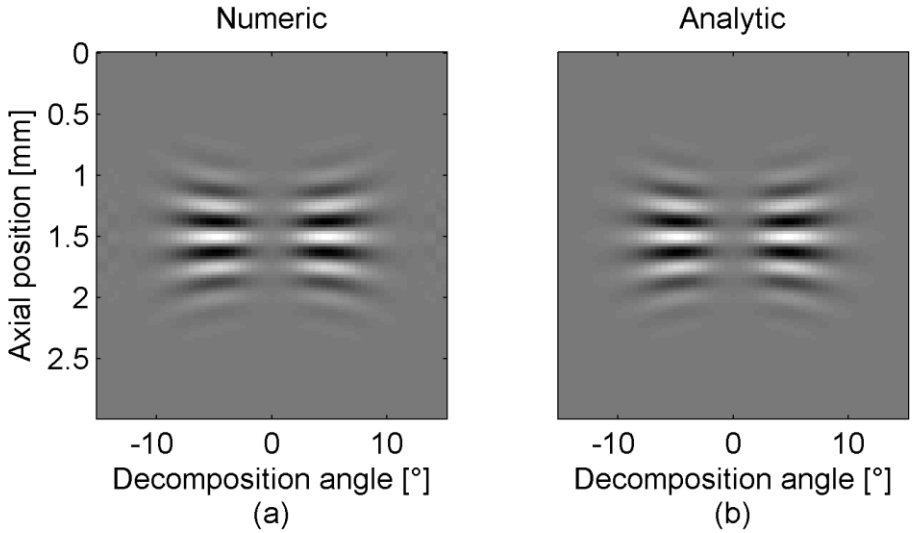

Fig. 6-5: Presentation of decomposed plane waves of the PSF with TO, (a) is the decomposition numerically and (b) is the analytical decomposition result. The decomposition angle is from -15° to 15°.

Note that the time t, the axial position z and the lateral position x are assumed to be local spatial stationary because the propagating time and distance vary a lot but the local parameters are easy to manipulate. To deal with these local parameters, the propagating acoustic pulse is frozen at time t_0 at the depth of z_0, which can be named as global parameters, as the pulse is a spatial distribution signal (2D in the thesis), it

can be regarded as a local distribution, in which manner the time varies locally and axially between $(-\tau:\tau)$ locally and axially, and it relates to the time interval $t_0+(-\tau:\tau)$ globally.

The PSF can be decomposed analytically see in equations (5.15)(5.16) and numerically, the decomposed plane waves are shown in Fig. 6-5 (a) the numerical results and Fig. 6-5 (b) the analytical results, as they are in good accordance with each other, so it is possible to decompose the PSF analytically into a set of plane waves.

6.1.2 Back-propagation theory in linear geometry

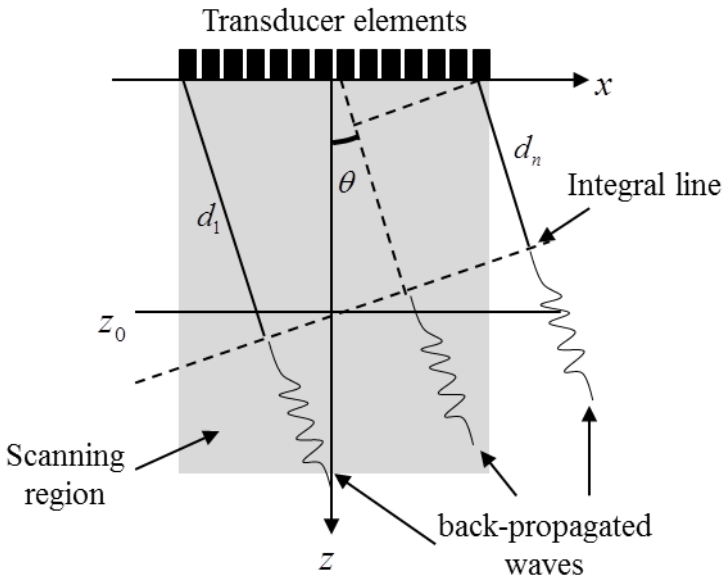

Fig. 6-6: Schema for presentation of back-propagation theory

Different from the proposed back-propagation method in chapter 4, [20, 21] gave a complex back-propagation method. As be presented in the previous subsection, the PSF can be decomposed into a set of plane waves coming from different directions. Thus the plane waves can be regarded as individual waves that could be back-propagated from certain directions to the probe. The sum of all back-propagated waves can be used as excitation signals to obtain the decomposed field. Fig. 6-6 presents the geometry used for back-propagation. The distance from the integral line to a certain element is given as d_i, θ is the decomposition angle, z_0 is the axial position of the field, the integral line rotate around it. The distance $d_i(\theta, z_0)$ can be given as

$$d_i(\theta, z_0) = x_i \cdot \sin(\theta) + z_0 \cdot \cos(\theta) \tag{5.18}$$

where x_i is the position of the ith element. The velocity corresponding to the θ-plane is corrected as given in [68]

$$c_\theta = c/\cos\theta \tag{5.19}$$

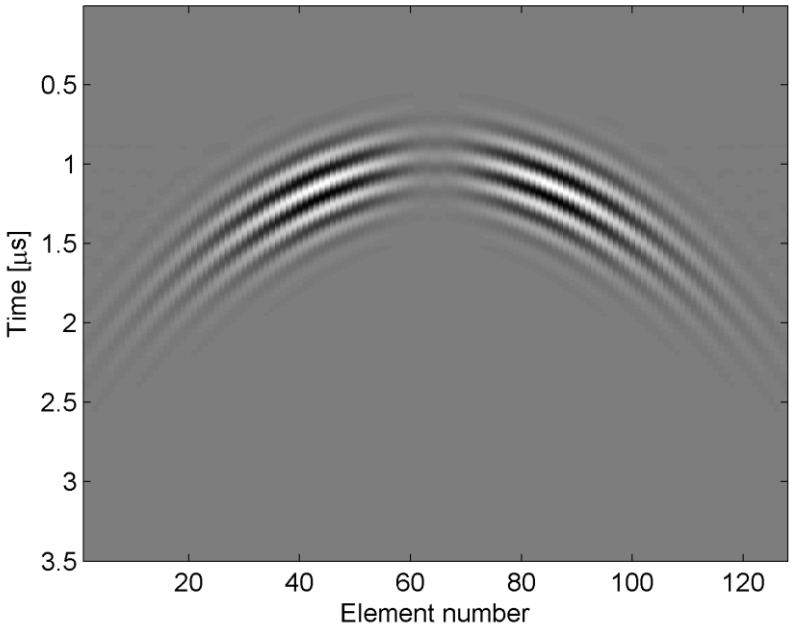

Fig. 6-7: Excitation matrix obtained under the back-propagation of plane waves corresponding to the decomposition of the PSF presented in Fig. 6-8 (a), the decomposition angles are from -15° to 15°

Fig. 6-7 shows the excitation matrix, i.e. the excitation signal used for each element of the probe to obtain the decomposed field. It is calculated by summing up all the back-propagated plane waves. Here the analytical decomposition was used. The abscissa varies with the number of elements, and the ordinate denotes the time.

Each column signal has been used as excitation for each element of the probe and the corresponding simulated PSF is given in Fig. 6-8 (b). The good similarity of the theoretical PSF in Fig. 6-8 (a) and the simulated one in (b) demonstrated the feasibility of this analytical plane wave decomposition method and the back-propagation theory.

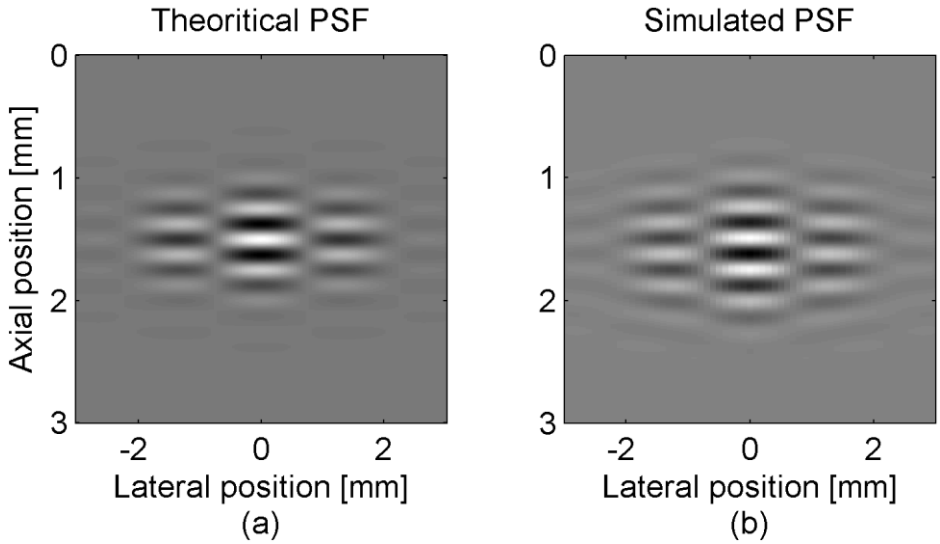

Fig. 6-8: Comparison of the theoretical PSF in (a) and the simulated PSF in (b) obtained using the excitation matrix given in Fig. 6-7.

6.2 PSF quality evaluation

In order to evaluate the performance of this plane wave decomposition theory, the quality of PSF is evaluated using the measure given in Equation(5.1), the RMSE. The results are compared with those obtained by using the classical Fourier relation method.

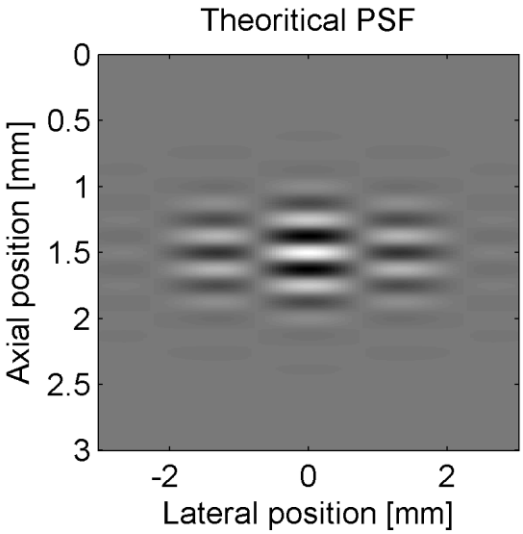

Fig. 6-9: Presentation of theoretical PSF

In order to show the difference between the two methods, Fig. 6-10 shows the PSF obtained under Fourier relation in Figure (a) and under the plane wave decomposition

method in Figure (b), as compared to the theoretical PSF in Fig. 6-9, we can see clearly the difference.

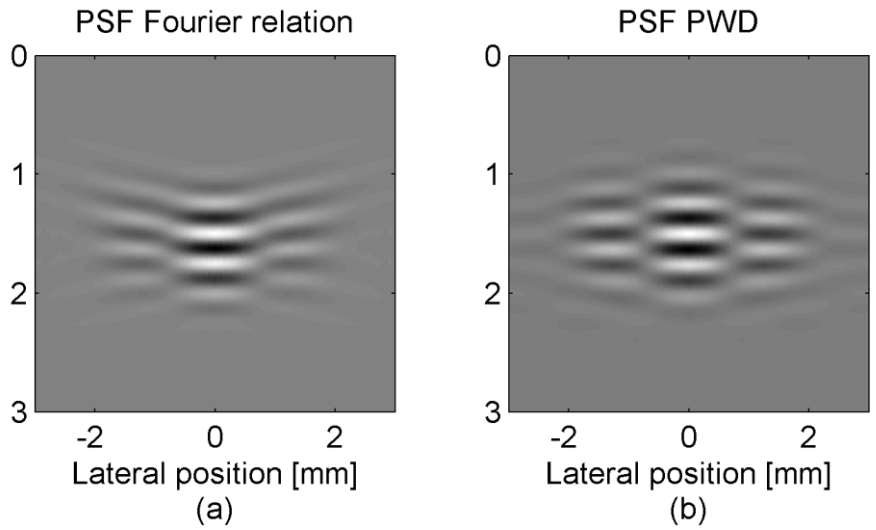

Fig. 6-10: Presentation of PSF obtained using Fourier relation (a) and the plane wave decomposition method (b).

The comparison of RMSE obtained using Fourier relation and the plane wave decomposition strategy, respectively, can be seen in Fig. 6-11 (a) and (b), respectively. The result is obtained for PSF located laterally from -5 mm to 5 mm and axially from 10 mm to 50 mm. For both methods, the RMSE changes a little horizontally but increases obviously in vertical direction, which indicates that the quality of PSF is poorer at larger depths but only little influenced by the lateral position in linear geometry. Furthermore, it is clear to see that the RMSE is smaller using the plane wave decomposition strategy than using the Fourier relation.

The verification of the improvements brought by the plane wave decomposition strategy in linear geometry has been verified both visually and numerically.

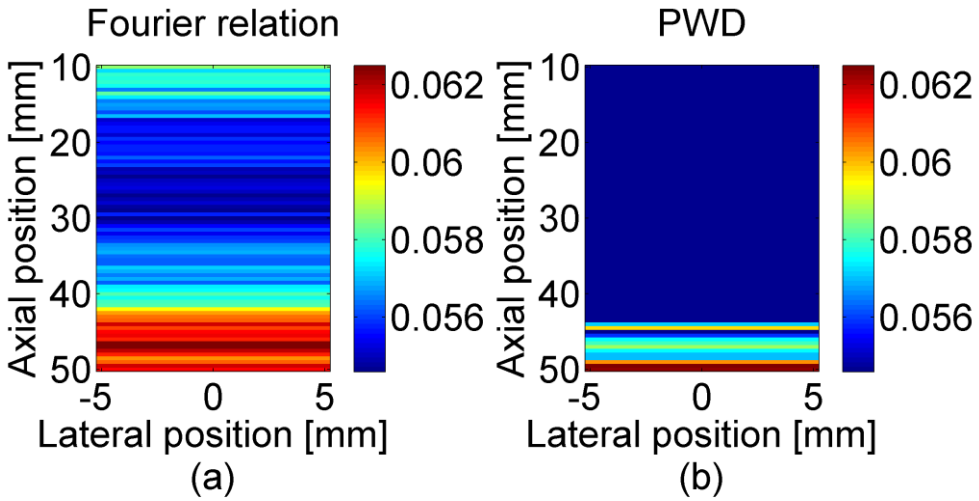

Fig. 6-11: Presentation of RMSE of PSF for the Fourier relation method in (a) and the decomposition-back-propagation-transmission strategy in (b).

6.3 Adaptation to sectorial geometry

The good performance of the plane wave decomposition theory stimulates the idea to adapt it into sectorial scanning aiming at getting good PSF quality in that geometry. In this section, the contribution of the adaptation of plane wave decomposition and the back-propagation methods will be described. All the simulations will be done using the parameters given in Table 3. The PSF in polar coordinate is presented in Fig. 6-12. The ordinate changes with the axial position and the abscissa varies with the scanning directions from -10° to 10°.

Table 3: Simulation parameters

f_0	$3.5MHz$
f_s	$50MHz$
λ_θ^{PSF}	8°
σ_θ^{PSF}	12°
c	1540
Kerf	0.2 mm
Width	0.14 mm
Number of elements	64

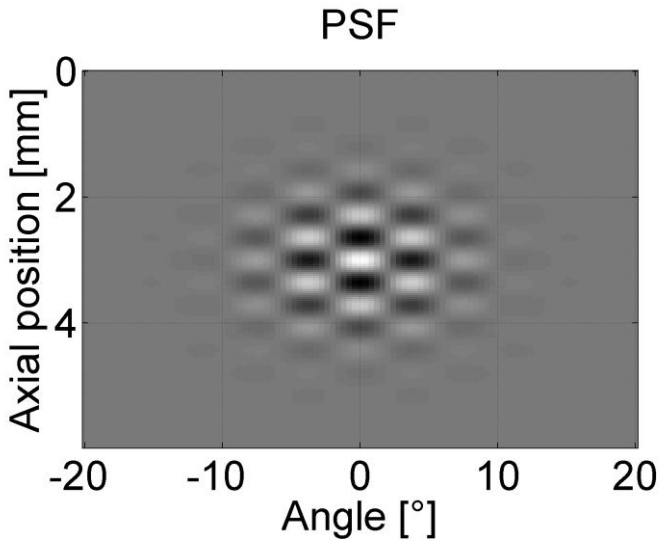

Fig. 6-12: Presentation of PSF in sector geometry, the parameters are: the center frequency is $f_0 = 2.1MHz$, lateral wavelength $\lambda_\theta^{PSF} = 8°$, $\sigma_\theta^{PSF} = 12°$

6.3.1 Plane wave decomposition in sectorial geometry

Taking into account the characteristics of sector scanning, the decomposition is done after converting the PSF from polar coordinates as given in Fig. 6-12 into Cartesian coordinates. Fig. 6-13 (a) presents the converted PSF in Cartesian coordinate in which the unit of abscissa is [mm], by decomposing it from -15° to 15° the plane waves decomposition can be seen in Fig. 6-13(b).

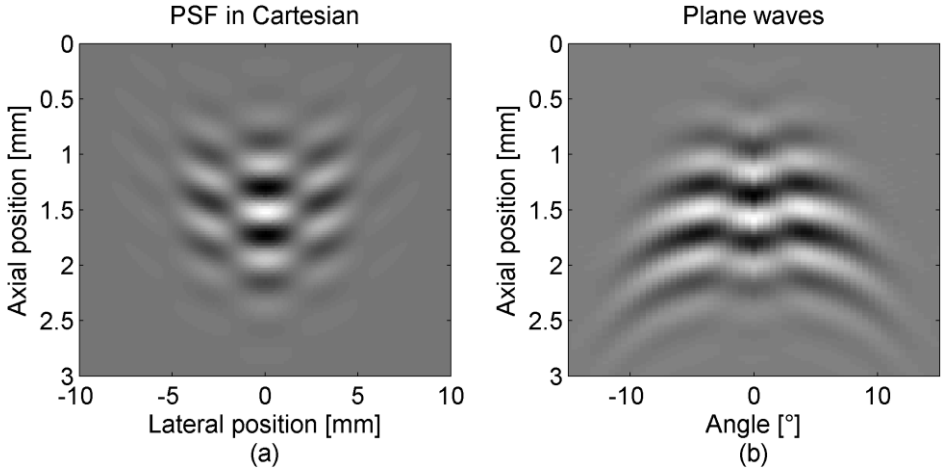

Fig. 6-13: Presentation of PSF in Cartesian coordinate (a) and the corresponding plane wave decomposition (b).

As in linear geometry, see in Fig. 6-6, the decomposed planes waves are back-propagated to the probe, and after summation of the back-propagated signals from different angles, one obtains the exciting signals for all scanning directions.

In order to evaluate the feasibility of this approach, the next subsection will show the evaluation of the quality of PSF, and the result will be compared with the conventional Fourier relation method.

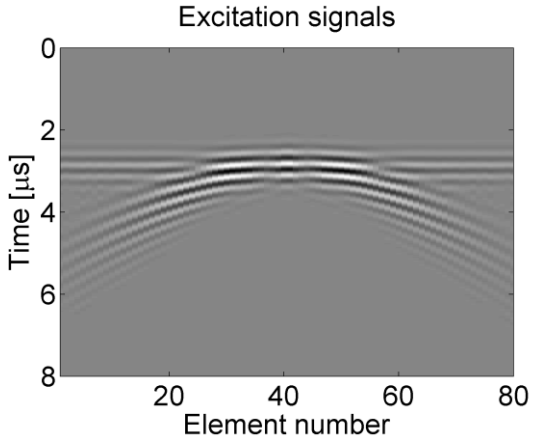

Fig. 6-14: Presentation of back-propagated signals used as excitation signals

6.3.2 Quality of PSF

A qualitative comparison of the PSF quality can be observed in Fig. 6-15 and in Fig. 6-16. Fig. 6-15 shows the PSF acquired in front of probe (0°) using Fourier relation (a) and the PWD theory (b). The corresponding RMSE for Fourier relation is 0.07 and for PWD method is 0.04. The improvement is also illustrated on the side of the probe (10°) in Fig. 6-16. Here the RMSE of Fourier relation is 0.08 and for PWD theory it is 0.05. This initial results show that PWD theory is a possible way to increase the quality of PSF not only in linear geometry but also in sectorial geometry.

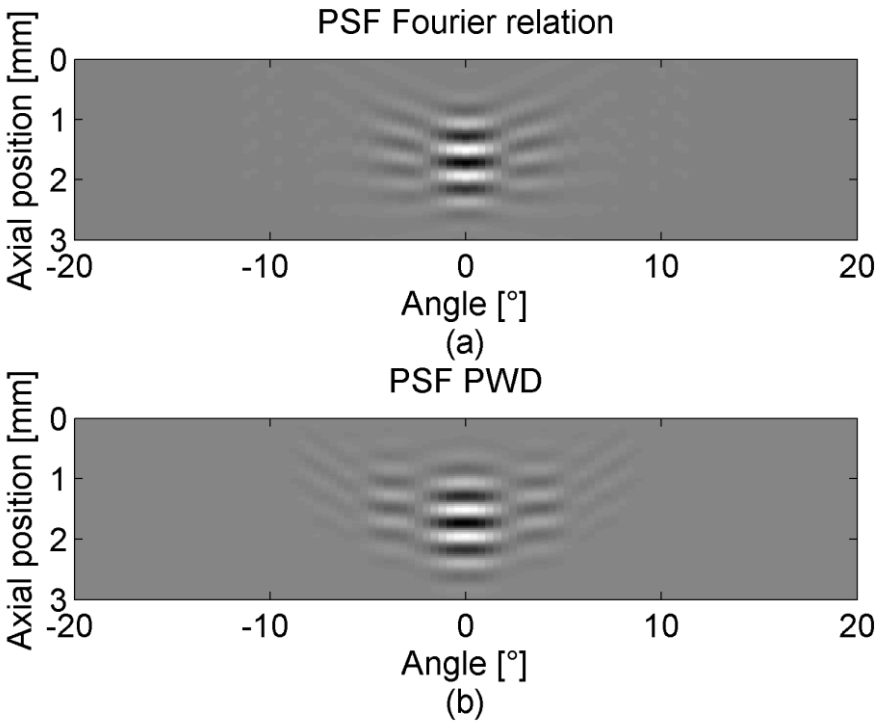

Fig. 6-15: PSF in front of probe (0°) obtained using Fourier relation (a) and the PWD theory (b)

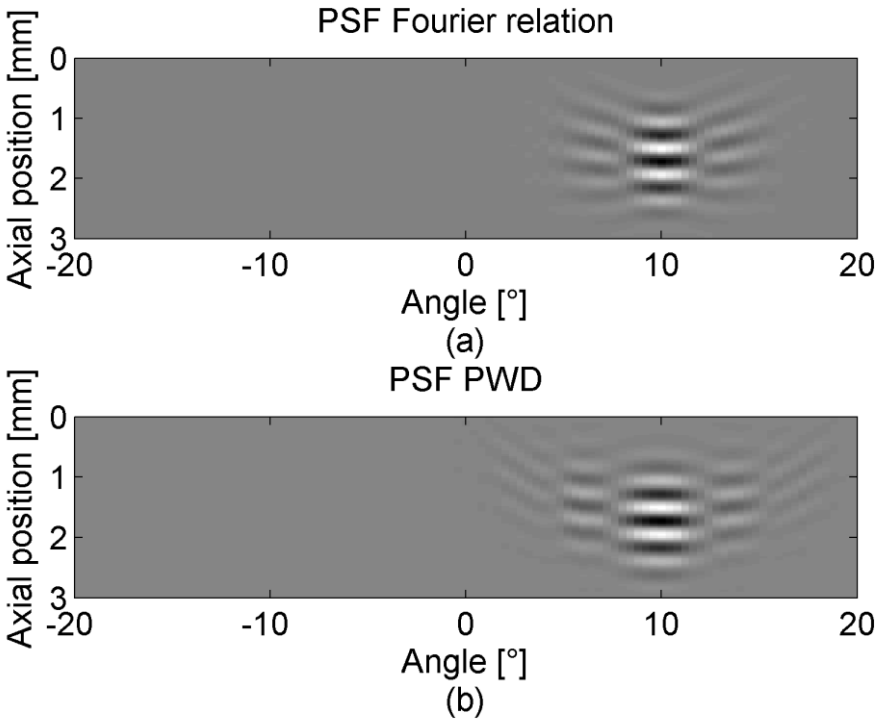

Fig. 6-16: Presentation of PSF on the side of probe (10°) obtained using Fourier relation (a) and the PWD theory (b)

6.4 Conclusion

In this chapter the plane wave decomposition method, the back-propagation theory and the transmission strategy in linear geometry have been introduced and they have been verified with simulation results. In view of the good performance in linear geometry, the contribution of adapting them to sector scanning has been done. Comparison between the PSF quality in front and on the side of probe indicate that PWD could represent an interesting candidate to improve the PSF quality even more for TO in echocardiography. The further work will concentrate on confirming the performance in more situations and for different parameters as well as in vivo.

Chapter 7

Conclusions and perspectives

Contents

7.1 Conclusions

This thesis tries to address the limitation of conventional beamforming design strategies, which are not able to produce a beamformer for TO in sectorial geometry. The resolution to this problem that we have proposed is to use back-propagation method to improve the quality of TOs obtained in the PSF compared with that from the conventional Fourier relation.

In order to make sure that readers understand well this thesis, the explanation of principles of ultrasound imaging and beamforming are presented step by step. The principle of ultrasound imaging is described from the elementary transmission and reception, different imaging arrays to the different echography modes. Afterwards, the imaging model which is PSF used in this thesis is explained. Introducing the principle of beamforming techniques is necessary. Several general beamformer methods are described, including the delay-and-sum method, the synthetic aperture imaging, the parallel receiving beamforming, spatial compounding and adaptive beamforming. More in specific, the methods for designing the transverse oscillation beamformer are introduced generally, which are the Fraunhofer approximation, Sumi's method and the Fourier relation. In the conclusion, the limits of these methods are discussed and illustrated. The contribution of this thesis-the so called back-propagation method- tries to tackle these limitations.

The back-propagation method is proposed under two principles: the wave propagation and the reciprocity theorem. Following these principles, the transverse oscillations beamforming is improved for acquiring better PSF in the the sectorial scanning typically used in echocardiography. The improvement is investigated in Chapter 5, by comparing the proposed back-propagation method with the Fourier relation method. In this chapter, the study of apodization function varying with angles for two methods is presented. The improvement evaluation is first given by comparing the quality of PSF obtained by two methods, the measure adopted to assess the quality is the RMSE method, which is used to compare the similarity of acquired PSF to theoretical one. The quality of PSF is studied spatially and by varying the TOs parameters. It presents that the proposed back-propagation method can improve the quality of PSF no matter in different positions by keeping the λ_θ^{PSF} and σ_θ^{PSF} constant, or changing the TOs parameters λ_θ^{PSF} and σ_θ^{PSF} and hold the PSF at the same position. The further study of the improvement is demonstrated by doing motion estimation, both to the simple displacements and simulated realistic cardiac motion. The quantitative results give the positive confirmation that the proposed back-propagation

method slightly improves the estimation motion results. The experimental results for comparison of the quality of PSF present visually and also quantitatively the possibility that the proposed method ameliorates the PSF in practical application.

As an extension of the proposed back-propagation method we have also proposed to adapt the plane wave decomposition method for the situation of sectorial scanning. The adaptation to sectorial geometry presents good performance for PSF on face and on the side of probe, this will motivate us to further implant it into motion estimation in echocardiography.

7.2 Perspectives

Thanks to the experiments we confirmed the experimental feasibility of the back-propagation method and we have shown the quality improvement of PSF obtained under back-propagation method compared with Fourier relation. The further study would be conducted to investigate the performance of the proposed back-propagation method comparing with the Fourier relation method in the in-vivo data. In this study, both methods would be implanted into an ultrasound research platform named ULA-Op [64], and the acquisition of two imaging modalities is interleaved, in which case it will ensure the comparability of the two imaging modes. The investigation will concentrate on estimating the cardiac motion. Once it confirms that the motion estimation results of back-propagation perform are better than that of the Fourier relation, the back-propagation method could be used in clinical diagnosis in the field of echocardiography.

Furthermore, the motion estimation in this paper is only committed to 2D images, but it's 3D in reality, so the further work can be put into the 3D motion estimation. On this step, the phased 1D probe is replaced by 1) a 2D mechanical probe to obtain 3D volume, each frame of this volume is acquired by mechanical move the probe; or by 2) a 2D array probe which can generate 3D volume on one shot, in this case it can satisfy the real-time acquisition.

The use of unfocused emission in our study may decrease the SNR, further study can dedicate into improve it. And the back-propagation is limited not only in echocardiography, but also in the application to elastography and blood flow fields, etc.

In demonstration of the plane wave decomposition method, it works well in linear geometry and in sectorial scanning only for the PSF in front of prove, but it limited for sectorial scanning, so the further work will be dedicated to adapting it for the complete sectorial imaging and confirming it in the experimental in vivo analysis..

Résumé en français

Contents

I. Introduction

1. Echographie et estimation de mouvement

Les ultrasons sont des ondes de pression dont la fréquence d'oscillation est supérieure à 20 kHz, mais qui n'est pas différentes des sons audibles du fait de sa nature physique, mais uniquement par le fait qu'elles sont en dehors de la limite supérieure de la gamme de fréquences de l'audition humaine.

L'utilisation des ultrasons pour les applications médicales a commencé dans les années 1950s et a eu un large développement dans les années 1970s [8]. Depuis plus de quarante ans, les ultrasons sont devenus une technologie de diagnostic clinique importante.

Avec les avantages d'être non invasive, non ionisante, d'avoir un coût relativement faible [9] par rapport à d'autres modalités d'imageries telles que les rayons-X, la tomographie et la résonance magnétique, et du fait qu'il s'agisse d'une modalité « transportable » l'échographie a été largement utilisée en diagnostic clinique. La rapidité de propagation de l'onde ultrasonore en fait une imagerie dite temps réel et particulièrement adaptée à l'estimation de mouvement. On peut citer deux applications typiques: l'une est de mesurer et de visualiser le flux sanguin en utilisant des techniques dites Doppler; l'autre concerne l'estimation de mouvement des organes mobiles. Dans le cadre de cette thèse, nous allons nous concentrer sur l'échocardiographie. Pourquoi l'échocardiographie est-elle importante? Le cœur est un organe mobile dont le mouvement peut être affecté par différentes pathologies, telles que l'ischémie ou l'infarctus qui peut modifier le mouvement cardiaque. En conséquence, il est d'une grande importance de fournir aux médecins un appareil d'imagerie qui permette d'imager le mouvement du cœur au cours du cycle cardiaque. Dans ce cas, l'échographie est un excellent candidat: comme mentionné ci-dessus, elle permet une acquisition très rapide par rapport à d'autres modalités d'imagerie.

En échocardiographie, la plupart du temps, seule une projection du mouvement cardiaque 3D est visualisée sous forme de séquence 2D d'images. Beaucoup de recherches ont été consacrées à développer des techniques d'estimation de mouvement à partir de séquences d'images échographiques, mais il n'est pas facile d'estimer le mouvement dans la direction transverse, c'est-à-dire la direction perpendiculaire à l'axe des ultrasons, avec une grande précision. Cela représente une forte limitation des techniques d'estimation de mouvement actuelles. VF-Figure 1 définit la géométrie d'acquisition: le faisceau se propage dans la direction axiale et la direction latérale

également appelée direction transverse est la direction perpendiculaire à l'axe du faisceau.

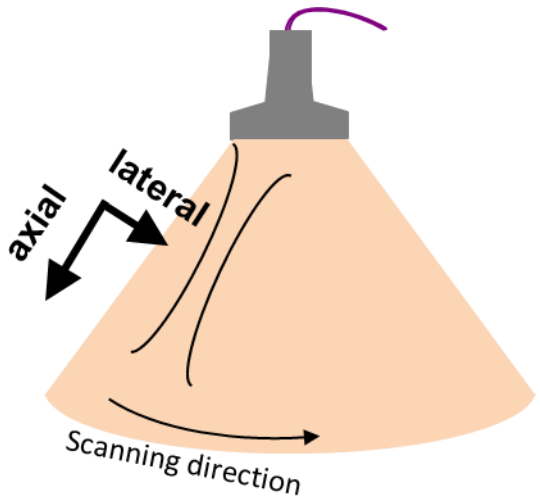

VF-Figure 1: Définition du repère d'imagerie. La direction dite axiale correspond à la direction de propagation des ultrasons. La direction orthogonale est dite latérale ou transverse.

2. Limitations des acquisitions classiques

Il a été montré que l'estimation du déplacement le long de la direction axiale peut être très précise. Ce grandement lié aux oscillations qui sont naturellement présentes dans les signaux RF. En observant la réponse impulsionnelle spatiale (en anglais Point Spread Function, PSF) dans la VF-Figure 2 (a), l'oscillation rapide du profil axial est très claire VF-Figure 2 (b), tandis que le profil latéral s'apparente à une enveloppe de forme gaussienne. Il n'est alors pas facile d'estimer le mouvement dans la direction transverse avec une grande précision, car une acquisition classique ne peut pas donner les mêmes caractéristiques d'oscillation dans la direction latérale que dans la direction axiale.

Comme nous le verrons dans la suite, ce problème peut être résolu en modifiant la formation de l'image et en utilisant un schéma de formation de voie qui conduit à des PSF ayant, dans la direction latérale de l'image, les mêmes caractéristiques d'oscillation que dans la direction axiale.

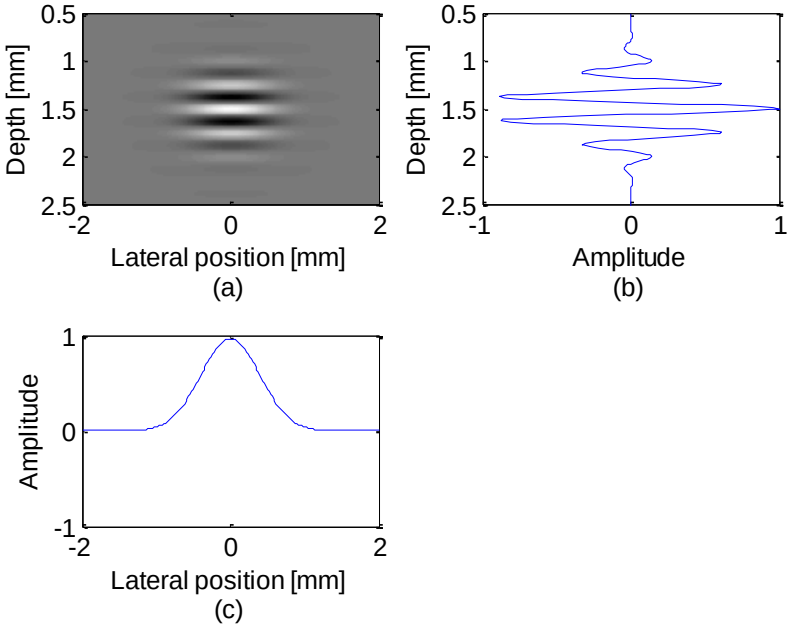

VF-Figure 2: PSF classique (a), profil axial montrant des oscillations (b) et profil latéral ayant la forme d'une enveloppe gaussienne (c).

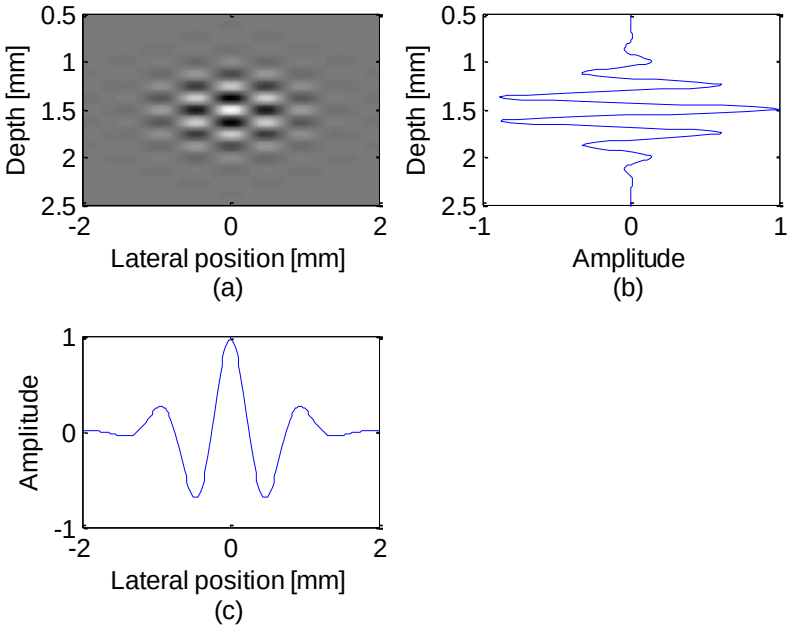

VF-Figure 3: PSF avec des oscillations transverses (a), profil axial (b) et profil latéral (c) présentant également des oscillations.

3. Objectif de la thèse

Afin de permettre l'estimation précise du mouvement transverse, des PSF présentant des profils latéraux avec oscillations ont été imaginées. La méthode des oscillations transverses (OT) a été initiée à la fin des années 1990 dans le domaine de l'estimation des flux sanguins [10, 11]. Plusieurs groupes ont travaillé sur ces méthodes. Jusqu'à présent, les méthodes OT ont été appliquées dans l'estimation du flux sanguin par Jensen et al. [11-13] et Anderson [10], dans l'élastographie par Sumi [14, 15] et notre groupe [16, 17], et en échocardiographie.

Ces études ont montré que les images OT peuvent conduire à une meilleure estimation de mouvement 2D en géométrie linéaire. Le formateur de voies permettant de produire des images OT en géométrie linéaire s'appuie sur l'approximation de Fraunhofer, qui permet de relier la fonction de pondération des éléments et le profil latéral de la PSF du système par une simple transformée de Fourier. L'application des OT en échocardiographie implique l'adaptation de cette technique pour la géométrie d'acquisition sectorielle. Nos travaux préliminaires [18] ont montré que, la formation de voie classique s'appuyant sur l'approximation de Fraunhofer conduit à des images d'OT non-optimales. Par conséquent, dans cette thèse, nous proposons une nouvelle approche de conception du formateur de voie adapté au balayage sectoriel. Comme cela sera décrit plus tard dans la thèse, l'approche proposée est basée sur le théorème de réciprocité et utilise la rétro-propagation (BP).

L'objectif de cette thèse est d'adapter la formation d'image OT pour l'échocardiographie dans le but d'améliorer l'estimation de mouvement 2D et en particulier le mouvement latéral.

II. Contexte

1. Imagerie ultrasonore

Le transducteur est le composant de base et le plus important d'un système d'imagerie ultrasonore. Il a deux fonctions principales. L'une est de transmettre des signaux ultrasonores, et l'autre est de recevoir des échos provenant du milieu imagé. En émission, un signal ultrasonore est généré en excitant le transducteur piézoélectrique avec un signal électrique. Les signaux transmis dans le corps sont soumis aux phénomènes de diffraction, d'atténuation, de diffusion et de réflexion. Les échos reçus font alors vibrer le transducteur qui les traduit en signaux électriques qui sont ensuite transformés en une image numérique par le scanner. L'affichage en échelle de gris ou couleur sur l'écran dépend de l'amplitude des signaux électriques.

Trois types de sondes ultrasonores de base qui sont constituées par une barrette d'éléments sont en général utilisés ; les sondes linéaires, les sondes convexes et les sondes dites à décalage de phase ou phased arrays en anglais.

Les modes de visualisation de base en échographie incluent le mode A (amplitude), le mode M (mouvement), le mode B (luminosité) et le mode C (profondeur constante) .

La PSF est l'image qui serait générée par un seul diffuseur d'amplitude unitaire. La PSF est très utile pour caractériser le système d'imagerie en particulier pour évaluer la résolution dans toutes les directions spatiales. En supposant la linéarité du système d'imagerie, et que le milieu est constitué par un ensemble de diffuseurs, la formation de l'image peut être considérée comme la somme d'une collection de PSFs.

2. Etat de l'art de la formation de voie

La formation de voie est le nom de la technique de traitement de signal utilisée pour construire un faisceau à partir de la combinaison des signaux obtenus au niveau des transducteurs individuels. Les techniques de formation de voie ultrasonore [21] ont beaucoup évolué, mais l'approche la plus couramment utilisée est la méthode délais et somme. Avec le développement de la technologie, des méthodes de formation de voie très élaborées incluant l'imagerie par synthèse d'ouverture [22], par onde plane [23], l'imagerie par composition [24, 25] et la formation de voie adaptive [26], etc., sont proposées afin de répondre à différents besoins.

On peut citer également des techniques de conception de formation de voie plus spécifiques pour des objectifs précis. Par exemple, l'amélioration de la profondeur de champ [31-33], la réduction du niveau de champ pour éviter les points chauds potentiels [34], la minimisation des artefacts de formation de voie indésirables [35].

Le principe des OT consiste à modifier la formation des images ultrasonores en utilisant une formation de voie qui est capable de produire un champ ultrasonore avec des oscillations axiales et transverses, tandis que les formateurs de voies classiques conduisent à des oscillations axiales seulement. La conséquence très intéressante, est que la signature du signal rétrodiffusé reçu d'un groupe mobile de diffuseurs qui traversent un tel champ sonore porte des informations à la fois sur la vitesse axiale et transverse des diffuseurs. Comment ces images sont obtenues et exploitées ainsi que leur potentiel pour différentes applications a été résumée dans [49].

En géométrie linéaire, les oscillations latérales correspondent au profil latéral exprimé dans l'équation (8.1), qui est la multiplication d'une enveloppe gaussienne

avec une fonction cosinus. Dans cette équation, λ^{PSF} est la longueur d'onde attendue des oscillations transverses, σ^{PSF} est la largeur à mi-hauteur de l'enveloppe gaussienne qui limite l'étendue de la PSF, et $u^{PSF} = 1/\lambda^{PSF}$.

$$h_r(x) = \cos(2\pi x u^{PSF}) \cdot \exp(-\pi(\frac{x}{\sigma^{PSF}})^2) \tag{8.1}$$

La fonction de pondération des éléments est obtenue par transformation de Fourier inverse du profil de la PSF et s'écrit comme suit:

$$w(x_i^{Apo}) = \frac{1}{2}(\exp^{-\pi(\frac{x_i^{Apo} - x^{Apo}}{\sigma^{Apo}})^2} + \exp^{-\pi(\frac{x_i^{Apo} + x^{Apo}}{\sigma^{Apo}})^2}) \tag{8.2}$$

où x_i^{Apo} est la position latérale du i^{ème} élément, $\pm x^{Apo}$ sont les positions des deux pics et σ^{Apo} est la largeur à mi-hauteur de chaque pic. Les paramètres de l'équation (8.2) peuvent être reliés aux paramètres de la PSF de l'équation (8.1) et à la profondeur y comme suit :

$$x^{Apo} = \lambda y / \lambda^{PSF} \tag{8.3}$$

$$\sigma^{Apo} = \sqrt{2}\,\lambda y / \sigma^{PSF} \tag{8.4}$$

où λ est la longueur d'onde de l'impulsion émise. Le profil latéral de la PSF donné en (8.1) et la fonction de pondération donné en (8.2) sont représentés sur la VF-Figure 4.

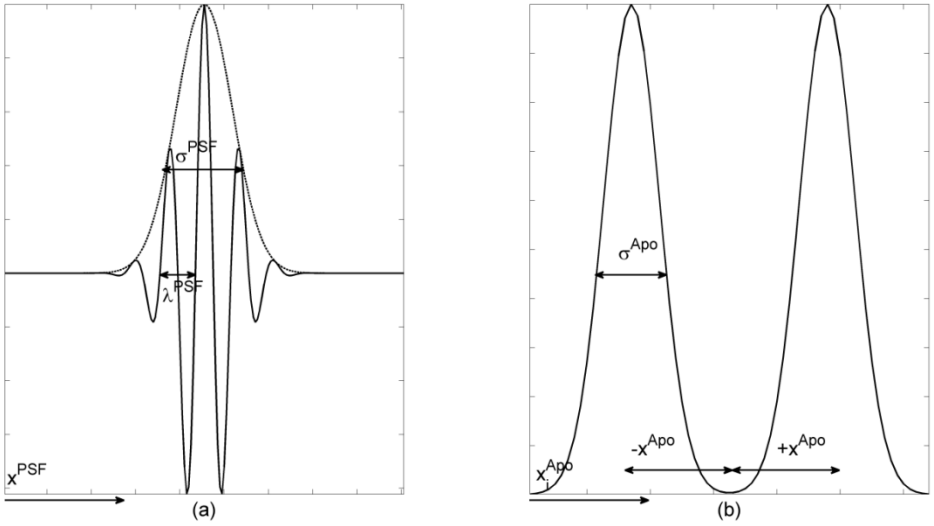

VF-Figure 4: Représentation des différentes variables du profil latéral de la PSF (a) et la fonction de pondération (b). Les relations entre x^{Apo} et $u^{PSF}=1/\lambda^{PSF}$ ainsi qu'entre σ^{Apo} et σ^{PSF} sont données équations (8.3) et (8.4).

Afin d'adapter le cadre ci-dessus pour la géométrie sectorielle, nous transformons les paramètres du modèle cartésien en coordonnées polaires [36]. La position des deux pics et l'écart-type (qui sont exprimées en [m]) de la fonction de pondération sont alors donnés comme suit:

$$x_\theta^{Apo}=\lambda/\lambda_\theta^{PSF} \tag{8.5}$$

$$\sigma_\theta^{Apo}=\sqrt{2}\lambda/\sigma_\theta^{PSF} \tag{8.6}$$

où λ_θ^{PSF} est la longueur d'onde latérale prévue du profil de PSF exprimée en degrés, σ_θ^{PSF} est la largeur à mi-hauteur du profil latéral de la PSF.

III. Contribution

1. Formation de voie par rétro-propagation

1) Théorie

Dans le but de mieux respecter la physique de la propagation des ondes en échocardiographie, nous proposons une méthode de conception du formateur de voie spécifique basée sur la rétro-propagation (BP) et le théorème de réciprocité, en vertu de laquelle les paramètres dépendent de la direction du faisceau. Cette approche permet de s'adapter à la géométrie sectorielle sans faire l'approximation de Fraunhoffer.

En géométrie sectorielle, le champ de pression et la fonction de pondération peuvent être transformés en coordonnées polaires comme suit:

$$p(\theta,r)=k_1\sum_{i=1}^{N}w(x_i^{Apo})\frac{e^{\frac{j2\pi r_i}{\lambda}}}{r_i} \tag{8.7}$$

$$w(x_i^{Apo},r_0)=k_2\int_{-\infty}^{+\infty}p(\theta,r_0)\frac{e^{\frac{j2\pi r_0(i,\theta)}{\lambda}}}{r_0(i,\theta)}d\theta \tag{8.8}$$

où $p(\theta,r)$ est le champ de pression variable avec l'angle θ, r la distance entre la sonde et le point d'intérêt, k_1 et k_2 sont des constantes, x_i^{Apo} est la position du i^{ème} élément, r_i est la distance entre le i^{ème} élément et le point d'intérêt; $w(x_i^{Apo},r_0)$ est la fonction de pondération pour un certain rayon de balayage r_0 qui devrait être utilisée pour obtenir la pression $p(\theta,r_0)$, $r_0(i,\theta)$ est la distance du i^{ème} élément à un point qui se trouve le long du rayon de balayage r_0 dans la direction θ.

En gardant la position axiale inchangée à 40 mm, la fonction de pondération en fonction de l'angle est représentée dans la VF-Figure 5. La VF-Figure 5 (a) montre la fonction de pondération de -30 ° à 30 °, la modification des profils en fonction de la direction est mise en évidence par la superposition des profils de pondérations aux angles -15 ° et 15 ° sur la VF-Figure 5 (b).

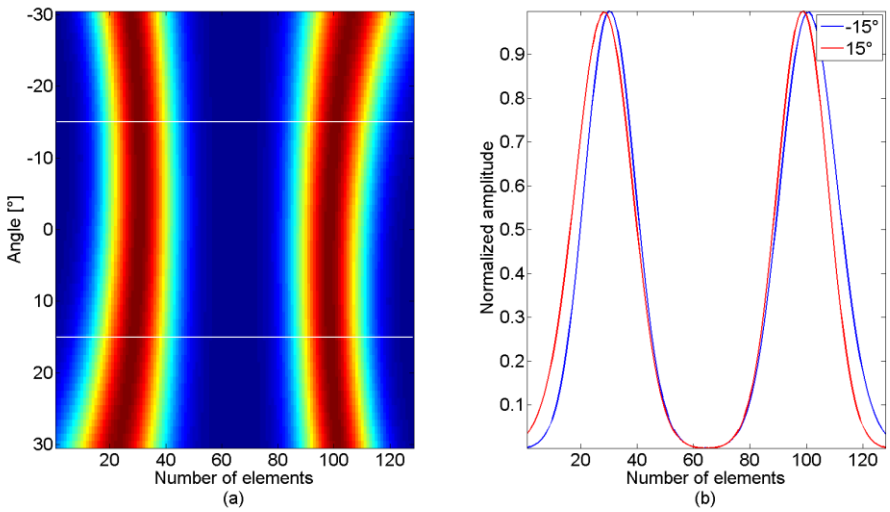

VF-Figure 5: Présentation de la fonction de pondération obtenue en géométrie sectorielle, le secteur de balayage s'étend de -30 ° à 30 ° et la position axiale est considérée fixe et égale à 40 mm. Figure (a) donne la pondération

obtenue. Figure (b) montre les profils à -15 ° (ligne bleue continue) et 15 ° (ligne rouge continue). $f_0 = 2.1MHz$, $\lambda^{PSF}{}_{\theta} = 8°$, and $\sigma_{\theta}^{PSF} = 1.5\lambda_{\theta}^{PSF}$.

2) Résultats

Fonction de pondération

Pour comparer la méthode de rétro-propagation et la méthode de Fourier classique, nous avons étudié les fonctions de pondération obtenues à la profondeur de 60 mm, et pour les directions de -30° à 30°. La fonction de pondération obtenue selon la méthode de Fourier ne présente pas de variation avec les angles comme c'est le cas dans la méthode de rétro-propagation.

Évaluation de la qualité des PSFs

Afin de mesurer la performance de la méthode de rétro-propagation proposée et celle de l'approche classique de Fourier, la qualité des PSF est mesurée par l'erreur quadratique moyenne (RMSE) entre PSF souhaitée et PSF obtenue.

Le RMSE est obtenue à des profondeurs de 60 à 100 mm et l'angle de balayage de -30° à 30° dans la VF-Figure 6. La comparaison des VF-Figure 6 (a) et (b) montre que le RMSE associé à des angles de balayage importants augmente avec la méthode de Fourier alors qu'il diminue pour la rétro-propagation. Ce dernier est toujours inférieur au RMSE obtenu avec Fourier.

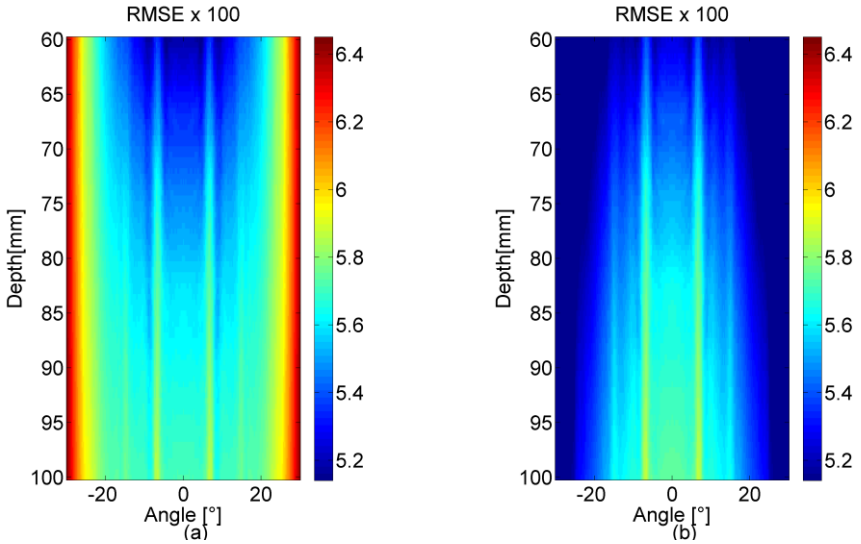

VF-Figure 6: Présentation des cartes d'erreur(RMSE) obtenues avec la méthode de Fourier (a) et de rétro-propagation (b) t, les paramètres sont $\lambda_{\theta}^{PSF} = 8°, \sigma_{\theta}^{PSF} = 12°, f_0 = 2.1MHz$.

Influence des paramètres

L'influence de différents paramètres est présentée dans cette partie. La longueur d'onde latérale λ_θ^{PSF} varie de 6° à 12°, la largeur à mi-hauteur de l'enveloppe gaussienne de la PSF σ_θ^{PSF} varie de 6° à 24°. L'influence est étudiée pour un diffuseur à la même profondeur de 80 mm mais situé en face de la sonde ($\theta = 0°$) ou positionné sur le côté de la sonde ($\theta = 30°$).

Les RMSEs obtenus pour le diffuseur en face de la sonde ($\theta = 0°$) sont très proches pour les deux méthodes. Ceci est cohérent avec le fait que cette situation corresponde à l'endroit où l'approximation de Fraunhofer, et donc la formation de voie à base de Fourier sont les plus valables. La BP ne conduit alors qu'à une légère amélioration.

Pour le diffuseur situé sur le côté de l'image ($\theta = 30°$), la rétro-propagation améliore nettement la PSF. Ceci est cohérent puisque c'est dans cette région que l'approximation de Fourier est la plus approximative et représente le moins la réalité physique du phénomène mis en jeu.

Précision en estimation de mouvement

Parce que notre méthode est basée sur des différences de phase, on ne peut pas estimer les mouvements plus grands que la demi-longueur d'onde axiale (0.36 mm) ou latérale (4°). Afin de quantifier les limites de la méthode, des simulations simples sont tout d'abord effectuées avec des mouvements simples de translation. Les mouvements se situent dans l'intervalle [0° - 6.4°] dans la direction transverse et [0-0.6] mm dans la direction axiale. Les valeurs maximales sont donc plus grandes que la moitié de la longueur d'onde latérale et axiale, ce qui permet d'évaluer les limites de la technique.

A. Mouvement simple

Pour une compréhension claire de caractérisation de l'estimation de mouvement, la VF-Figure 7 présente la procédure mise en œuvre qui consiste en:

a. Obtenir l'image I_2 en déplaçant les diffuseurs de la valeur connue d;
b. Considérer une région d'intérêt ROI_1^k dans I_1, et ROI_2^k dans I_2 ;
c. Extraire la phase des deux ROIs et calculer le déplacement $\hat{d}$ en utilisant l'estimateur basé sur la phase [45];
d. Calculer l'erreur quadratique moyenne de l'estimation $\hat{d}$ pour le déplacement théorique d ;

Prendre la ROI dans une autre position, répéter les étapes b à d jusqu'à ce que les régions d'intérêt aient couvert l'image I_1 et/ou I_2 en entier.

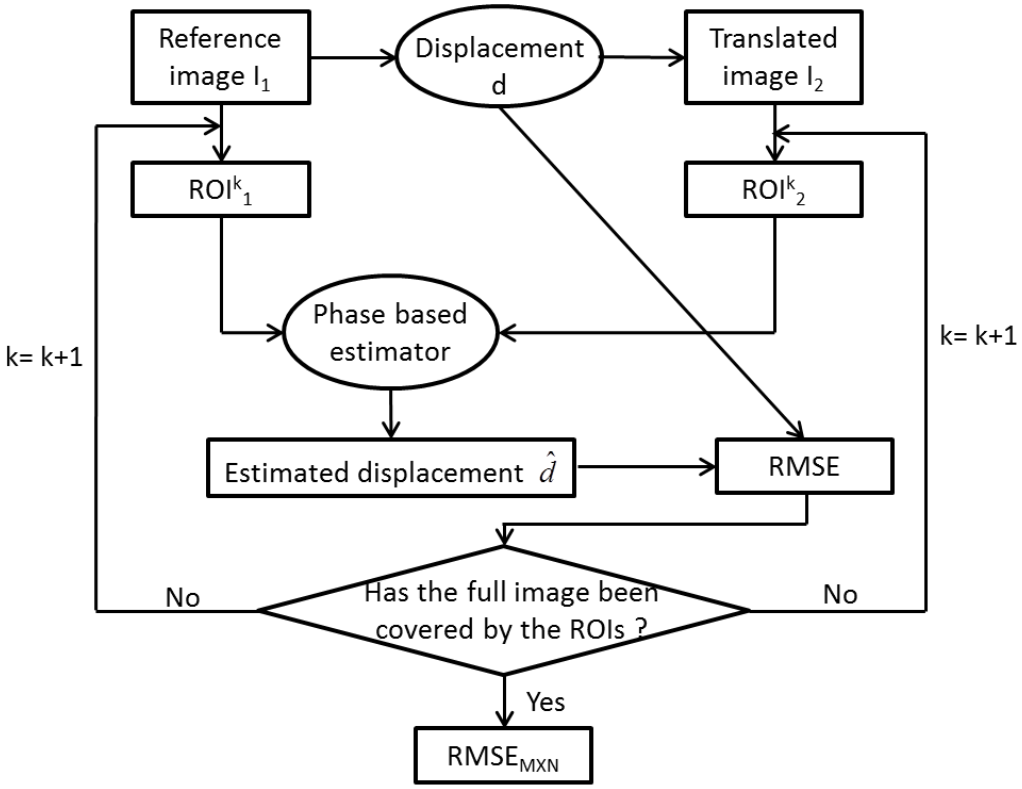

VF-Figure 7: Représentation de la procédure de caractérisation de l'estimation de mouvement

Les mouvements d'entrée sont purement axiaux, purement transverses ou diagonales. Ces mouvements sont appliqués à 100 fantômes isotropes différents, chacun d'entre eux contenant 10.000 diffuseurs situés en face de la sonde. Le fantôme couvre une profondeur allant de 60 à 100 mm. Pour un mouvement donné, on applique le déplacement à 100 fantômes différents obtenus en faisant varier les distributions de diffuseurs.

VF-Figure 8, VF-Figure 9 et VF-Figure 10 donnent les résultats de l'estimation de mouvement effectuée en des points situés à en face de la sonde (0°) à la profondeur de 80 mm.

Les résultats de la VF-Figure 9 montrent que les méthodes basées sur Fourier et sur la BP donnent une précision similaire pour l'estimation de mouvement purement axial. D'autre part, les résultats correspondant à un mouvement transversal pur donnés sur VF-Figure 8 (points situés à proximité d'un axe horizontal) indiquent que la formation de voies par l'approche BP conduit à une amélioration par rapport à l'approche avec Fourier. Les résultats de la VF-Figure 10 associée au mouvement combiné (points

situés sur la diagonale de la région) montrent une situation intermédiaire où l'approche BP est globalement plus performante que Fourier, mais l'amélioration observée n'est pas aussi grande que pour le mouvement purement transverse. Il peut également être observé que la précision diminue à mesure que l'amplitude de mouvement augmente, en particulier lorsque les déplacements sont plus grands que la demi longueur d'onde. Il existe alors des différences significatives entre les mouvements réels et estimés.

Les figures VF-Figure 11, VF-Figure 12 et VF-Figure 13 donnent les résultats de l'estimation de mouvement effectuée sur le côté de l'image (30°) à la profondeur de 80 mm.

Les résultats obtenus sur le côté de la sonde (VF-Figure 12) sont similaires aux résultats précédents pour un mouvement purement axial dans la VF-Figure 9: la formation de voie par BP améliore légèrement la précision de mouvement estimé par rapport à la formation de voie par Fourier. En ce qui concerne le mouvement transverse dans la VF-Figure 11, la formation de voie par BP améliore encore la précision, mais pas autant que dans la VF-Figure 8. Là encore, les résultats associés au mouvement en diagonal correspondent à une situation intermédiaire où la rétro-propagation est plus performante que Fourier dans la VF-Figure 13. Conformément à la conclusion des figures VF-Figure 8, VF-Figure 9 et VF-Figure 10, le mouvement estimé dévie beaucoup quand le déplacement réel est plus grand que la moitié de la longueur d'onde du signal (8° pour une longueur d'onde latérale et 0.73mm pour une longueur d'onde axiale), confirmant ainsi la limitation de notre méthode à des mouvements inférieurs à la demi-longueur d'onde du signal.

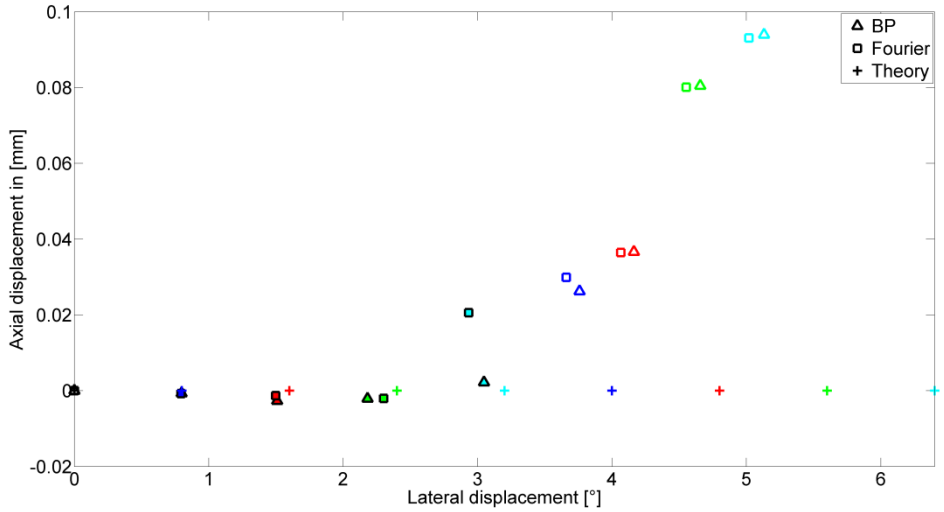

VF-Figure 8: Estimation des déplacements latéraux. Le déplacement a été estimé en utilisant soit l'approche de Fourier (carré) soit l'approche de BP (triangle). Les résultats sont comparés au mouvement réel (croix). L'estimation de mouvement a été effectuée en des points situés à l'avant ($\theta = 0°$) de la sonde à une profondeur de 80 mm. La valeur de la demi-longueur d'onde latérale est de 4 °.

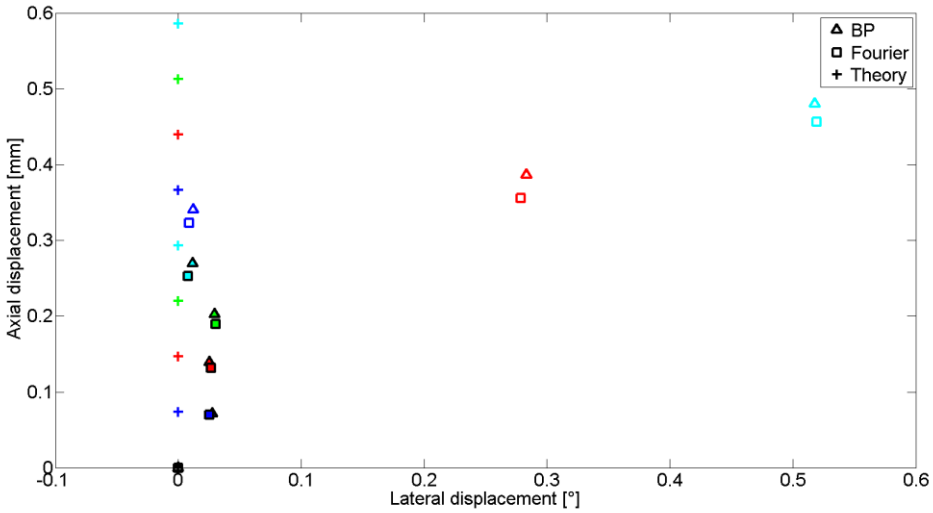

VF-Figure 9: Estimation des déplacements axiaux. Le déplacement a été estimé en utilisant soit l'approche de Fourier (carré) soit l'approche de BP (triangle). Les résultats sont comparés au mouvement réel (croix). L'estimation de mouvement a été effectuée en des points situés à l'avant ($\theta = 0°$) de la sonde à une profondeur de 80 mm. La valeur de la demi-longueur d'onde axiale est de 0.36 mm.

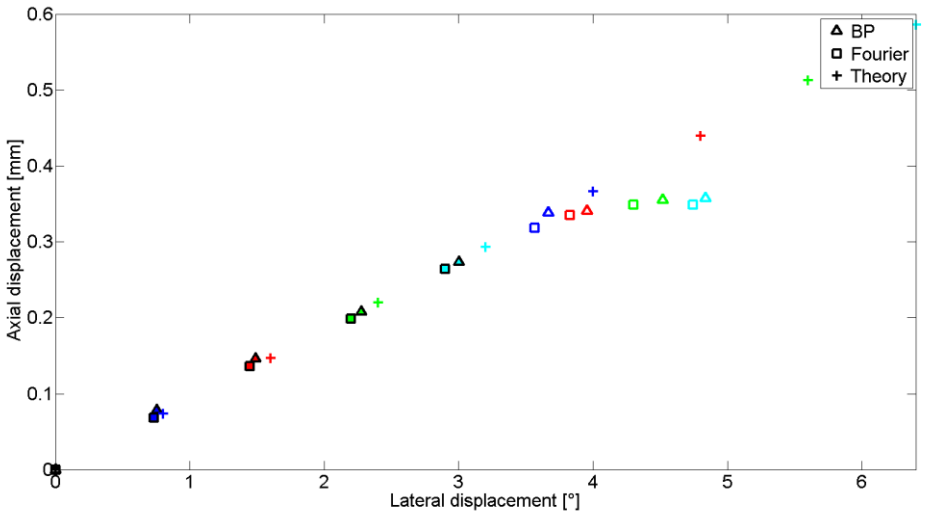

VF-Figure 10: Estimation des déplacements diagonaux. Le déplacement a été estimé en utilisant soit l'approche de Fourier (carré) soit l'approche de BP (triangle bleu). Les résultats sont comparés au mouvement réel (croix). L'estimation de mouvement a été effectuée en des points situés à l'avant ($\theta = 0°$) de la sonde à une profondeur de 80 mm.. La valeur de la demi-longueur d'onde latérale est de 4° et de 0.36 mm pour la moitié de la longueur d'onde axiale.

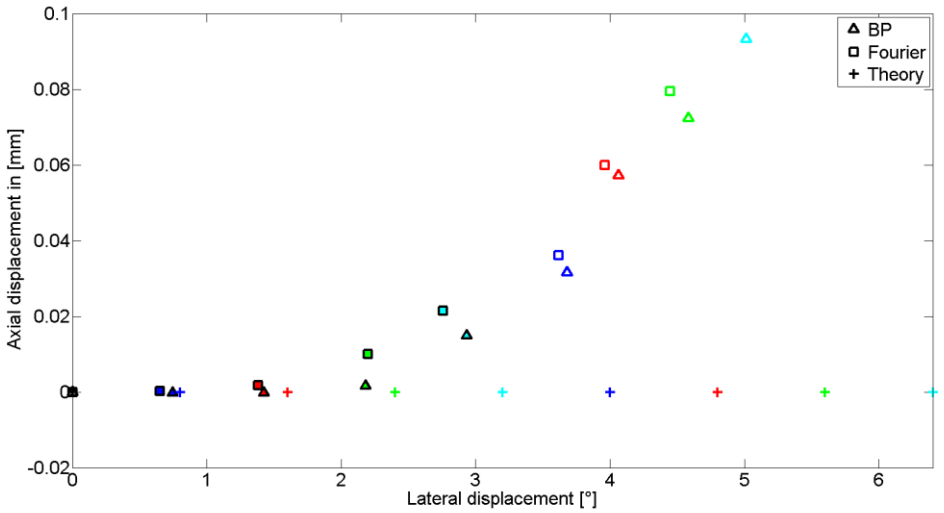

VF-Figure 11: Estimation des déplacements latéraux. Le déplacement a été estimé en utilisant soit l'approche de Fourier (carré) soit l'approche de BP (triangle). Les résultats sont comparés au mouvement réel (croix). L'estimation de mouvement a été effectuée en des points situés à l'avant ($\theta = 30°$) de la sonde à une profondeur de 80 mm. La valeur de la demi-longueur d'onde latérale est de 4 °.

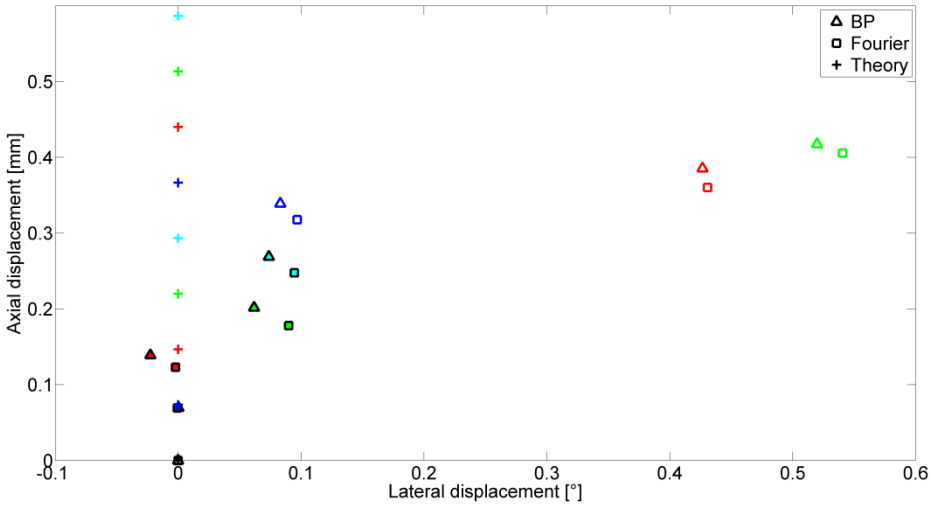

VF-Figure 12: Estimation des déplacements axiaux. Le déplacement a été estimé en utilisant soit l'approche de Fourier (carré) soit l'approche de BP (triangle). Les résultats sont comparés au mouvement réel (croix). L'estimation de mouvement a été effectuée en des points situés à l'avant ($\theta = 30°$) de la sonde à une profondeur de 80 mm. La valeur de la demi-longueur d'onde axiale est de 0.36 mm.

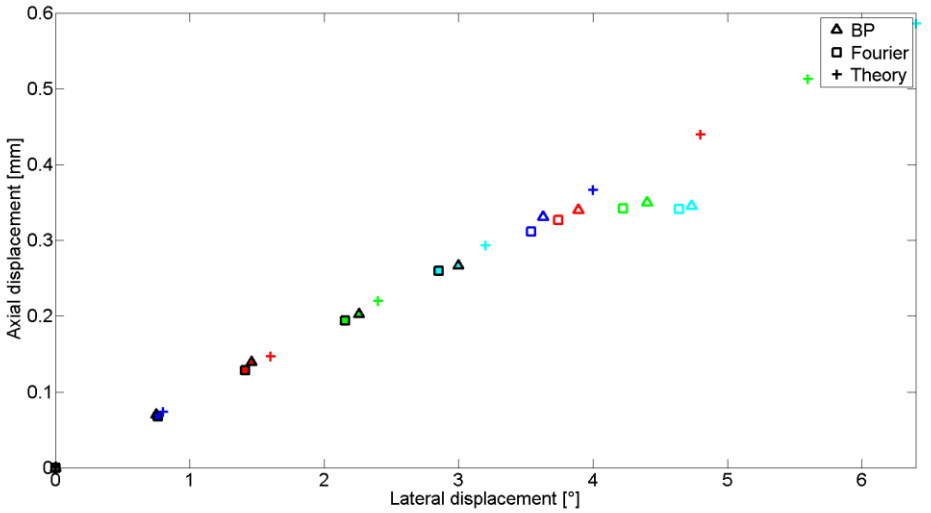

VF-Figure 13: Estimation des déplacements diagonaux. Le déplacement a été estimé en utilisant soit l'approche de Fourier (carré) soit l'approche de BP (triangle bleu). Les résultats sont comparés au mouvement réel (croix). L'estimation de mouvement a été effectuée en des points situés à l'avant ($\theta = 30°$) de la sonde à une profondeur de 80 mm.. La valeur de la demi-longueur d'onde latérale est de 4° et de 0.36 mm pour la moitié de la longueur d'onde axiale.

B. Distribution spatiale de l'erreur de mouvement

La distribution spatiale de l'erreur d'estimation de mouvement, mesurée en RMSE entre les estimations et le mouvement réel est représentée pour une région de balayage

sectoriel correspondant à une profondeur allant de 60 à 100 mm et un angle compris entre -30 ° à 30 ° dans les figures VF-Figure 14, VF-Figure 15 et VF-Figure 16.

VF-Figure 14 présente les résultats obtenus dans le cas d'un mouvement transverse de 0.8°. VF-Figure 14 (a) montre que l'erreur quadratique moyenne associée à la méthode de Fourier est relativement stable le long de la direction de propagation et augmente avec l'angle de balayage pour atteindre un maximum dans les régions latérales de l'image. D'autre part, le RMSE associé à la rétro-propagation est assez stable. En outre, le RMSE obtenu avec l'approche BP est plus petit que celui obtenu par la méthode de Fourier, sauf autour de la direction correspondant à l'axe de la sonde ($\theta = 0°$), où les deux RMSE sont proches. Le RMSE associé à la transformée de Fourier est de 0.07° et 0.05 pour la rétro-propagation. Ces résultats montrent que la rétro-propagation contribue en moyenne à une amélioration de 32,8 % par rapport à la transformée de Fourier.

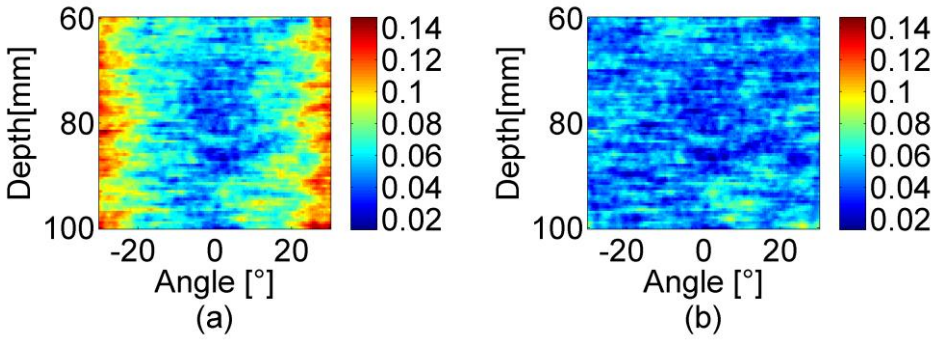

VF-Figure 14: Représentation spatiale de la précision de l'estimation de mouvement évaluée par le RMSE pour un mouvement latéral de 0.8° obtenu pour des diffuseurs situés à des profondeurs entre 60mm et 100mm sur un secteur allant de -30° à +30°, en utilisant des images obtenues par la formation de voie basé sur la transformée de Fourier (a) et la rétro-propagation dans (b), l'erreur quadratique moyenne est présentée en [°] .

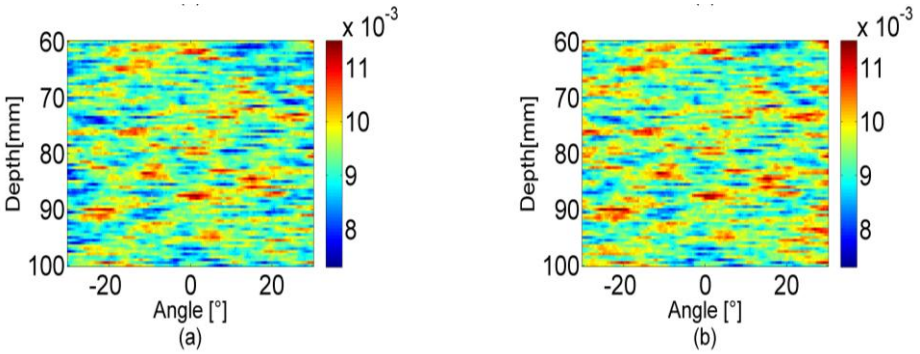

VF-Figure 15: Représentation spatiale de la précision de l'estimation de mouvement évalué par le RMSE pour un mouvement axial de 0.07 mm obtenu pour des diffuseurs situés à des profondeurs entre 60 mm et 100 mm sur un

secteur allant de -30° à +30°, en utilisant des images obtenues par la formation de voie basé sur la transformée de Fourier (a) et la rétro-propagation dans (b), l'erreur quadratique moyenne est présentée en [mm].

VF-Figure 15 présente les résultats obtenus dans le cas d'un mouvement axial de 0.07 mm. Contrairement aux résultats obtenus pour le mouvement transverse, on peut observer que les deux méthodes de formation de voie donnent de très proches RMSE. Les valeurs moyennes de RMSE sont de 9.4 x 10^{-3} mm et 9.3 × 10^{-3} mm pour la formation de voie à base de Fourier et de rétro-propagation,

VF-Figure 16 présente les résultats obtenus dans le cas d'un déplacement diagonal. VF-Figure 16 (a, b) représente l'amplitude du RMSE transverse à l'aide d'images formés à partir de l'approche de Fourier et l'approche par rétro-propagation, respectivement. VF-Figure 16 (c, d) représentent les RMSE axiaux correspondants. Ces résultats donnent les mêmes conclusions que dans la VF-Figure 14 et VF-Figure 15. En effet, VF-Figure 16 (a, b) montrent que les RMSE transverses augmentent avec l'angle de balayage pour l'approche avec la transformée de Fourier, alors que le RMSE associé à la rétro-propagation est plus stable et plus petit. En ce qui concerne le RMSE axial, VF-Figure 16 (c, d) indique que les deux méthodes donnent des valeurs de précision très proches. Les RMSE transversaux moyens sont de 0.11° et 0.08° pour la formation de voie à base de Fourier et pour la rétro-propagation, respectivement ; ainsi la rétro-propagation contribue à une amélioration moyenne de 28 % par rapport à Fourier.

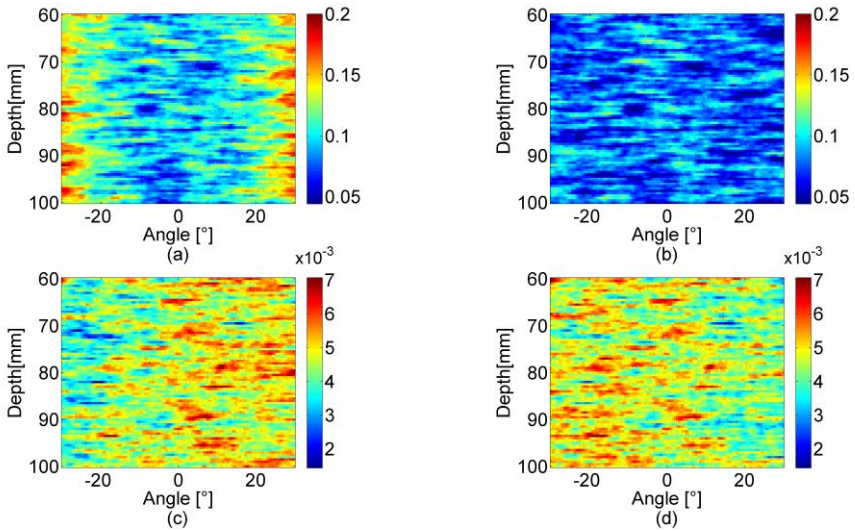

VF-Figure 16: : Représentation spatiale de la précision de l'estimation de mouvement évalué par le RMSE pour un mouvement latéral de 0.8° et axial de 0.07 mm obtenu pour des diffuseurs situés à des profondeurs entre 60 mm et 100 mm sur un secteur allant de -30° à +30°, en utilisant des images obtenues par la formation de voie basées sur la transformée de Fourier (a) et la rétro-propagation dans (b), l'erreur quadratique moyenne est présentée en [°], (c) est obtenue par la formation de voie basé sur la transformée de Fourier et la rétro-propagation dans (d), l'erreur quadratique moyenne est présentée en [mm]

Mouvement cardiaque simulé

Finalement, les performances du formateur de voie proposé sont également étudiées dans le cas d'un mouvement cardiaque réaliste simulé. Le mouvement cardiaque est créé en prenant une acquisition d'échographie cardiaque réelle comme modèle. Les simulations ainsi obtenues sont visuellement indiscernable des acquisitions réelles. Comme les séquences simulées intègrent un mouvement connu, elles peuvent être utilisées comme référence pour évaluer la méthode proposée.

VF-Figure 17 illustre les valeurs d'erreur moyenne pour chaque image de la séquence de synthèse pour l'erreur latérale en [°] (a) et de l'erreur axiale en [mm] (b). On peut observer que dans la figure (a) l'erreur latérale de BP est inférieure à celle de Fourier tandis que dans la figure (b) les deux méthodes donnent les mêmes résultats pour l'erreur axiale. VF-Figure 18 présente les écarts-types correspondants. Cette figure montre que la BP présente des écart-type inférieurs pour les erreurs latérales et similaires pour les erreurs axiales.

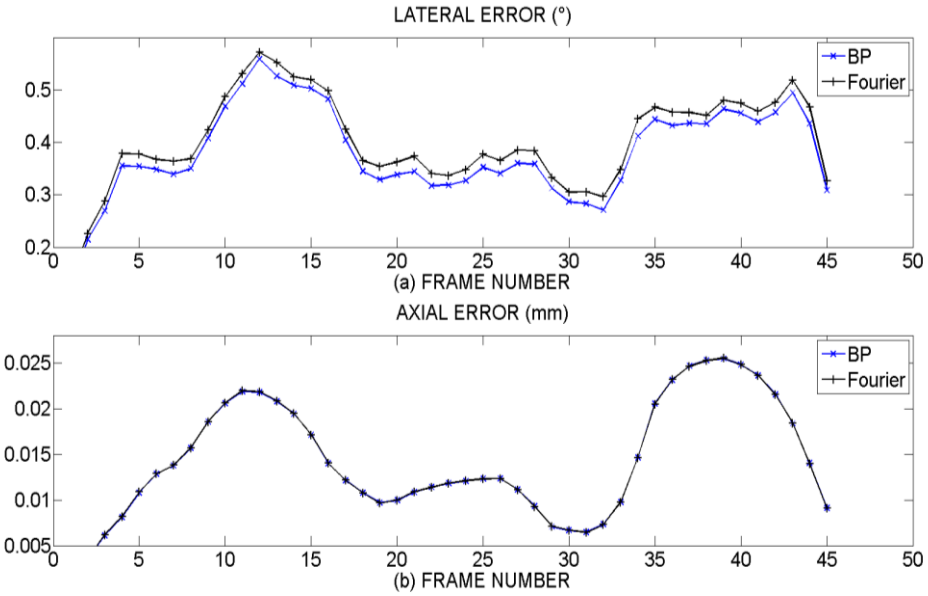

VF-Figure 17: Erreurs au cours de la séquence réaliste simulée. (a) et (b) illustrent les valeurs moyennes pour chaque image de la séquence de synthèse pour l'erreur latérale en [°] et l'erreur axiale en [mm], respectivement. La ligne de croix bleues correspond aux résultats par formation de voie à base de BP, et la ligne de + noirs par formation de voie par Fourier.

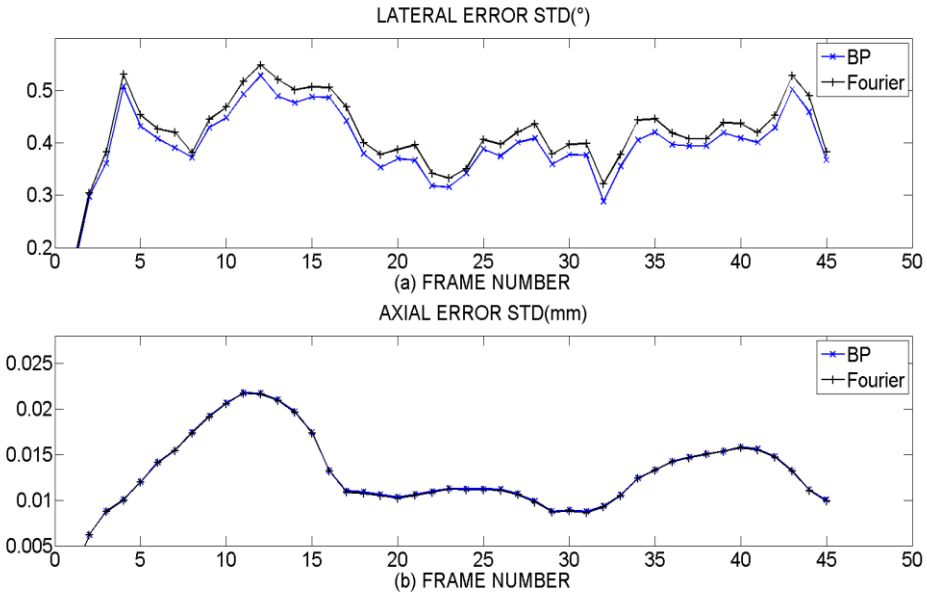

VF-Figure 18: Ecarts-types d'erreurs au cours de la séquence réaliste simulée dans la VF-Figure 18. (a) et (b) illustrent les valeurs moyennes pour chaque image de la séquence de synthèse pour les écarts-types dans la direction latérale en [°] et les écarts-types pour la direction axiale en [mm], respectivement. La ligne de croix bleues correspond aux résultats par formation de voie par BP, et la ligne de + noirs par formation par Fourier.

Dans VF-Figure 17 et VF-Figure 18 les images de 10 à 18 correspondent à l'expansion diastolique, celles 19 à 31 sont à la fin de la diastole et les images 32 à 45 correspondent à la contraction systolique. A titre d'exemple les résultats de l'estimation au cours de la contraction systolique et de l'extension diastolique sont présentés dans la VF-Figure 19. Ces résultats montrent que les déplacements estimés sont qualitativement en accord avec le mouvement physiologique prévu sur un cœur en bonne santé dans les deux phases du cycle cardiaque.

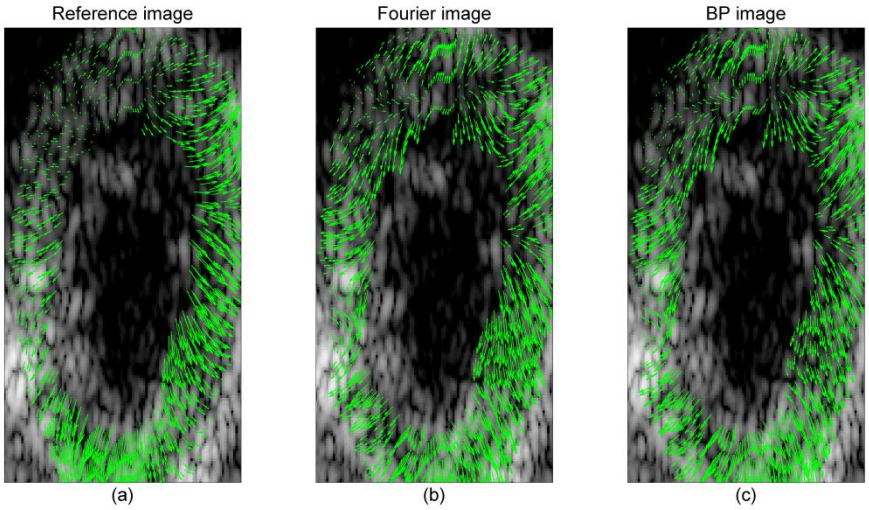

VF-Figure 19: Exemple de champs de mouvement estimés sur une phase diastolique de la séquence étudiée, (a) présente le mouvement de référence, (b) et (c) le mouvement estimée à l'aide de la méthode de Fourier et de rétro-propagation.

Résultats expérimentaux

Afin d'évaluer la méthode sur des données réelles, nous avons effectué une étude expérimentale simple. Elle a consisté à acquérir des données à partir d'un fil afin d'évaluer la PSF expérimentale. Le formateur de voie avec OT basé sur la BP a été comparé à la technique à base de Fourier. Les expériences ont été réalisées en utilisant l'échographe de recherche ULA-OP [54], dans lequel nous avons implanté le formateur de voies proposé. Le fil a été imagé à 0° et 30°. Ceci a été répété 100 fois afin de mesurer l'erreur quadratique moyenne de la même manière que dans les simulations.

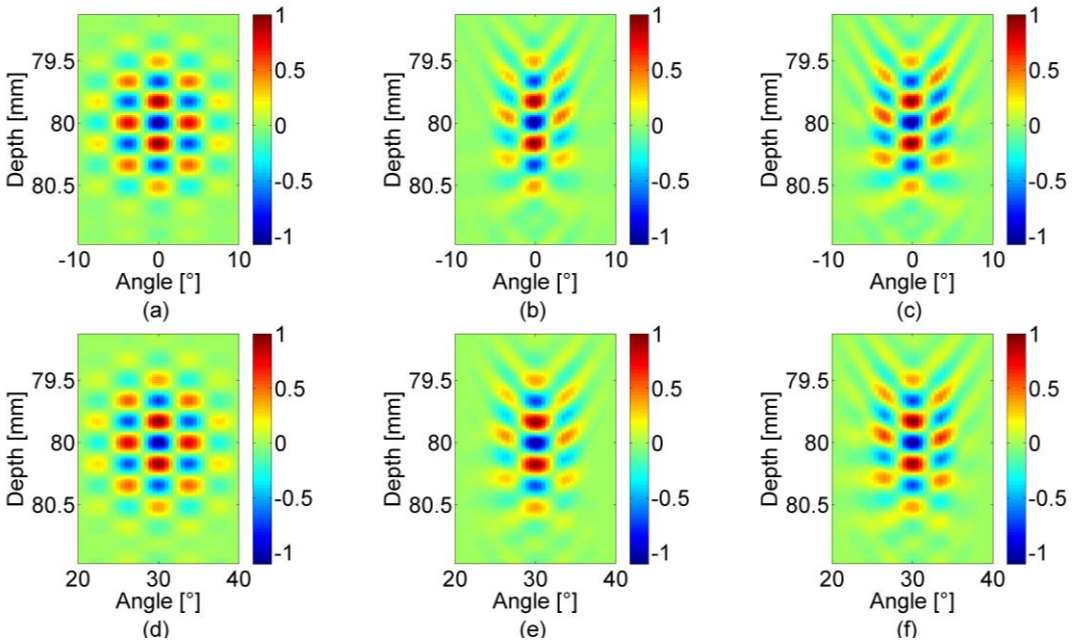

VF-Figure 20: Présentation de la PSF théorique à l'avant (0°) de la sonde en (a) et PSF expérimentale correspondante obtenu par Fourier en (b) et par rétro-propagation en (c); (d) PSF théorique sur le côté (30°) de la sonde et PSF expérimentale correspondante obtenue par Fourier en (e) et par rétro-propagation en (f).

VF-Figure 20 (a, d) présente les PSFs théoriques pour des diffuseurs situés à l'avant (0°) à (a) et sur le côté (30°) à (d) de la sonde. Les deux diffuseurs sont situés à une profondeur de 80mm.

VF-Figure 20 (b, c) représente la PSF obtenue à l'avant de la sonde en utilisant une formation de voie par Fourier (b) et par BP (c), respectivement. Les RMSE associés sont de 0,0734 pour la BP et 0,0783 pour Fourier, respectivement: les deux donnent donc des résultats très proches. VF-Figure 20 (e, f) correspond à une erreur quadratique moyenne de 0,0727 pour Fourier et 0,0675 pour la BP, montrant que la formation de voie par BP améliore la PSF de 7,15 % par rapport à la formation de voie par Fourier. VF-Figure 20 (e, f) montre en particulier que cette amélioration correspond principalement aux lobes latéraux de la PSF, qui sont mieux définis dans le cas de la formation de voie par BP.

Le PSF obtenue dans un cadre expérimental réel confirme donc que la mise en œuvre du formateur de voie proposé obtenu par rétro-propagation est techniquement faisable. Les résultats valident en outre que la formation de voie à base de BP donne une PSF plus précise que la formation de par Fourier sur le côté de la sonde. Ces premiers résultats seront confirmés à l'avenir par des études expérimentales plus approfondies y compris par des évaluations de précision en termes d'estimation de mouvement.

2. Décomposition en ondes planes

La théorie de la décomposition en ondes planes est utilisée pour décomposer un champ acoustique en un ensemble d'ondes planes. Les ondes planes sont des ondes individuelles qui se propagent dans différentes directions. En rétro-propageant l'ensemble des ondes planes obtenues suite à la décomposition du champ et en sommant tous les signaux ainsi reçus au niveau de la sonde, nous pouvons obtenir les signaux d'excitation pour chaque transducteur. En utilisant la matrice d'excitation en tant que signaux émis, on peut obtenir en théorie la même PSF que celle décomposée et retro-propagée. Il faut souligner que le champ de pressions ou la PSF doivent être symétrique par rapport à l'axe de propagation [55, 56].

1) Décomposition en ondes planes en géométrie linéaire

Compte tenu du caractère 2D du problème traité, la ligne d'intégrale servant pour la décomposition est la ligne d'intersection entre un plan de coupe et le faisceau émis. VF-Figure 21 représente le faisceau émis et coupé par un plan suivant l'angle θ. L'intégrale suivant cette direction porte donc l'indice θ.

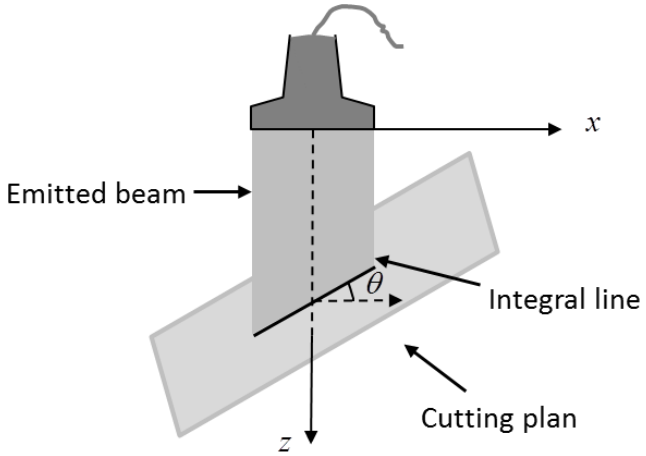

VF-Figure 21: Schéma représentant une ligne d'intégrale pour la décomposition en ondes planes

VF-Figure 22 (a) présentent la PSF avec des oscillations transverses et la décomposition en ondes planes correspondante dans la VF-Figure 22 (b).

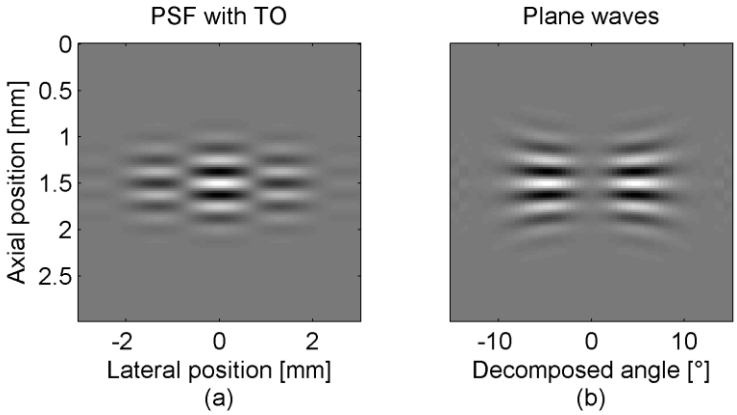

VF-Figure 22: Présentation de la PSF avec des oscillations transverses (a) et la décomposition en ondes planes correspondante en (b). La fréquence centrale est de $f_0 = 6MHz$, la longueur d'onde latérale est de 3 mm, et l'angle décomposé est de -15 ° à 15 °.

La comparaison des RMSE obtenus en utilisant l'approche de Fourier et la stratégie de la décomposition en ondes planes est présentée sur la VF-Figure 23. Le résultat est obtenu pour une PSF située latéralement entre -5 mm et 5 mm et à des profondeurs de 10 mm à 50 mm. Le RMSE pour les deux méthodes change peu horizontalement mais augmente très clairement en fonction de la profondeur, ce qui indique que la qualité de la PSF est largement affaiblie avec la profondeur mais peu influencée par la position latérale en géométrie linéaire. En outre, il est évident de voir l'amélioration par rapport à l'approche de Fourier apportée par la stratégie de décomposition ondes planes sur la VF-Figure 23 (b).

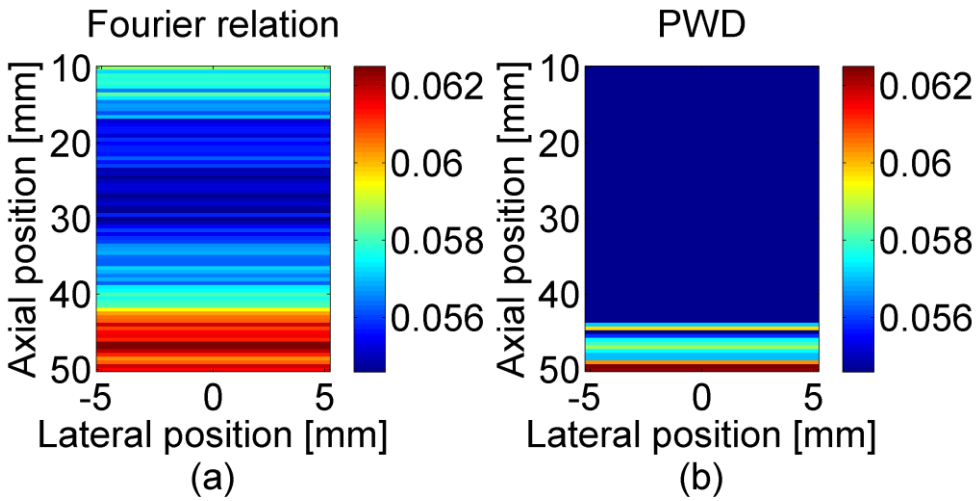

VF-Figure 23: Présentation des RMSE de la PSF pours ll'approche de Fourier en (a) et la stratégie de décomposition-rétro-propagation dans (b).

2) Décomposition en ondes plane en géométrie sectorielle

La bonne performance de la décomposition en ondes planes en géométrie linéaire nous a poussés à l'adapter en balayage sectoriel visant à obtenir une PSF de bonne qualité également dans cette géométrie. Toutes les simulations ont été effectuées en utilisant les paramètres donnés dans le tableau 3. La PSF en coordonnées polaires est présentée dans la VF-Figure 24.

Tableau 1: Paramètres de simulation

f_0	$3.5MHz$
f_s	$50MHz$
λ_θ^{PSF}	8°
σ_θ^{PSF}	12°
c	1540
Kerf	0.2 mm
Largeur	0.14 mm
Nombre des éléments	64

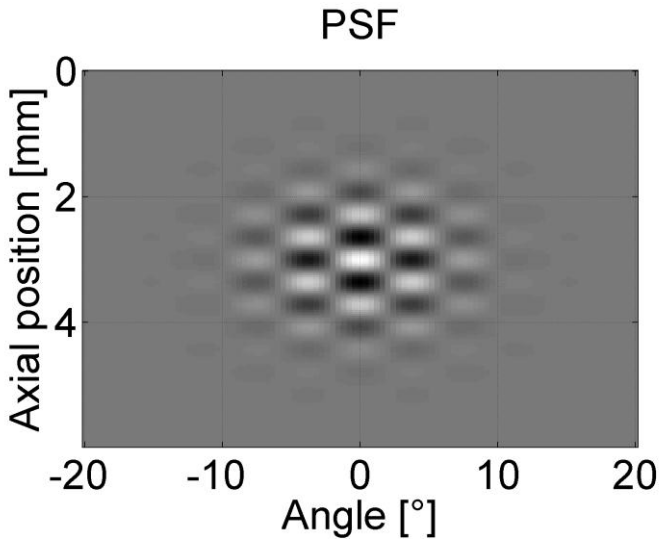

VF-Figure 24: Présentation de la PSF. La longueur d'onde latérale $\lambda_\theta^{PSF} = 8°$, $\sigma_\theta^{PSF} = 12°$, la fréquence centrale $f_0 = 3.5MHz$.

En tenant compte des caractéristiques de balayage sectoriel, la décomposition de PSF est effectuée après conversion de la PSF des coordonnées polaires en coordonnées cartésiennes comme présenté dans la VF-Figure 25(a). La décomposition en ondes planes est présentée dans la VF-Figure 25(b).

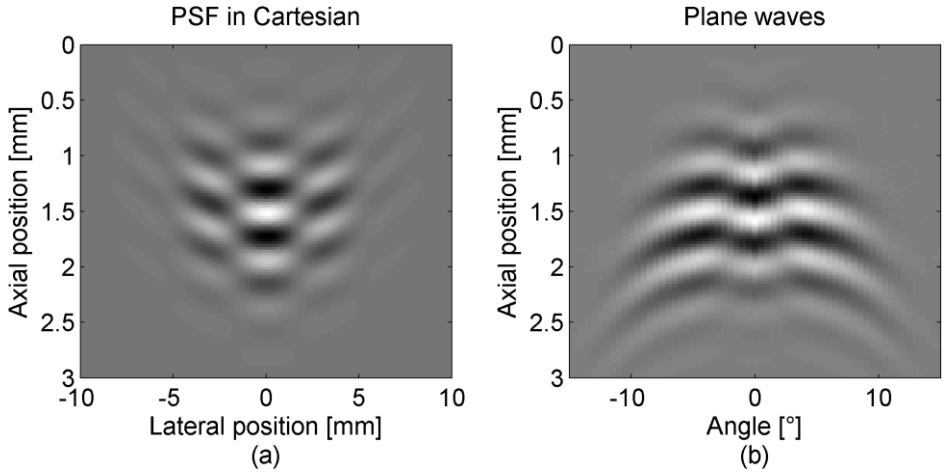

VF-Figure 25: Présentation de la PSF en coordonnées cartésiennes (a) et les ondes planes décomposées (b).

Comme présenté pour la géométrie linéaire, les ondes planes décomposées sont rétro-propagées à la sonde, puis sommées pour chaque élément. On utilise alors comme signaux d'excitation les signaux ainsi obtenus. Afin d'évaluer la faisabilité de cette technique la qualité des PSF obtenues est comparée avec celle obtenue par la méthode de Fourier.

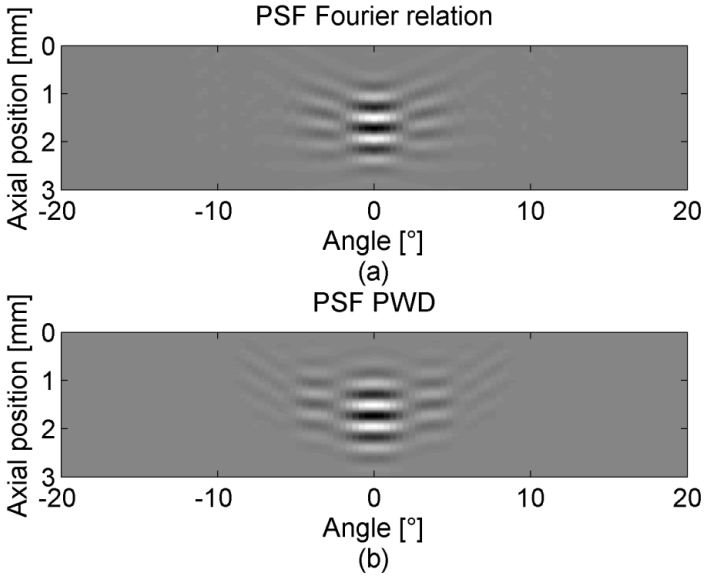

VF-Figure 26: Présentation de la PSF en face de la sonde (0 °) obtenue en utilisant la transformée de Fourier (a) et la théorie de décomposition en ondes planes (b)

La comparaison de la qualité de la PSF est donnée dans VF-Figure 26 et VF-Figure 27. VF-Figure 26 montre la PSF acquise en face de la sonde (0 °) en utilisant la relation de Fourier (a) et la théorie PWD (b). Le RMSE pour la PSF en face de la sonde est de 0.07 avec la transformée de Fourier et de 0.04 pour la PWD. En outre, le

RMSE pour la PSF obtenue sur le côté de la sonde (10°) VF-Figure 27, est de 0.08 pour la transformée de Fourier est de 0.08 et de 0.05 pour la PWD. Ainsi, les résultats quantifiés indiquent qu'il est possible d'adapter la théorie PWD en géométrie sectorielle et il peut donner une meilleure PSF que celle obtenue en utilisant la méthode de la transformée de Fourier classique.

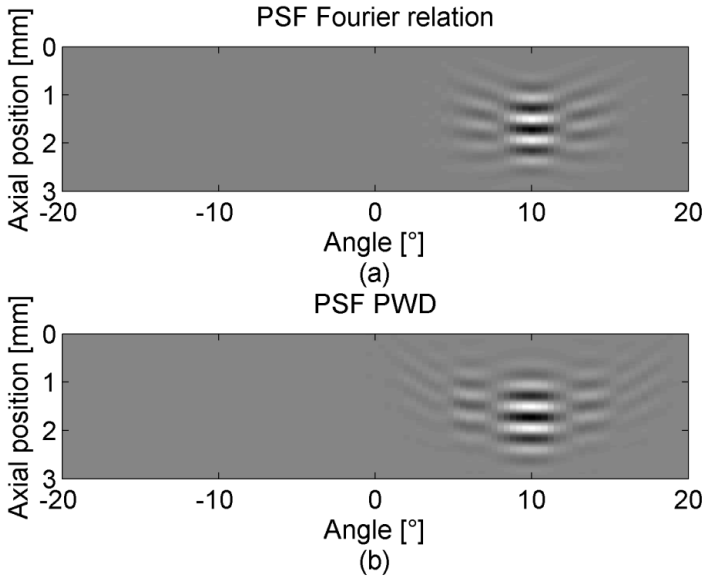

VF-Figure 27: Présentation de PSF sur le côté de la sonde (10°) obtenue en utilisant la transformée de Fourier (a) et la théorie de décomposition en ondes planes (b)

IV. Conclusion

Cette thèse présente tout d'abord la limitation de la méthodologie conventionnelle de conception des formateurs de voie en imagerie ultrasonore médicale et souligne la faible résolution dans la direction latérale obtenue avec cette approche. La résolution de ce problème est de mettre en œuvre une technique d'imagerie particulière qui consiste à introduire dans les images des oscillations transverses, c'est-à-dire dans la direction perpendiculaire aux ultrasons. La contribution de cette thèse est de proposer un nouveau formateur de voie basé sur des méthodes de rétro-propagation afin d'améliorer la qualité des PSF pour les OT par rapport aux formateurs de voies classiques obtenus avec l'approche dite de Fourier.

La méthode de rétro-propagation s'appuie sur deux principes physiques: la propagation des ondes et le théorème de réciprocité. Avec l'approche proposée la formation de voie avec des oscillations transverses est améliorée et des PSF plus proches de celles escomptées qu'avec l'approche de Fourier ont pu être obtenues en balayage sectoriel. L'étude de la variation de fonction de pondération en fonction des

angles est présentée pour les deux méthodes. L'évaluation de l'amélioration est donnée par le calcul du RMSE. La variation spatiale de la qualité de la PSF de même que l'influence des paramètres sont étudiés. L'approche par rétro-propagation conduit à des PSF plus proches de la théorie (et donc avec un RMSE plus faible) que l'approche classique de Fourier. Enfin l'intérêt de l'approche proposée est également montrée pour l'estimation de mouvement, à la fois pour les déplacements simples et dans le cas d'une simulation réaliste du mouvement cardiaque. Les résultats quantitatifs confirment que la méthode de rétro-propagation proposée est mieux adaptée pour le suivi du mouvement que l'approche de Fourier. Enfin des résultats expérimentaux ont permis de montrer la faisabilité pratique de mettre en œuvre sur échographe de recherche le formateur de voies proposé.

La décomposition en ondes planes, la théorie de rétro-propagation et la stratégie de transmission en géométrie linéaire ont été vérifiées en simulations numériques. Compte tenu de la bonne performance en géométrie linéaire, la contribution de les adapter à la géométrie sectorielle a été proposée. La méthode proposée permet d'obtenir une meilleure PSF que la méthode de Fourier. Cette partie devra encore être approfondie afin de valider la stabilité de l'approche lorsque les paramètres varient et lorsque l'on passe au cas in vivo.

Publications

Journal articles

1. **X. Guo**, H. Liebgott, and D. Friboulet, "Back-propagation beamformer design for motion estimation in echocardiography", *Ultrasonic Imaging*, **accepted**, *2014.*
2. M. Alessandrini, A. Basarab, L. Boussel, **X. Guo**, A. Serusclat, D. Friboulet, D. Kouame, O. Bernard, and H. Liebgott, A New Technique for the Estimation of Cardiac Motion in Echocardiography Based on Transverse Oscillations: a preliminary evaluation in silico and a feasibility demonstration in vivo, Medical Imaging, IEEE Transactions on, PP. 99, 1-1, 2014..

Conference papers

1. **X. Guo**, D. Friboulet, and H. Liebgott, "Transverse oscillations beamformer design for sector scan using back-propagation", *IEEE International Symposium on Biomedical Imaging (ISBI)*, Barcelona, Spain, pp. 1100-1103, 2012.
2. **X. Guo**, D. Friboulet, and H. Liebgott, "Back-propagation based beamformer design for Transverse Oscillations in Echocardiography", *Acoustics 2012*, Nantes, France, pp. 1100-1103, 2012.

Appendix: Practical implementation on an ultrasound scanner

The practical implementation on an ultrasound scanner is included in a framework for cardiac motion estimation based on transverse oscillations[28], it is done for verifying the feasibility of an in vivo evaluation on real clinical recording.

This has been done with two modes, the conventional B-mode and the mode with transverse oscillations. The proposed image formation technique with transverse oscillations is based on Fourier relation as given in equations(3.4)(3.5). The experiments were conducted by using the ultrasound research platform named ULA-Op [64], in which we have imported the proposed apodization as presented in equation(3.5), the basic parameter setting are given in equations (3.6) and (3.7). A cardiac phased array probe PA230 from Esaote is used as the data recording scanner. In order to make the conventional B-mode and the proposed TO beamforming be comparable, they are imported in the same interface, and the acquisition of two imaging modalities is interleaved, by which means the scanning beams for two modes is done one after another. The center frequency of ultrasound signal is 2.1MHz and the sampling frequency is 50MHz. Limited to the memory capacity, the scanning sector is from -32° to 32° and the beam density is of 1 beam/degree. The apodization function is shown in Fig.A-1. As to close to the real echocardiography scanning machine the frame rate is set as 25 frames/s, a total recordation during 2 seconds with 49 frames for each mode is acquired.

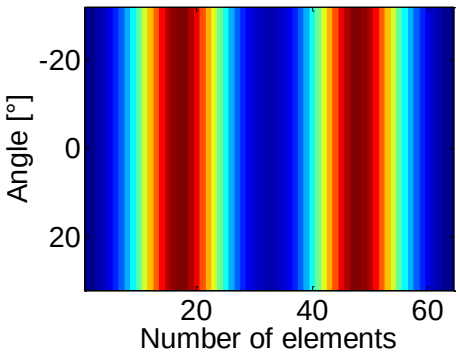

Fig.A-1: Presentation of apodization function implanted into the ULA-Op.

The acquisition is performed by an experienced radiologist on a healthy male volunteer aged 25 years old. Fig.A-2 shows one frame of the heart septum on the short axis obtained using B-mode without TO in (a) and using Fourier relation with TO in

(b). And in another aspect, the apical four chamber view with and without TO is presented in Fig.A-3. By comparing the images, the speckles with TOs are with higher lateral resolution as expected.

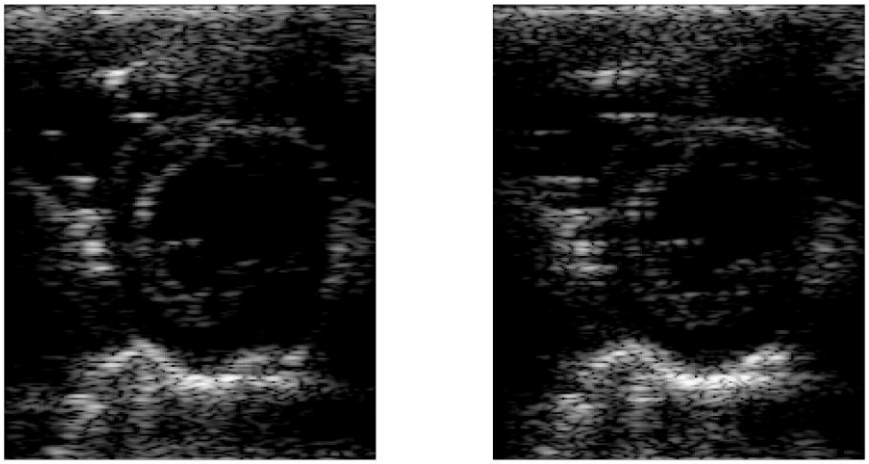

Fig.A-2: Presentation of one frame on the short axis, (a) is obtained under B-Mode, and (b) is obtained using the Fourier relation.

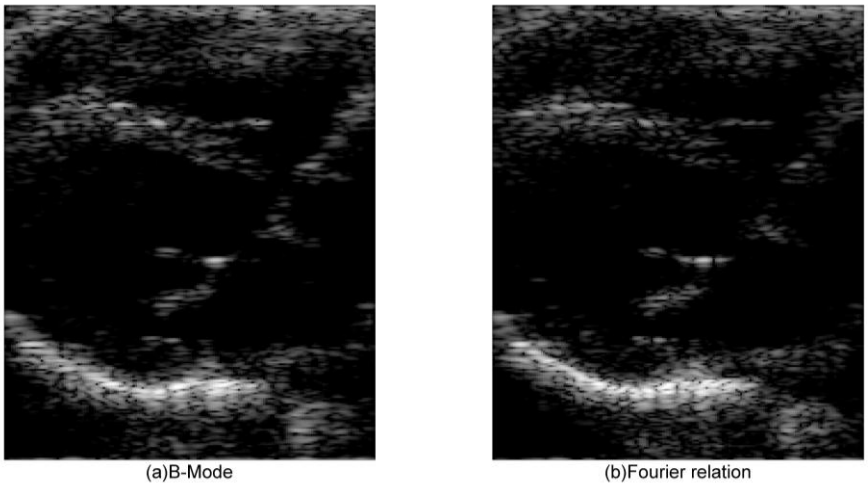

Fig.A-3: Presentation of one frame of apical 4 chamber obtained under B-Mode in (a) and under Fourier relation in (b).

References

[1] J. Kisslo, B. Firek, T. Ota, D. H. Kang, C. E. Fleishman, G. Stetten, J. Li, C. J. Ohazama, D. Adams, and C. Landolfo,Real‐Time Volumetric Echocardiography, Echocardiography, 17. 8, 773-779, 2007.

[2] B. Touil, A. Basarab, P. Delachartre, O. Bernard, and D. Friboulet,Analysis of motion tracking in echocardiographic image sequences: Influence of system geometry and point-spread function, Ultrasonics, 50. 3, 373-386, 2010.

[3] J. A. Jensen, *Estimation of blood velocities using ultrasound: A signal processing approach*: Cambridge University Press, 1996.

[4] A. Marion, W. Aoudi, A. Basarab, P. Delachartre, and D. Vray,Blood flow evaluation in high-frequency, 40MHz imaging: A comparative study of four vector velocity estimation methods, Ultrasonics, 50. 7, 683-690, 2010.

[5] J. F. Deprez, E. Brusseau, J. Fromageau, G. Cloutier, and O. Basset,On the potential of ultrasound elastography for pressure ulcer early detection, Medical Physics, 38. 4, 1943, 2011.

[6] J. Ophir, I. Cespedes, H. Ponnekanti, Y. Yazdi, and X. Li,Elastography: a quantitative method for imaging the elasticity of biological tissues, Ultrasonic imaging, 13. 2, 111-134, 1991.

[7] C. Sumi,Fine elasticity imaging utilizing the iterative RF-echo phase matching method, Ultrasonics, Ferroelectrics and Frequency Control, IEEE Transactions on, 46. 1, 158-166, 1999.

[8] W. L. Nyborg,Biological effects of ultrasound: development of safety guidelines. Part II: general review, Ultrasound in medicine & biology, 27. 3, 301-333, 2001.

[9] D. Vray, E. Brusseau, V. Detti, F. Varray, A. Basarab, O. Beuf, O. Basset, C. Cachard, H. Liebgott, and P. Delachartre, "Ultrasound Medical Imaging," in *Medical Imaging Based on Magnetic Fields and Ultrasounds*, ed: John Wiley & Sons, Inc., 2014, pp. 1-72.

[10] E. Nagel, H. B. Lehmkuhl, W. Bocksch, C. Klein, U. Vogel, E. Frantz, A. Ellmer, S. Dreysse, and E. Fleck,Noninvasive diagnosis of ischemia-induced wall motion abnormalities with the use of high-dose dobutamine stress MRI comparison with dobutamine stress echocardiography, Circulation, 99. 6, 763-770, 1999.

[11] B. Bijnens, P. Claus, F. Weidemann, J. Strotmann, and G. R. Sutherland,Investigating cardiac function using motion and deformation analysis in the setting of coronary artery disease, Circulation, 116. 21, 2453-2464, 2007.

[12] K. Kaluzynski, X. Chen, S. Y. Emelianov, A. R. Skovoroda, and M. O'Donnell,Strain rate imaging using two-dimensional speckle tracking, Ultrasonics, Ferroelectrics and Frequency Control, IEEE Transactions on, 48. 4, 1111-1123, 2001.

[13] E. Konofagou and J. Ophir,A new elastographic method for estimation and imaging of lateral displacements, lateral strains, corrected axial strains and Poisson's ratios in tissues, Ultrasound in medicine & biology, 24. 8, 1183-1199, 1998.

[14] J. D'hooge, E. Konofagou, F. Jamal, A. Heimdal, L. Barrios, B. Bijnens, J. Thoen, F. Van de Werf, G. Sutherland, and P. Suetens,Two-dimensional ultrasonic strain rate measurement of the human heart in vivo, Ultrasonics, Ferroelectrics and Frequency Control, IEEE Transactions on, 49. 2, 281-286, 2002.

[15] M. A. Lubinski, S. Y. Emelianov, K. Raghavan, A. E. Yagle, A. R. Skovoroda, and M. O'Donnell,Lateral displacement estimation using tissue incompressibility, IEEE Transactions on Ultrasonics Ferroelectrics and Frequency Control, 43. 2, 247-256, 1996.

[16] R. G. Lopata, M. M. Nillesen, H. H. Hansen, I. H. Gerrits, J. M. Thijssen, and C. L. De Korte,Performance evaluation of methods for two-dimensional displacement and strain estimation using ultrasound radio frequency data, Ultrasound in medicine & biology, 35. 5, 796-812, 2009.

[17] M. De Craene, S. Marchesseau, B. Heyde, H. Gao, M. Alessandrini, O. Bernard, G. Piella, A. Porras, L. Tautz, and A. Hennemuth,3D strain assessment in ultrasound (straus): A synthetic comparison of five tracking methodologies, Medical Imaging, IEEE Transactions on, 32. 9, 1632-1646, 2013.

[18] M. E. Aderson,Multi-dimensional velocity estimation with ultrasound using spatial quadrature, Ultrasonics, Ferroelectrics and Frequency Control, IEEE Transactions on, 45. 3, 852-861, 1998.

[19] J. A. Jensen and P. Munk,A new method for estimation of velocity vectors, Ultrasonics, Ferroelectrics and Frequency Control, IEEE Transactions on, 45. 3, 837-851, 1998.

[20] P. Munk and J. A. Jensen, "Improved beamforming performance using pulsed plane wave decomposition," in *Ultrasonics Symposium, 2000 IEEE*, 2000, pp. 1749-1754.

[21] P. Munk and J. A. Jensen, "Performance of velocity vector estimation using an improved dynamic beamforming setup," in *Proceedings of SPIE*, 2001, p. 227.

[22] C. Sumi, "Multidimensional displacement vector measurement methods utilizing instantaneous phase," in *Engineering in Medicine and Biology Society, 2005. IEEE-EMBS 2005. 27th Annual International Conference of the*, 2006, pp. 1704-1707.

[23] C. Sumi,Displacement vector measurement using instantaneous ultrasound signal phase-multidimensional autocorrelation and Doppler methods, Ultrasonics, Ferroelectrics and Frequency Control, IEEE Transactions on, 55. 1, 24-43, 2008.

[24] H. Liebgott, J. Fromageau, J. E. Wilhjelm, D. Vray, and P. Delachartre,Beamforming scheme for 2D displacement estimation in ultrasound imaging, EURASIP journal on applied signal processing, 2005. 1212-1220, 2005.

[25] H. Liebgott, J. E. Wilhjehm, J. A. Jensen, D. Vray, and P. Delachartre,PSF dedicated to estimation of displacement vectors for tissue elasticity imaging with ultrasound, Ultrasonics, Ferroelectrics and Frequency Control, IEEE Transactions on, 54. 4, 746-756, 2007.

[26] H. Hasegawa and H. Kanai,High-frame-rate echocardiography using diverging transmit beams and parallel receive beamforming, Journal of Medical Ultrasonics, 38. 3, 129-140, 2011.

[27] S. Blaak, Z. Yu, G. C. M. Meijer, C. Prins, C. T. Lancee, J. G. Bosch, and N. de Jong, "Design of a micro-beamformer for a 2D piezoelectric ultrasound transducer," in *Ultrasonics Symposium (IUS), 2009 IEEE International*, 2009, pp. 1338-1341.

[28] M. Alessandrini, A. Basarab, L. Boussel, X. Guo, A. Serusclat, D. Friboulet, D. Kouame, O. Bernard, and H. Liebgott,A New Technique for the Estimation of Cardiac Motion in Echocardiography Based on Transverse Oscillations: a preliminary evaluation in silico and a feasibility demonstration in vivo, Medical Imaging, IEEE Transactions on, PP. 99, 1-1, 2014.

[29] A. Basarab, P. Gueth, H. Liebgott, and P. Delachartre,Phase-based block matching applied to motion estimation with unconventional beamforming strategies, Ultrasonics, Ferroelectrics and Frequency Control, IEEE Transactions on, 56. 5, 945-957, 2009.

[30] H. Liebgott, A. Basarab, S. Marincas, O. Bernard, and D. Friboulet, "Tangential oscillations for motion estimation in echocardiography," 2008, pp. 1761-1764.

[31] H. Liebgott,Impulse response synthesis in ultrasound imaging for vectorial displacement estimation, LYON: INSA-LYON, 138, 2005.

[32] J. C. Bamber and R. J. Dickinson,Ultrasonic B-scanning: a computer simulation, Physics in medicine and biology, 25. 3, 463, 1980.

[33] K. E. Thomenius, "Evolution of ultrasound beamformers," in *Ultrasonics Symposium, 1996. Proceedings., 1996 IEEE*, 1996, pp. 1615-1622.

[34] J. A. Jensen, S. I. Nikolov, K. L. Gammelmark, and M. H. Pedersen,Synthetic aperture ultrasound imaging, Ultrasonics, 44. e5-e15, 2006.

[35] A. Hernandez, O. Basset, P. Chirossel, and G. Gimenez,Spatial compounding in ultrasonic imaging using an articulated scan arm, Ultrasound in medicine & biology, 22. 2, 229-238, 1996.

[36] R. R. Entrekin, B. A. Porter, H. H. Sillesen, A. D. Wong, P. L. Cooperberg, and C. H. Fix, "Real-time spatial compound imaging: application to breast, vascular, and

musculoskeletal ultrasound," in *Seminars in ultrasound, CT and MRI*, 2001, pp. 50-64.

[37] J.-F. Synnevag, A. Austeng, and S. Holm,Adaptive beamforming applied to medical ultrasound imaging, Ultrasonics, Ferroelectrics and Frequency Control, IEEE Transactions on, 54. 8, 1606-1613, 2007.

[38] M. Soumekh,Bistatic synthetic aperture radar inversion with application in dynamic object imaging, Signal Processing, IEEE Transactions on, 39. 9, 2044-2055, 1991.

[39] M. Bashkansky, R. Lucke, E. Funk, L. Rickard, and J. Reintjes,Two-dimensional synthetic aperture imaging in the optical domain, Optics letters, 27. 22, 1983-1985, 2002.

[40] L. N. Bohs, S. C. Gebhart, M. E. Anderson, B. J. Geiman, and G. E. Trahey,2-D motion estimation using two parallel receive beams, Ultrasonics, Ferroelectrics and Frequency Control, IEEE Transactions on, 48. 2, 392-408, 2001.

[41] C. Yoon, G.-D. Kim, Y. Yoo, T.-K. Song, and J. H. Chang,Frequency equalized compounding for effective speckle reduction in medical ultrasound imaging, Biomedical Signal Processing and Control, 8. 6, 876-887, 2013.

[42] J. S. Blogh and L. L. Hanzo, *Third-generation systems and intelligent wireless networking: smart antennas and adaptive modulation*: John Wiley & Sons, 2002.

[43] K. Ranganathan and W. F. Walker,A novel beamformer design method for medical ultrasound. Part I: Theory, Ultrasonics, Ferroelectrics and Frequency Control, IEEE Transactions on, 50. 1, 15-24, 2003.

[44] K. Ranganathan and W. F. Walker,A novel beamformer design method for medical ultrasound. Part II: Simulation results, Ultrasonics, Ferroelectrics and Frequency Control, IEEE Transactions on, 50. 1, 25-39, 2003.

[45] D. Guenther and W. F. Walker,Optimal apodization design for medical ultrasound using constrained least squares part i: theory, Ultrasonics, Ferroelectrics and Frequency Control, IEEE Transactions on, 54. 2, 332-342, 2007.

[46] E. S. Ebbini and C. A. Cain,Multiple-focus ultrasound phased-array pattern synthesis: optimal driving-signal distributions for hyperthermia, Ultrasonics, Ferroelectrics and Frequency Control, IEEE Transactions on, 36. 5, 540-548, 1989.

[47] P.-C. Li, S. Flax, E. Ebbini, and M. O'Donnell,Blocked element compensation in phased array imaging, Ultrasonics, Ferroelectrics and Frequency Control, IEEE Transactions on, 40. 4, 283-292, 1993.

[48] X. Guo, D. Friboulet, and H. Liebgott, "Transverse oscillations beamformer design for sector scan using back-propagation," in *Biomedical Imaging (ISBI), 2012 9th IEEE International Symposium on*, 2012, pp. 1100-1103.

[49] H. Liebgott, A. Basarab, P. Gueth, D. Friboulet, and P. Delachartre,Transverse oscillations for tissue motion estimation, Ultrasonics, 50. 6, 548-555, 2010.

[50] J. W. Goodman, *Introduction to Fourier optics*: Roberts & Company Publishers, 2005.

[51] H. Liebgott, A. Ben Salem, A. Basarab, H. Gao, P. Claus, J. D'Hooge, P. Delachartre, and D. Friboulet, "Tangential sound field oscillations for 2D motion estimation in echocardiography," 2009, pp. 498-501.

[52] C. Sumi,Determination of lateral modulation apodization functions using a regularized, weighted least squares estimation, Journal of Biomedical Imaging, 2010. 1-7, 2010.

[53] P. Gueth, A. Basarab, H. Liebgott, and P. Delachartre, "P4B-2 Beamforming Techniques for Motion Estimation in Ultrasound Elastography," 2007, pp. 1953-1956.

[54] M. J. Pihl, J. Marcher, and J. A. Jensen,Phased-array vector velocity estimation using transverse oscillations, Ultrasonics, Ferroelectrics and Frequency Control, IEEE Transactions on, 59. 12, 2662-2675, 2012.

[55] M. J. Pihl and J. A. Jensen, "Measuring 3D Velocity Vectors using the Transverse Oscillation Method," in *IEEE International Ultrasonics Symposium*, Dresden, Germany., 2012, p. in press.

[56] M. Fink,Time reversal of ultrasonic fields. I. Basic principles, Ultrasonics, Ferroelectrics and Frequency Control, IEEE Transactions on, 39. 5, 555-566, 1992.

[57] T. Dietenbeck, M. Alessandrini, D. Barbosa, J. D'hooge, D. Friboulet, and O. Bernard,Detection of the whole myocardium in 2D-echocardiography for multiple orientations using a geometrically constrained level-set, Medical image analysis, 16. 2, 386-401, 2012.

[58] J. A. Jensen, "Field: A program for simulating ultrasound systems," 1996.

[59] J. A. Jensen and N. B. Svendsen,Calculation of pressure fields from arbitrarily shaped, apodized, and excited ultrasound transducers, Ultrasonics, Ferroelectrics and Frequency Control, IEEE Transactions on, 39. 2, 262-267, 1992.

[60] S. Salles, G. Zahnd, H. Liebgott, A. Sérusclat, and D. Vray, "Real time US-tagging combined with phase-based optical flow applied to 2D motion estimation of the carotid artery wall. IEEE Ultrasonics Symposium, Dresden," ed: Germany), page, 2012.

[61] S. L. Hahn,Multidimensional complex signals with single-orthant spectra, Proceeding of the IEEE, 80. 1287-1300., 1992.

[62] A. Basarab, H. Liebgott, and P. Delachartre,Analytic estimation of subsample spatial shift using the phases of multidimensional analytic signals, IEEE Transactions of Image Processing, 18. 2, 440-447, 2009.

[63] M. Alessandrini, H. Liebgott, D. Friboulet, and O. Bernard, "Simulation of realistic echocardiographic sequences for ground-truth validation of motion estimation," in *Image Processing (ICIP), 2012 19th IEEE International Conference on*, 2012, pp. 2329-2332.

[64] P. Tortoli, L. Bassi, E. Boni, A. Dallai, F. Guidi, and S. Ricci,ULA-OP: an advanced open platform for ultrasound research, Ultrasonics, Ferroelectrics and Frequency Control, IEEE Transactions on, 56. 10, 2207-2216, 2009.

[65] S. Ricci, L. Bassi, E. Boni, A. Dallai, and P. Tortoli,Multichannel FPGA-based arbitrary waveform generator for medical ultrasound, Electronics Letters, 43. 24, 1335-1336, 2007.

[66] J. Udesen and J. A. Jensen,Investigation of transverse oscillation method, Ultrasonics, Ferroelectrics and Frequency Control, IEEE Transactions on, 53. 5, 959-971, 2006.

[67] G. Clement, R. Liu, S. Letcher, and P. Stepanishen,Temporal backward planar projection of acoustic transients, The Journal of the Acoustical Society of America, 103. 4, 1723-1726, 1998.

[68] P. Munk and J. A. Jensen. Estimation of blood velocity vectors using ultrasound. Technical University of DenmarkDanmarks Tekniske Universitet, Department of Information TechnologyInstitut for Informationsteknologi, 2002,

FOLIO ADMINISTRATIF

THESE SOUTENUE DEVANT L'INSTITUT NATIONAL DES SCIENCES APPLIQUEES DE LYON

NOM : GUO **DATE de SOUTENANCE:** 12/09/2014

Prénoms : Xinxin

TITRE : Back-propagation beamformer design with Transverse Oscillations for motion estimation in echocardiography

NATURE : Doctorat **Numéro d'ordre : :** 2014ISAL0085

Ecole doctorale : Ecole Doctoral Electronique, Electrotechnique, Automatique

Spécialité : Image et System

RESUME :

L'échographie est aujourd'hui l'une des modalités les plus populaires de diagnostic médical. Elle permet d'observer, en temps réel, le mouvement des organes, ce qui facilite le diagnostic des pathologies pour les médecins. L'échocardiographie, l'imagerie du flux sanguin et l'élastographie sont les domaines privilégié pour l'estimation de mouvement basée sur l'échographie (en raison de sa cadence élevée d'acquisition).En imagerie cardiaque, les systèmes d'imagerie classiques sont limités en terme de précision dans la direction transversale (direction perpendiculaire à celle de propagation). En partant de la formation des images, ce problème peut être résolu en modifiant le mode de formation de voie afin d'introduire des oscillations transversales (OTs) dans la fonction d'étalement ponctuelle (PSF).

Les techniques d'oscillations transversales ont montré leur potentiel pour améliorer la précision de l'estimation du mouvement local dans la direction transversale. La modélisation classique des OT en géométrie linéaire est basée sur l'approximation de Fraunhofer et permet de relier la PSF et la fonction de pondération par une transformée de Fourier. Afin d'adapter la formation des OTs en échocardiographie, nous proposons une technique spécifique, basée sur la rétro-propagation et permettant de construire des OTs en géométrie sectorielle.

Les performances de la méthode de rétro-propagation proposée ont été étudiées et comparées à celles issues de méthode classique basée sur la transformée de Fourier. Ainsi, nous avons évalué la qualité de la PSF, celle de l'estimation de mouvement cardiaque en simulation, ainsi que la qualité des PSF obtenues expérimentalement. Les résultats montrent que les OTs obtenues par la méthode de rétro-propagation présentent une meilleure qualité que celle obtenue par le formateur de voie conventionnel basé sur la transformée de Fourier.

Une autre méthode, basée sur la décomposition en onde plane et un principe de rétro-propagation différent, a également été étudiée. Cette méthode permet de mieux prendre en compte les propriétés 2D de la PSF. En rétro-propageant l'ensemble des ondes planes obtenues suite à la décomposition du champ et en sommant tous les signaux ainsi reçus au niveau de la sonde, nous pouvons obtenir les signaux d'excitation pour chaque transducteur. De cette façon, une PSF très proche de la PSF théorique souhaité peut ainsi être obtenue. Cette approche a été adaptée et testé en géométrie sectorielle. La qualité de la PSF obtenue le long de l'axe frontal de la sonde est meilleure que celle basée sur la relation de Fourier. Cependant cette qualité diminue lorsque l'on s'éloigne de l'axe de la sonde, aussi un travail supplémentaire sera nécessaire pour adapter la décomposition en ondes planes à une imagerie sectorielle complète.

MOTS-CLES: échocardiographie, estimation de mouvement, rétro-propagation, oscillation transversale, formation de voie, décomposition de l'onde plane

Laboratoire (s) de recherche: Creatis (CNRS UMR 5520, INSERM U1044)

Directeur de thèse: Denis Friboulet, Hervé Liebgott

Président de jury : Denis Kouamé

Composition du jury :

GIRAULT Jean-Marc, LETHIECQ Marc, KOUAME Denis, CACHARD Christian, FRIBOULET Denis, LIEBGOTT Hervé